Finite-element modelling of middle-ear vibrations under quasi-static pressurization

Tina Qian

Department of BioMedical Engineering

McGill University, Montréal

December 2019

A thesis submitted to McGill University

in partial fulfillment of the requirements of the degree of

Master of Engineering

Finite-element modelling of middle-ear vibrations under quasi-static pressurization

Abstract

Early identification of hearing loss is important because if untreated it can lead to delayed language development and other difficulties. Current tools for newborn hearing screening are subject to excessively high false-positive rates. Tympanometry is a promising tool for improving screening tests by evaluating the condition of the middle ear, but it is poorly understood in newborns. Tympanometry involves large deformations, non-linear responses, viscoelastic (time-dependent) effects, and complex dynamic responses, which make it hard to model. A previous gerbil finite-element model developed in our lab was the first numerical simulation of tympanometry involving the simultaneous application of large quasi-static pressures and small sound pressures, and it succeeded in replicating some features of tympanometry. However, the model involved over-simplified anatomical details of the ossicles to reduce the computational cost. The goal of this study was to improve the model by adding a representation of the incudostapedial joint and its surrounding structures.

The model employed a quasi-linear visco-hyperelastic model with several time constants in a Prony series. Material properties were taken from previous models and publications. The tympanic membrane was assumed to be homogeneous and nearly incompressible. The loads, combining high quasi-static pressures with low-amplitude sound pressures, both low-frequency pure tones and wideband chirps, reflected the conditions in tympanometry. The model was verified against our previous models, and validated against data from the literature and our recent laser vibrometry data for the pressurized gerbil middle ear. The model demonstrated experimentally and clinically observed features, including hysteresis and the asymmetry in the vibration amplitude between positive and negative static pressures.

This numerical model will help us gain insight into how the middle ear responds to different stimuli and thus open up new approaches to the interpretation of tympanometric measurements.

Modélisation par éléments finis des vibrations de l’oreille moyenne sous pressurisation quasi-statique

Résumé

L’identification précoce de la perte auditive est importante car si elle n’est pas traitée, elle peut entraîner un retard du développement du langage et d’autres difficultés. Les outils actuels de dépistage auditif du nouveau-né sont soumis à des taux de faux positifs excessivement élevés. La tympanométrie est un outil prometteur pour améliorer les tests de dépistage en évaluant l’état de l’oreille moyenne, mais elle est mal comprise chez les nouveau-nés. La tympanométrie implique de grandes déformations, des réponses non linéaires, des effets viscoélastiques (dépendants du temps) et des réponses dynamiques complexes, ce qui rend la modélisation difficile. Un précédent modèle à éléments finis de gerbille développé dans notre laboratoire était la première simulation numérique de tympanométrie impliquant l’application simultanée de grandes pressions quasi-statiques et de petites pressions sonores, et il a réussi à reproduire certaines caractéristiques de la tympanométrie. Cependant, le modèle impliquait des détails anatomiques trop simplifiés des osselets pour réduire le coût de calcul. Le but de cette étude était d’améliorer le modèle en ajoutant une représentation de l’articulation incudostapédiale et de ses structures environnantes.

Le modèle a utilisé un modèle visco-hyperélastique quasi linéaire avec plusieurs constantes de temps dans une série Prony. Les propriétés des matériaux ont été tirées de modèles et publications précédents. La membrane tympanique était supposée homogène et presque incompressible. Les charges, combinant des pressions quasi-statiques élevées avec des pressions sonores de faible amplitude, à la fois des sons purs à basse fréquence et des gazouillis à large bande, reflétaient les conditions de la tympanométrie. Le modèle a été vérifié par rapport à nos modèles précédents, et validé par rapport aux données de la littérature et à nos données récentes de vibrométrie laser pour l’oreille moyenne de gerbille sous

pression. Le modèle a démontré des caractéristiques qui sont observés expérimentalement et dans la clinique, comme l'hystérésis et l'asymétrie de l'amplitude des vibrations entre les pressions statiques positives et négatives.

Ce modèle numérique nous aidera à mieux comprendre comment l'oreille moyenne répond à différents stimuli et ouvrira ainsi de nouvelles approches pour l'interprétation des mesures tympanométriques.

Acknowledgements

I would like to express my appreciation to everyone who has contributed to this work in any way.

Firstly, I would like to express my sincere gratitude to my supervisor, Dr. W. Robert J. Funnell, for his continuous guidance and support through each stage of this work, for his patience, motivation, and immense knowledge. I deeply appreciate his willingness and effort to review multiple drafts of this thesis at short notice and late hours. I could not have imagined having a better supervisor and mentor for my study.

I am also very grateful to the members of the Auditory Mechanics Laboratory. I would like to thank Marzieh, for her kindness and her support. My thanks also go to Sajjad, for his valuable input. I would also like to thank Orhun, for sharing his knowledge in coding, for explaining his data to me and for always encouraging me to attend social activities. My thanks also go to Majid and Hamid, for their insightful and constructive advice on dealing with the challenges in my work.

I would like to acknowledge Dr. Robert Kearney, for what he taught me in the signal processing course. I learnt to always be careful with data processing. My thanks also go to Dr. Ross Wagner, for the technical support and for what he taught me about biomedical devices. I would also like to acknowledge Pina Sorrini, Trang Q. Tran and Sabrina Teoli, for their valuable guidance and support during my study.

I am deeply indebted to my parents Xiao’an and Tianhui, and my siblings Nanyuan and Shuxi. They always supported me and encouraged me to pursue my passion and always welcomed me home with hugs and smiles. This accomplishment would not have been possible without them.

This work was supported by the Canadian Institutes of Health Research, the Natural Sciences and Engineering Research Council of Canada and the BioMedical Engineering Department.

Table of Contents

Chapter 1: Introduction

1.1 Motivation

Hearing loss is one of the most common congenital defects. Impaired hearing can lead to deficits in language, cognition and social skill development. Early detection accompanied by appropriate early intervention is essential. Neonatal hearing screening tools including otoacoustic emission (OAE) and auditory brainstem response (ABR) tests have high false-positive rates that are often caused by transient middle-ear dysfunction due to fluid and other residual material in the first 48 hours after birth.

Tympanometry provides information about the acoustic input admittance of the outer and middle ear in the presence of large static pressures. It is a promising clinical took for evaluating the status of the middle ear in newborns. Since tympanometry can effectively identify various forms of middle-ear dysfunction, it can be used to help interpret OAE and ABR measurements. In older children and adults, tympanometry with a single low probe-tone frequency provides easy-to-interpret results but the interpretation may be very different in newborn ears because of anatomical and physiological changes during maturation. Tympanometry with a high-frequency or multi-frequency probe tone may provide more information on the middle-ear condition but is often hard to interpret and is even less well understood for the infant ear. For example, tympanometry results are influenced by the direction of the quasi-static pressure change and the rate of the pressure pump. Currently, the clinical significance of these parameters is not well understood.

Numerical models of the middle ear are very helpful in understanding and predicting the responses of the middle ear. Such models allow us to study the effects of different parameters quantitatively to get a better understanding of the functions of different middle-ear components. Finite-element models allow us to connect the detailed anatomical and mechanical properties of the middle-ear structures to

the physiological characteristics of the system. In recent years, because of increasing computational power, increasing accessibility of finite-element software and the improved integration of solvers and post-processing tools, the finite-element method has been increasingly applied in modelling of the middle ear.

Tympanometry involves both non-linear responses and viscoelastic (time-dependent) effects. The model of Choukir (2017) was the first non-linear middle-ear model that could simulate responses to an acoustic stimulus in the presence of large quasi-static pressures (comparable to those in tympanometry). However, some aspects of that model were very much simplified.

1.2 Objectives

The overall research programme of which this thesis forms part has a focus on improving understanding of tympanometry in newborns. In this research, an animal model (the Mongolian gerbil ear) is used because it allows comparison with experimental measurements that are not possible with human ears. The overall objective of the present work was to develop a better quantitative understanding of the mechanical behaviour of the gerbil middle ear, particularly its response under conditions involving both non-linear viscoelasticity and linear dynamics as found in tympanometry. The specific objectives of this work are listed below:

1) Modification of the previous model by inserting some middle-ear components, with the material properties of the different components estimated from previous work.
2) Verification of the new model's low-amplitude response by comparison to the previous model.
3) Investigation of the non-linear behaviour of the new model in conditions relevant to tympanometry, involving the presence of large quasi-static ear-canal pressures with and without the presence of a sound stimulus.
4) Comparison of the model results with experimental measurements.

1.3 Thesis outline

Chapter 2 of the thesis provides a brief overview of the auditory system with an emphasis on the anatomy of the middle ear. Chapter 3 consists of a literature review of concepts and previous studies related to the present work. Chapter 4 presents the methods and is followed by our results in Chapter 5. Chapter 6 includes a summary of this work, a discussion of potential future work and the significance of our research.

Chapter 2: The auditory system

2.1 Introduction

The auditory system is responsible for the sense of hearing. The system serves to gather sound signals, transform and amplify them, and transmit the results to the brain via neural pathways. The system consists of three sections: the outer, middle, and inner ear (Fig. 2-1). Detailed descriptions of the anatomy of the ear are illustrated in numerous anatomy textbooks (e.g., Standring, 2016, chaps. 36 & 37). This chapter provides a brief description of the anatomical characteristics of each part of the human ear, based largely on Standring (2016), with an emphasis on the middle ear as it is most relevant to this thesis. In section 2.5, we highlight the similarities and differences between the human middle ear and the gerbil middle ear. Section 2.6 is a brief conclusion.

2.2 Anatomy of the outer ear

The outer ear (see Fig. 2-1) includes the pinna (or auricle) and the outer ear canal (or external acoustic meatus). The pinna has a curved rim called the helix, a deep notch called the concha, and an adipose bottom part called the lobule (or earlobe). The pinna is approximately three-quarters of its adult size at birth and continues to grow up to about 11 years of age (e.g., Purkait, 2013). The ear canal is an air-filled tube that extends from the pinna to the eardrum (or tympanic membrane, TM). It is approximately 2.5 cm in length from the floor of the concha of the auricle (e.g., Standring, 2016). The lateral, cartilaginous part forms approximately one-third of the length of the ear canal, and the osseous part forms the remaining two-thirds of the canal.

2.3 Anatomy of the middle ear

The middle ear is an irregularly shaped, air-filled space laterally bounded by the TM. Within the middle-ear cavity lie three ossicles, the malleus, the incus and the stapes. The ossicles transmit the vibrations of the tympanic membrane across the cavity to the inner ear.

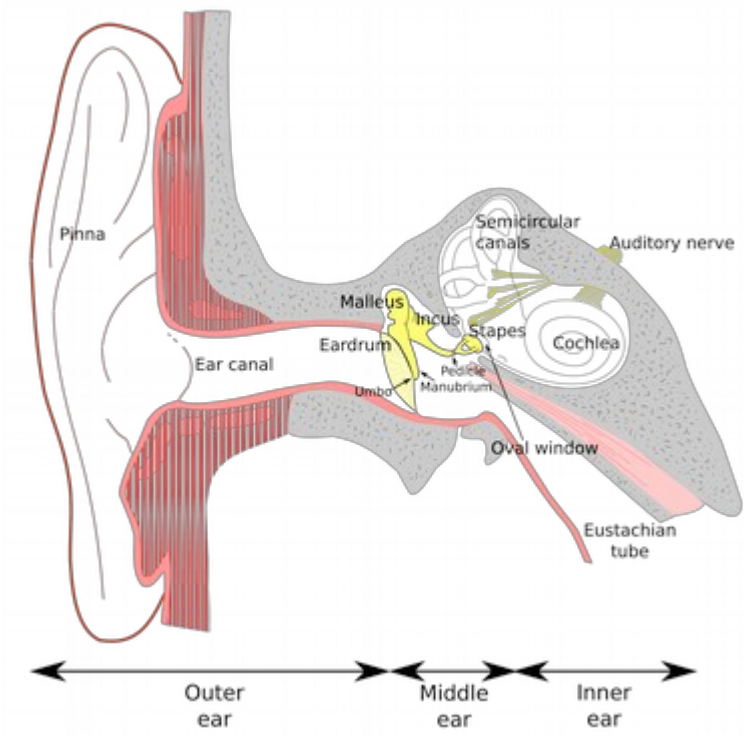

Figure 2-1: Ear anatomy schematic, showing the outer ear, the middle ear and the inner ear spaces. (Adapted from http://audilab.bme.mcgill.ca/teach/me_saf/)

2.3.1 Middle-ear cavity

The middle-ear air cavity can be subdivided into four parts: the tympanic cavity, the aditus ad antrum, the mastoid antrum and the mastoid air cells. The tympanic cavity is bounded laterally by the TM and medially by the oval window. It contains the middle-ear ossicles. Posterior to the tympanic cavity is the aditus ad antrum, which is a short passageway that connects the cavity and the mastoid antrum. The mastoid antrum (or the tympanic antrum) is within the petrous portion of the temporal bone and communicates with the mastoid air cells, which are small air spaces of variable size. The volume of the mastoid air cells usually makes up most of the volume of the middle-ear cavity and is very variable.

Although the mastoid antrum is well developed at birth, the mastoid air cells continue to extend and pneumatize (i.e., to fill with air) into the mastoid antrum even after puberty (Standring, 2016).

2.3.2 Tympanic membrane

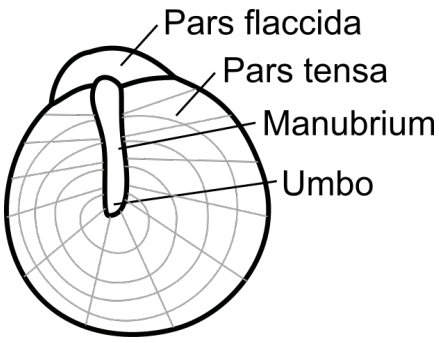

Figure 2-2: Anatomy of tympanic membrane. (From http://audilab.bme.mcgill.ca/teach/me_saf/)

The TM is a thin, cone-shaped membrane, separating the middle-ear cavity from the external auditory canal. The apex of the TM cone is referred to as the umbo. A ring of bone called the tympanic annulus encircles the TM. The longest diameter of the TM is between 9 and 10 mm and the shortest diameter is about 8 to 9 mm (e.g., Kassem et al., 2010).

The TM consists of two components, the pars tensa (PT) and the pars flaccida (PF) (Fig. 2-2). Both components have three layers: the inner mucosal layer, the outer epidermal layer and the intermediate fibrous layer (Fig. 2-3). The epidermis of the human TM exhibits a centripetal migration pattern, from the umbo outward to the external meatus. This serves as a self-cleaning mechanism for ear wax and cell debris (e.g., Lim, 1995). The PT and PF are different in the compositions of their fibrous layers. In the PT, the fibres of the radial collagenous layer converge on the manubrium, while the circular collagenous layer thickens towards the periphery. The PF is thicker than the PT and has a much looser structure which contains vessels, nerve endings and mast cells (e.g., Lim, 1970; Stenfeldt et al., 2006).

Lim (1970) reported the thickness of the PT as being between 30 and 90 µm in adults. They also reported the PF to be approximately one-tenth of the TM in surface area and to have a thickness that varies between 30 and 230 µm in adults. Ruah et al. (1991) measured TM thickness in human temporal bones of different ages and reported age-related changes of the TM thickness. They found the thickness of the PT and PF to be significantly higher in newborns. Other groups have reported that the thickness of the PF in adults has a range from 40 to 120 µm and the thickness of the PT has a range from 120 to 140 µm (e.g., Kuypers et al., 2006; Van der Jeught et al., 2013).

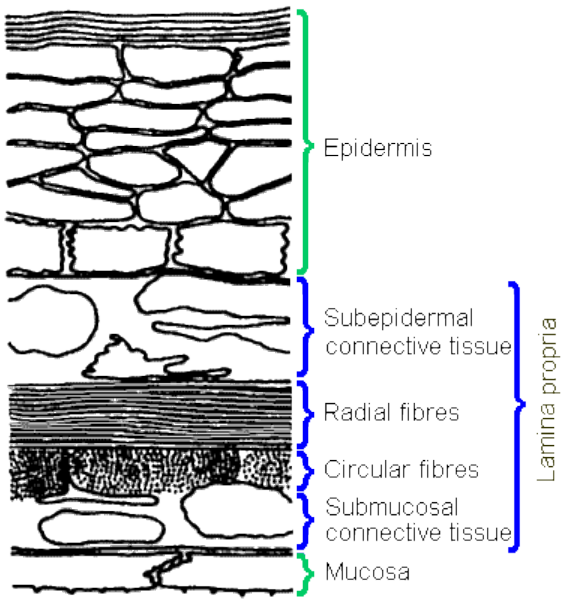

Figure 2-3: Illustration of TM microstructure. (http://audilab.bme.mcgill.ca/teach/me_saf/)

2.3.3 Ossicles

The ossicular chain connects the TM to the oval window and consists of the malleus, incus and stapes. The malleus (Latin for “hammer”) is the most lateral of the three. It has a head, a neck, and three processes (anterior, lateral and manubrium). The head of the malleus has a round shape and is connected to the incus. The neck of the malleus extends inferiorly to the manubrium. Both the manubrium and the lateral process are connected to the TM.

The incus (Latin for “anvil”) has a body, a short process and a long process. The articular surface of the malleus articulates with the body of the incus via the incudomallear joint (IMJ). The short process extends into the posterior incudal recess of the middle-ear cavity. At the tip of the long process, there is a lenticular process (consisting of a pedicle and a plate) that articulates with the stapes at the incudostapedial joint (ISJ).

The stapes (Latin for “stirrup”) is the smallest bone in the body and has the shape of a stirrup. It consists of a head, a neck, two crura and a footplate. The two crura diverge at the neck and join the stapes footplate separately. The anterior crus is generally shorter, thinner and less curved than the posterior crus. Among the ossicles, the stapes is the most variable (e.g., Saha et al., 2017).

The development of the ear ossicles starts at fours weeks into intrauterine life. The ossicles have achieved their adult size and configuration at birth (Standring, 2016).

2.3.4 Joints

There are two synovial joints between the three ossicles. The IMJ is saddle-shaped. The ISJ has been described as ball-and-socket, but the surfaces are only mildly convex and concave. As in typical synovial joints, articular cartilage covers the articular surfaces, and in between there is synovial fluid. Each joint is surrounded by a fibrous joint capsule which contains synovial fluid inside. Karmody et al. (2009) reported the existence of a fibrous articular disk (which they referred to as a meniscus) that divides the joint space into unequal parts, but Soleimani et al. (2020) did not observe it in their histological sections. As Soleimani et al. (2020) discussed, the variability of the thickness of the synovial space of the ISJ in experimental measurements is huge because the joint is extremely delicate and under observation might be dehydrated, dislocated or changed in other ways.

2.3.5 Muscles and ligaments

The ossicles are connected to the tympanic cavity wall by ligaments. According to Standring (2016), the malleus has three ligaments: the anterior, the lateral and the superior. The anterior mallear ligament stretches from the neck of the malleus to the cavity wall. The lateral ligament is triangularly shaped and connects the head of the malleus to the cavity wall. The superior ligament connects the head of the malleus to the roof of the epitympanic recess. The incus has a posterior incudal ligament that in human stretches in two bundles from the short process to the cavity wall at the posterior incudal recess. There is also a mucosal fold (sometimes referred to as the superior incudal ligament) that connects the body of the incus to the roof of the epitympanic recess. A study by Lemmerling et al. (1997) reported great variability in the mallear and incudal ligaments. They observed the anterior, superior, and lateral mallear ligaments and the medial and lateral parts of the posterior incudal ligament in only 68%, 46%, 95%, 26% and 34% of the 75 ears they examined. The stapedial annular ligament connects the base of the stapes to the oval window of the cochlea. The posterior part of this ligament is much narrower than the anterior part.

There are two intratympanic muscles: tensor tympani and stapedius. The tensor tympani originates from the cartilaginous part of the pharyngotympanic (i.e., Eustachian) tube and is inserted into the handle of the malleus. The stapedius muscle connects the stapes head to the mastoid wall of the tympanic cavity. Both muscles are fully developed prenatally, but their attachments mature about one week after birth (Saunders et al., 1983, p. 10). Both muscles reduce the response of the middle ear by inhibiting the motion of the ossicles. They attenuate the low-frequency components of a loud complex sound to prevent the masking of the sound’s high-frequency components (Borg and Counter, 1989).

2.4 Anatomy of the inner ear

The inner ear is a structure of interconnected membranous sacs and ducts. It is a liquid-filled labyrinth and has three main parts: the cochlea, the vestibule and the semicircular canals. Medial to the tympanic cavity and between the cochlea and the semicircular canals lies the vestibule. It is egg-shaped but flattened transversely. There are mechanosensory receptors in the vestibule that detect the steady-state head position. Posterior to the vestibule are located the three semicircular canals, which detect angular acceleration during tilting or turning of the head. The cochlea is anterior to the vestibule and is connected laterally to the stapes via the oval window. It is coiled around a conical central axis like a snail shell. The basilar membrane sits inside the cochlea and carries two types of sensory hair cells: the inner hair cells and the outer hair cells. The inner hair cells are pear-shaped; they only form one row and extend along the axial border of the basilar membrane. The outer hair cells are long cylindrical cells that form two to three rows radially within the organ of Corti. They are nearly twice as tall as the inner hair cells.

2.5 Gerbil middle ear

The middle ear of the Mongolian gerbil (*Meriones unguiculatus*) has been a popular subject of experimental studies and modelling (e.g., Dirckx et al., 1998; Rosowski et al., 1999; Lee and Rosowski, 2001; Elkhouri et al., 2006; Maftoon et al., 2015). Gerbil ears are relatively large for their overall body size, allowing easier observation of the TM during experimental procedures. Gerbils are also easy to breed and are relatively inexpensive, making them convenient subjects for experimental measurements.

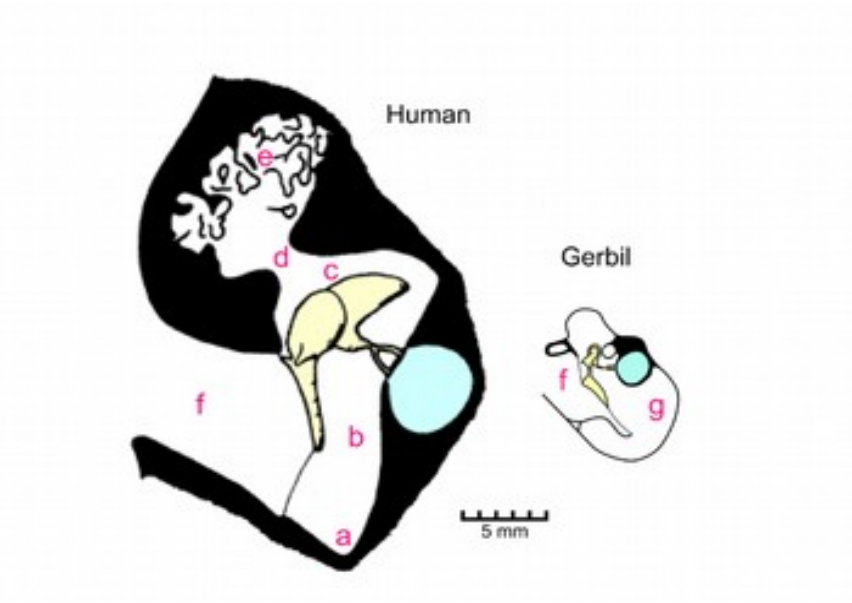

Figure 2-4: Sizes and configurations of human and gerbil middle ears. Air spaces in the ear: (a) hypotympanum; (b) tympanic cavity; (c) epitympanic recess; (d) aditus; (e) mastoid cells; (f) ear canal; (g) hypertrophied bulla. (After Funnell, http://audilab.bme.mcgill.ca/teach/me_saf/)

Despite overall similarities in anatomy and function between the human and gerbil middle ears, there are several differences:

1. Size: the human middle ear is larger than the gerbil middle ear, as shown in Fig. 2-4, although the size of the gerbil middle ear is larger relative to its body size.

2. Presence of the bulla: a thin bony shell called the bulla encapsulates the gerbil middle ear.

3. Anatomy of the manubrium: the entire length of the gerbil manubrium is tightly attached to the PT, while in human the manubrium is only tightly attached to the PT at the umbo and at the lateral process.

4. Shape and relative size of PF: The gerbil's TM, unlike the human TM, has a relatively large and circularly shaped PF.

5. Composition of TM: The human PT contains more and denser collagen than does the gerbil's (Chole and Kodama, 1989).

6. TM thickness: The gerbil TM is much thinner than the human TM. According to Decraemer and Funnell (2008), the gerbil PF has a thickness of around 23 μm in its thin central region and increases steeply to 5 to 10 times thicker approaching the bony annulus. The gerbil PT has a thickness between 5.6 to 14.4 μm in the thin central region and increases to around 34 μm near the rim.

7. Anatomy of the anterior mallear process: The gerbil anterior mallear attachment is a bony attachment as opposed to the ligament in the human middle ear. The anterior process is also longer in the gerbil.

8. Anatomy of the posterior incudal ligament: In the gerbil middle ear, the ligament surrounds the short process of the incus, but the human posterior incudal ligament is composed of two bundles (see Fig. 2-5).

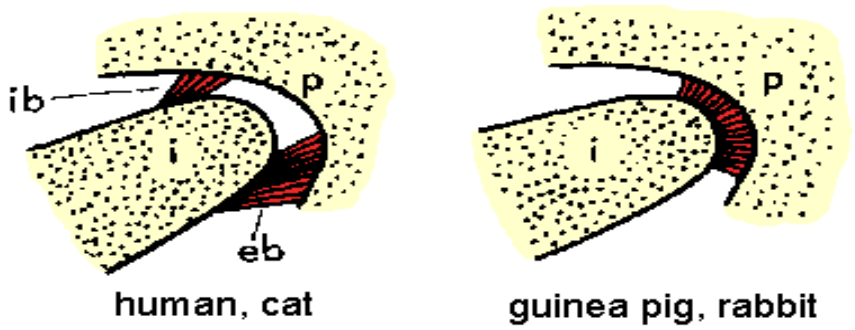

Figure 2-5: Different configuration of posterior incudal ligament in human and gerbil. ib = internal bundle, eb = external bundle, i = incus, p = periotic bone. (Adapted from http://audilab.bme.mcgill.ca/teach/me_saf/)

2.6 Conclusion

In this chapter, we presented anatomical descriptions of the human ear with an emphasis on the middle ear. We have shown that the middle ear is a system with complex anatomy and contains many tissue types. We also compared the gerbil middle ear to that in humans. Significant variations can be found within species and between species.

Chapter 3: Literature review

3.1 Introduction

In this chapter, we give a summary of concepts and previous studies relevant to our research. In section 3.2, the principle and applications of tympanometry are presented. In section 3.3, the principle of finite-element modelling, its applications and a number of relevant middle-ear models are summarized. In section 3.4, a review of previous experimental studies on the middle ear is presented. In section 3.5, we summarize models and experimental measurements with an emphasis on the ISJ.

3.2 Tympanometry

Tympanometry is a promising clinical tool for evaluating the status of the middle ear in newborns. In section 3.2.1, we present the principles of tympanometry. In section 3.2.2, we present clinical applications of tympanometry. Finally, in section 3.2.3, we review the use of tympanometry in newborns.

3.2.1 Principles of tympanometry

The following information is mostly based on Van Camp et al. (1986). Tympanometry provides information about the acoustic input admittance of the outer and middle ear. Acoustic admittance Y is the reciprocal of impedance Z and is defined as the volume velocity response to a known pressure, expressed as

$$Y = 1/Z = U/P \quad , \tag{3-1}$$

where U is the volume velocity (i.e., the volume of fluid that passes through a unit surface area per unit time) and P is the sound pressure at the point of measurement. Admittance and impedance are complex numbers; they can be expressed either as a combination of real and imaginary parts (namely, conductance G and susceptance B for admittance) or using magnitude and phase. Acoustic admittance

has units of mho (m^3/Pa·s). In tympanometry, in addition to the acoustic stimulus, there is also a pump that generates quasi-static pressures generally ranging between −4 and +4 kPa. (The unit for pressure commonly used in clinical tympanometry is daPa, where 1 daPa=10 Pa.)

An illustration of a tympanometer is shown in Fig. 3-1. A probe is inserted into the ear canal and seals the air in the canal. The probe contains three components: a sound source that generates acoustic stimuli, a microphone that measures the resulting sound pressure levels, and a pump that produces varying quasi-static pressures. The microphone voltage values are monitored and converted to equivalent admittance values.

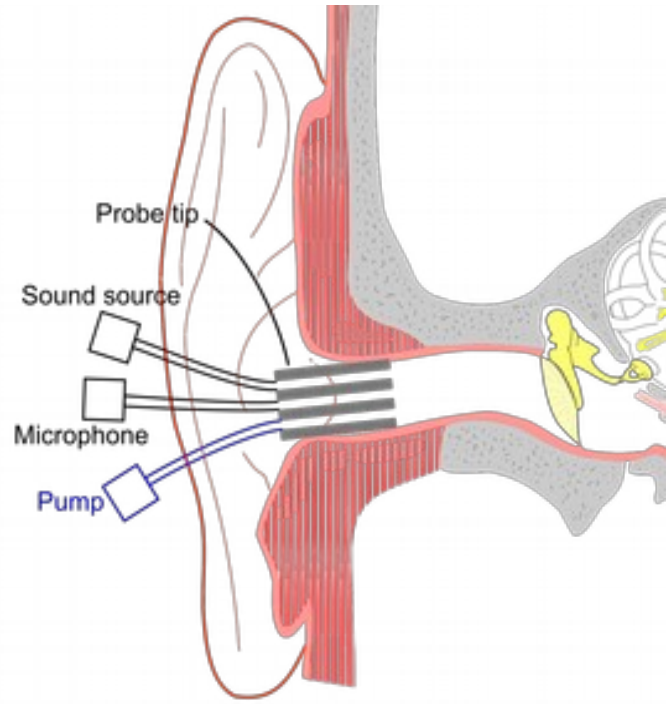

Figure 3-1: Illustration of a tympanometer (After Funnell, http://audilab.bme.mcgill.ca/teach/me_obj/)

The first commercial tympanometer was introduced clinically in the 1970s (Van Camp et al., 1986, p. 21) and was capable of measuring the acoustic admittance at two probe frequencies (220 Hz and 660 Hz). The resulting tympanogram shows the measured acoustic input admittance as a function of the quasi-static pressure (see Fig. 3-2 for an example). The acoustic admittance is related to the amount of

sound energy absorbed and reflected by the TM and can thereby provide information about the status of the middle ear.

However, the probe tip has to be placed at the entrance of the ear canal and cannot be placed directly on the TM surface. Therefore, the admittance measured at the probe tip (Y_a) (i.e., “a” for acoustic) is the sum of the admittance of the ear-canal volume (Y_{ec}) (i.e., “ec” for ear canal) and the admittance at the TM (Y_{tm}). We can calculate Y_{tm} if we know Y_{ec}. Early studies (e.g., Terkildsen and Thomsen, 1959) suggested that Y_{ec} can be measured when a large static pressure is applied to the ear canal, pushing or pulling the TM almost to its limit. As a result, the TM and other middle-ear structures cannot vibrate much. Therefore, all (or at least most) of the energy from the probe tip is reflected from the surface of the eardrum, making $Y_a \approx Y_{ec} + Y_{tm}$.

A real tympanogram is asymmetric, with higher admittance values for positive pressure values than for negative values. The asymmetry has been said to come from eardrum movement, enlargement of the cartilaginous ring of the TM, movement of the probe tip, and viscoelasticity of the soft tissue (Elner et al., 1971).

Tympanograms can be analyzed qualitatively or quantitatively. Qualitative methods are based on the overall shape of the tympanogram (e.g., Fig. 3-2A), while the quantitative methods are based on specific measurable characteristics (e.g., Fig. 3-2B). A popular qualitative classification system was developed by Lidén (1969) and Jerger (1970). The following information is mostly based on Shanks and Shobet (2008). Type A tympanograms (see Fig. 3-2A) indicate the normal condition of the middle ear. Type A tympanograms have subcategories type A_S (“S” refers to a shallow notch in an impedance tympanogram) with a flattened peak, and type A_D (“D” refers to a deep notch in an impedance tympanogram) with a sharper peak. These subcategories indicate middle-ear conditions that require more attention: Type A_S tympanograms are associated with otosclerosis, and type A_D tympanograms are

related to ossicular discontinuity or atrophic scarring of the eardrum. Type B tympanograms are flat and generally occur with middle-ear effusion and eardrum perforation. Type C tympanograms have peaks shifted towards the negative pressure. A shifted peak indicates static pressure in the middle-ear space, which is often a result of sinus congestion, ear infection or dysfunction of the Eustachian tube.

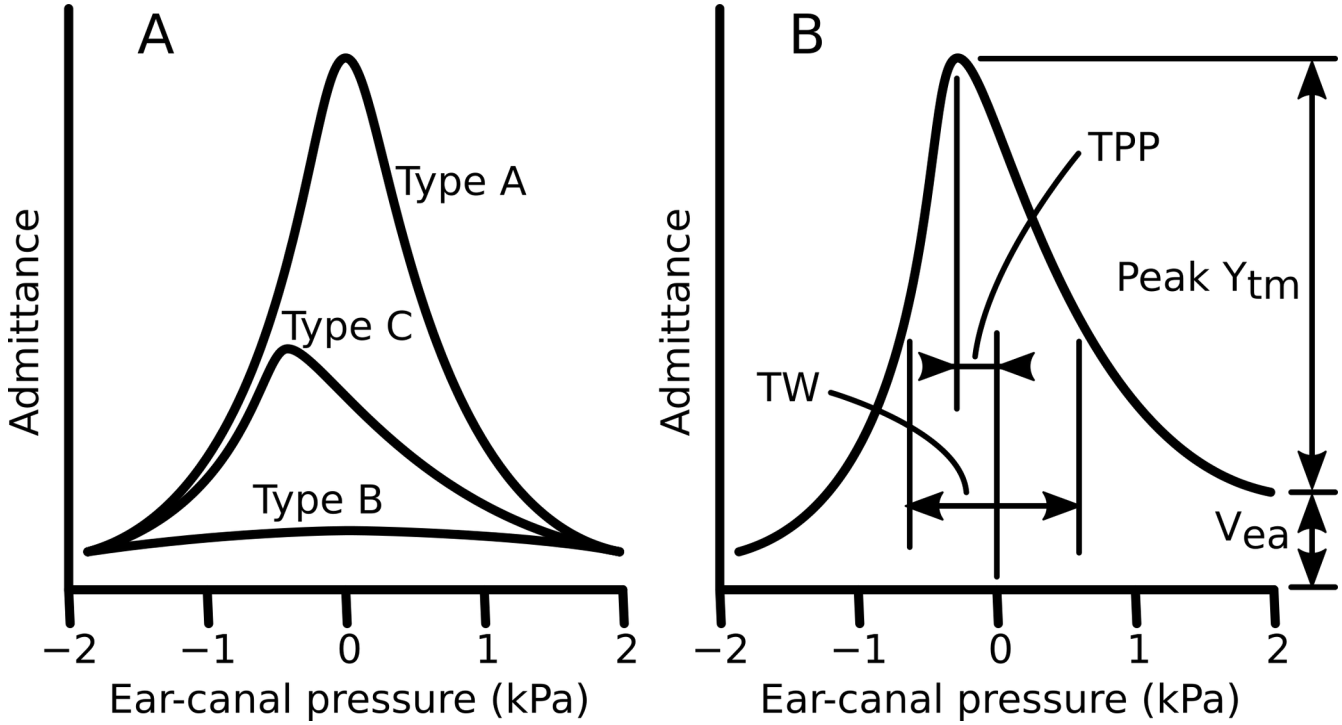

Figure 3-2: Two methods for analyzing 226 Hz tympanograms. (A) A qualitative analysis based on tympanogram shape. (B) A quantitative analysis based on equivalent ear canal volume, peak static acoustic admittance, tympanogram peak pressure and tympanogram width.

Fig. 3-2B showcases a quantitative method of analyzing a tympanogram. As indicated in the figure, a tympanogram can be interpreted in terms of four values: acoustic admittance magnitude Y_{tm} (mmho), peak pressure *TPP* (daPa), width *TW* (daPa), and external ear canal volume V_{ea} (ml). These four numbers differ in their degrees of diagnostic relevance. Tympanometry can also be analyzed in terms of admittance quantities: susceptance (*B*), conductance (*G*), admittance magnitude (*Y*), and the admittance phase angle (φ). The admittance tympanograms can have patterns with more features and can help to discern specific middle-ear pathologies (Van Camp et al., 1986).

3.2.2 Clinical applications of tympanometry

According to Van Camp et al. (1986), measurements of immitance (a term that includes both admittance and impedance) were first made clinically available in the 1940s and became widely used in the 1970s. Early tympanometry instruments measured only the magnitude of acoustic impedance for a single, low-frequency probe tone of 220 Hz and lacked control units to produce stable sound pressure levels. In the 1970s, a second probe tone of 660 Hz became available in new instruments and its advantage was demonstrated in evaluating mass-related pathologies in the middle ear (Feldman, 1976). Although low-frequency probe tones are still used most frequently, the use of higher-frequency probe tones gained more clinical acceptance because it permitted higher sensitivity for the diagnosis of ossicular-chain diseases (Lilly, 1984). Along with the development of a better-controlled probe tone, quantitative measurements were added to the instrument for more precise diagnostics. As a result, tympanometry became a routine component of audiological and otological evaluation procedures for older children and adults. Audiologists recognize peak patterns and use the position and magnitude of peaks in the tympanograms to diagnose patients with possible middle-ear pathologies (Van Camp et al., 1986). Although measurements of the input admittance only reflect possible abnormalities of the middle ear as a whole, tympanometry has often been used to estimate middle-ear pressure because it is inexpensive, sensitive and non-invasive. It is used clinically to determine the possible presence of fluid in the middle-ear cavity and to evaluate the intactness of the ossicular chain.

The choice of 220 or 226 Hz as the probe-tone frequency was initially made for several reasons (e.g., Van Camp et al., 1986; Kochkin, 2006). Firstly, the impedance value at this frequency is numerically equal to the volume of air in a closed cavity. Calibration became easy because a volume of 1 cm^3 had an impedance of 1 milliohm at a frequency of 226 Hz. Thirdly, transducers at the time were only compatible with low frequencies and became non-linear at high frequencies. Secondly, the low-frequency probe tone allowed precise calculation for a single-component admittance approach as the

phase angle is nearly constant and did not need to be considered. Fourthly, the probe signal level was sufficiently high and did not activate the acoustic stapedial reflex. Also, 220 Hz was not a harmonic of the 50-Hz power-line frequency used in Europe (e.g., Lilly, 1984; Van Camp et al., 1986; Iacovou et al., 2013). As the probe-tone frequency increases, the tympanometric pattern begins to have multiple peaks. Therefore, higher probe-tone frequencies (660 Hz or above) allow a better differentiation between healthy ears and pathological ears (e.g., Feldman, 1976; Colletti, 1977; van de Heyning et al., 1982) and thus provide a more effective basis for categorizing middle-ear conditions based on tympanometric shapes.

Multi-frequency tympanometry (MFT) emerged in the 1970s and offered an alternative approach to conventional tympanometry. One can achieve MFT by (1) holding each probe-tone frequency constant while quasi-statically sweeping the ear-canal pressure (e.g., Colletti, 1975); (2) holding the ear-canal pressure constant at each value while sweeping the frequency (e.g., Wada and Kobayashi, 1990); or (3), what is usually done now, quasi-statically sweeping the ear-canal pressure while applying multiple stimuli consisting of either chirps (i.e., rapid frequency sweeps; e.g., Funasaka et al., 1984) or clicks (e.g., Keefe and Simmons, 2003). The changes in quasi-static pressure are quite small within the duration of a single chirp or click, leading to the assumption that the pressure remains constant within each such stimulus.

MFT provides information on how components of admittance change with the pressure and with the probe frequency. The resonance frequency of the middle ear changes when the mass and stiffness of the system change, and can, therefore, serve as one of the middle-ear status indicators in the tympanogram. Otosclerosis (e.g., Colletti et al., 1993) and rheumatoid arthritis (e.g., Giannini et al., 1997) increase middle-ear stiffness and subsequently increase the resonance frequency of the middle ear. Ossicular chain discontinuity and otitis media with effusion (i.e., a common middle-ear disorder in which fluid is

built up in the middle-ear cavity) typically decrease the resonance frequency of the middle ear because such conditions decrease the stiffness of the middle-ear system (e.g., Wada et al., 1998; Ferekidis et al., 1999).

Vanhuyse et al. (1975) proposed patterns of tympanograms obtained with normal and pathological ears at 678 Hz. Colletti (1977) investigated the effects of probe-tone frequencies on the shape of the tympanogram for frequencies from 200 to 2,000 Hz. Low-frequency tympanograms were found to be V-shaped, the mid-frequency ones W-shaped, and the high-frequency ones inverted V-shaped. Margolis and Goycoolea (1993) later adapted the Vanhuyse model to higher probe-tone frequencies (up to 2,000 Hz). The number of peaks and troughs in the admittance tympanograms increase as the middle-ear system shifts from stiffness to mass controlled. Although MFT curves contain more information, the coupling of the ear canal and TM becomes complex at high frequencies and therefore adds complexity in interpreting the tympanograms. As a result, MFT is not yet used as a routine clinical hearing test.

3.2.3 Tympanometry in newborns

The overall research programme of which this thesis forms part has a focus on newborn hearing screening. Hearing loss is one of the most common congenital disabilities, and impaired hearing can lead to deficits in language, cognition and social skills. Early detection accompanied by appropriate early intervention is essential. Newborn hearing screening often starts with an otoacoustic emission (OAE) test to check for the cochlear response to sound. The emission of a range of sound frequencies in response to appropriate stimuli indicates proper functioning of the outer hair cells. OAE test results also depend on middle-ear status, because for the cochlea to receive the sound stimuli the middle ear needs to be functional. The middle ear is also paramount in transmitting the OAEs from the cochlea to the TM for the probe to be able to capture them in the ear canal (Kemp, 2002). Newborn hearing

screening sometimes also includes an auditory brainstem response (ABR) test to check for nerve function. Three surface electrodes are placed on the infant's head to record nerve responses. ABR tests provide information about the function of the middle ear and cochlea and the central auditory pathway through the brainstem (e.g., Bogičević et al., 2018). Since both OAE and ABR signals travel through the middle ear, their results may be more most effective when interpreted along with tympanometry measurements (McKinley et al., 1997; Kilic et al., 2012).

The infant ear has substantial anatomical differences from the adult ear (as shown in Fig. 3-3), and such differences greatly affect the interpretation of tympanograms. Postnatal changes in the outer and middle ear that may contribute to the acoustic differences include ossification of the ear canal; enlargement of the external ear, mastoid and middle ear cavity; tympanic annulus fusion; and changes in the ossicular joints (e.g., Qi et al., 2006; Motallebzadeh et al., 2017a). Infants with otitis media may reveal a normal tympanogram when using a 226-Hz probe tone (e.g., Paradise et al., 1976; McKinley et al., 1997; Margolis et al., 2003), while healthy infant ears may produce notched tympanograms at 226 Hz with features generally found at higher probe-tone frequencies in adults (Bennett, 1972; Keith, 1973). As reviewed by Carmo et al. (2013), many groups recommend 1,000-Hz tympanometry for infants under sixth months of age as it offers higher sensitivity for identifying middle-ear disorders in infants and shows better correlations to OAE and ABR screening results. Some groups observed that the 1,000-Hz probe tone gives rise to better results for the characterization of tympanometric patterns when compared to 226-Hz and 678-Hz probe tones (e.g., Calandruccio et al., 2006; de Moraes et al., 2012). Alaerts et al. (2007) compared 226-Hz and 1,000-Hz tympanometry performed on 110 infants up to nine months of age and 15 adults with normal hearing. In infants younger than three months, 91% passed tympanometry screening with a 1,000-Hz probe tone while only 35% passed when using a 226-Hz probe tone. High-frequency tympanometry has been shown to offer better specificity for neonatal

hearing screening, if not better sensitivity. However, due to the ambiguity and complexity of high-frequency tympanograms, there are disagreements concerning a standard for tympanometric patterns and classification parameters.

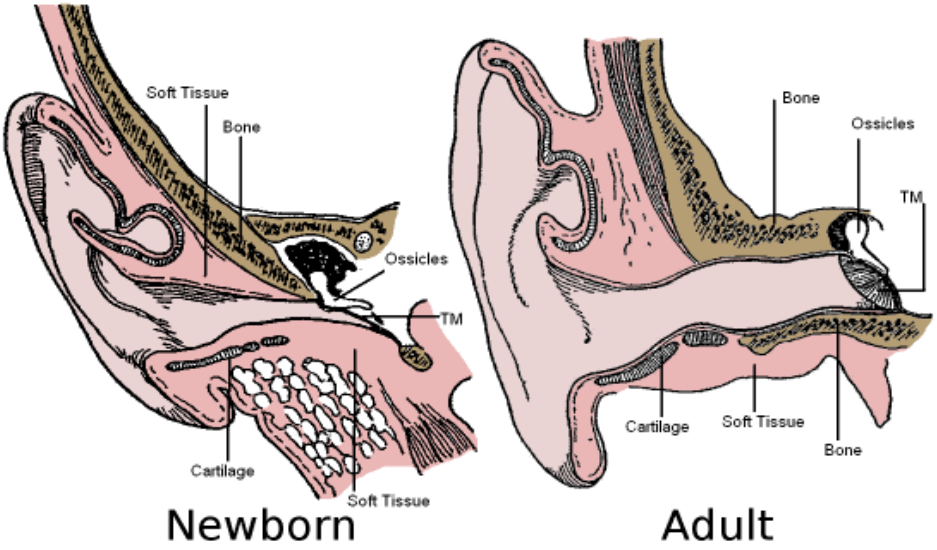

Figure 3-3: Comparison of ear anatomy between newborns and adults (After Fowler EP Jr. (1947): Medicine of the ear, 2nd ed., T. Nelson, New York, from http://audilab.bme.mcgill.ca/teach/me_saf/)

3.3 Finite-element method

In this section, we introduce the finite-element (FE) method and some important concepts for model generation. In section 3.3.1, we define the FE method and its basics. In section 3.3.2, we introduce non-linear and time-dependent models. In section 3.3.3, we give a review of previous middle-ear models.

3.3.1 Introduction

Continuum mechanics treats distributions of physical quantities as continuous functions of position and time and considers their discrete nature to be unimportant. Continuum mechanics applies the fundamental law of motion and derives differential equations that represent the balance of linear and angular momentum of particles in a continuum. It also uses empirical constitutive laws to add information about the particular materials of the continua into the system of equations.

For stress problems, current strategies involve solving analytical equations. The differential equations for a simple system may be easy, but they become very complicated for systems with irregular geometries and with multiple material properties and loading conditions. The use of analytical methods to solve real systems often involves a considerable degree of idealization or approximation.

Numerical methods are appropriate when the behaviour of a system and its surroundings is too complex to be solved as a whole, and no plausible idealization of the system can be obtained. By far the most versatile and widely used numerical method for solving problems in mechanics of materials is the FE method. In the finite element method, the system is divided into a finite number of well-defined components, whose individual behaviour is readily understood and is represented by simple approximations. The history of the FE method used in mechanics probably started in the 1940s when McHenry, Hrenikoff, Newmark, and Southwell showed a reasonably good solution to an elastic continuum problem by dividing it into simple elastic bars (e.g., Zienkiewicz et al., 2013). Here we present a brief description of the FE method based largely on Zienkiewicz et al. (2013).

Obtaining a FE solution involves the following steps:

1. Divide structure into elements with nodes (i.e., discretization or meshing)
2. Assign the material properties, define the boundary conditions, determine loading condition(s)
3. Connect the elements at the nodes to form an approximate system of equations for the whole structure (i.e., forming system matrices)
4. Solve the system of equations involving unknown quantities at the nodes (e.g., displacement)
5. Calculate desired quantities (e.g., strains and stresses) at selected elements

Based on the variational principle (Zienkiewicz et al., 2013, chap. 4), the solution to the continuous problem is a function u which makes the potential energy Π stationary with respect to arbitrary changes δu. Thus, for a solution to the continuous problem, the "variation" is

$$\delta \Pi = 0 \tag{3-2}$$

for any δu, which defines the condition of stationarity.

Frequently, the physical aspects of a problem can be stated directly in a variational form. One of the "natural" variational principles is the minimization of energy. In stress analysis, for example, the variational principle for a continuous body can be obtained by minimizing the total potential energy of the system. The total potential energy Π can be expressed as

$$\Pi = \frac{1}{2}\int_{\Omega} \sigma^{\mathrm{T}} \varepsilon \, \mathrm{d}V - \int_{\Omega} \boldsymbol{d}^{\mathbf{T}} \boldsymbol{b} \, \mathrm{d}V - \int_{\Gamma} \boldsymbol{d}^{\mathbf{T}} \boldsymbol{q} \, \mathrm{d}S \quad , \tag{3-3}$$

where $\boldsymbol{\sigma}$ and $\boldsymbol{\varepsilon}$ are the vectors of the nodal stress and strain components, respectively; $\boldsymbol{d}$ is the vector of displacement; $\boldsymbol{b}$ is the vector of body-force components per unit volume; and $\boldsymbol{q}$ is the vector of applied surface-force components. The volume integrals are defined over the entire region of the domain Ω and the surface integrals are defined over the boundary Γ. Solving the resulting system of linear equations provides the response of the system (e.g., Zienkiewicz et al., 2013, chap. 3).

The FE method can be very accurate if realistic assumptions are made and proper material and boundary definitions are used. There are some factors to be considered to provide an adequate representation of reality:

1. Constitutive equations: The choice of method is based on trade-offs between the computational cost and the required accuracy. The choice of constitutive equations should depend on the natural material behaviour under desired modelling conditions. For example, modelling a rubber using linear isotropic constitutive laws is inappropriate unless strains are small enough.

2. Mesh convergence analysis: The degree of meshing should be analyzed carefully. A coarse mesh may not lead to accurate results, but a very fine mesh can have undesirably high computational cost. Appropriate mesh size is essential to accurate but practical analysis.

3. Material definition: Material parameters should be determined *a priori* as much as possible. Adjusting too many model parameters to fit a set of experimental results will not lead to a reliable model.

4. Boundary conditions, loading conditions and constraints: The interconnections of the system within itself (i.e., between the components of the system) and with the environment (i.e., how the system is situated within its surroundings) are usually very complicated. A successful FE model should represent those conditions in a simplified form but still provide an acceptable representation of reality.

5. Model verification and validation: Model verification refers to the verification of the FE computer code and the mathematical calculations. It may consist of comparing results from the same FE model obtained with different solvers or with other simulation results. Model validation is the process of comparing the FE model simulation results to experimental measurements.

There are many software packages available for FE modelling. Commonly used commercial packages include ANSYS (www.ansys.com/) and ABAQUS (www.3ds.com/products-services/simulia/products/abaqus/). Both of them integrate three steps of modelling, including pre-processing, processing, and post-processing. Free and open-source software is also available and may include all three steps or target specific functions. For example, Salome-Meca (code-aster.org/) is an open-source platform that incorporates sub-modules to include all three steps of modelling. FEBio (febio.org/) is also open source and has specific software for the different modelling steps, including PreView for pre-

processing, FEBio for solving, and PostView for post-processing. Moreover, some software targets geometry and mesh generation (e.g., Fie, Tr3 and Fad at audilab.bme.mcgill.ca/sw/, Gmsh at www.geuz.org/gmsh). There is software that just solves the mathematical equations (e.g., Code_Aster at www.code-aster.org/, SAP IV at https://nisee.berkeley.edu/elibrary/getpkg?id=SAP4, and a locally modified version at http://audilab.bme.mcgill.ca/sw/sap.html). Software for visualizing the output is usually included in the package (e.g., PostView in FEBio and ParaVis in Salome-Meca).

3.3.2 Non-linear and time-dependent material models

In continuum mechanics, non-linearity arises from three conditions: (1) geometrical non-linearities (i.e., when geometry changes because of large displacements), (2) material non-linearities, and (3) contact non-linearities (e.g., Funnell et al., 2017). Modelling tympanometry requires simulation of the middle-ear response to a sound pressure in the presence of large static pressures. In this brief introduction, we only discuss hyperelastic and viscoelastic behaviours.

3.3.2.1 Finite-strain theory

For moderate to large deformations, simulation software uses finite-strain theory to describe the geometric configuration. The following mathematical presentation is largely based on Irgens (2008, chaps. 5 & 7). Let us consider that a particle P_0 and its neighbouring particle Q_0 in the reference configuration Ω_0 are transformed to new positions P and Q in the deformed configuration Ω_f. In the deformed configuration, the two particles are located at $\boldsymbol{y}(\boldsymbol{X})$ and $\boldsymbol{y}(\boldsymbol{X}+\mathrm{d}\boldsymbol{X})$, respectively, and the deformed image of segment PQ is described by the vector

$$\mathrm{d}\,\boldsymbol{y} = \boldsymbol{y}(\boldsymbol{x}+\mathrm{d}\,\boldsymbol{x}) - \boldsymbol{y}(\boldsymbol{x}) \quad . \tag{3-4}$$

Since P and Q are neighbouring particles, we can approximate this expression for small $|dx|$ by the Taylor expansion

$$\mathrm{d}\,\boldsymbol{y} = (\mathrm{Grad}\,\boldsymbol{y})\,\mathrm{d}\,\boldsymbol{x} + \mathrm{O}\left|\mathrm{d}\,\boldsymbol{x}^2\right| = \boldsymbol{F}\,\mathrm{d}\,\boldsymbol{x} + \mathrm{O}\left|\mathrm{d}\,\boldsymbol{x}^2\right| \quad , \tag{3-5}$$

which we can approximate as

$$\mathrm{d}\,\boldsymbol{y} = \boldsymbol{F}\,\mathrm{d}\,\boldsymbol{x} \quad , \tag{3-6}$$

where F is called the *deformation gradient.* The deformation gradient linearly transforms any infinitesimal vector in the undeformed configuration to another infinitesimal vector in the deformed configuration of a body. The *right Cauchy-Green deformation tensor* $\boldsymbol{C}$ arises from mapping the scalar product of two initial infinitesimal vectors and is defined by

$$\boldsymbol{C} = \boldsymbol{F}^{\mathrm{T}}\boldsymbol{F} \quad , \tag{3-7}$$

$\boldsymbol{F}^{\mathrm{T}}$ being the transpose of matrix $\boldsymbol{F}$. Note that $\boldsymbol{C}$ is symmetric. The difference between the initial and modified scalar products gives rise to the *Lagrangian finite-strain tensor* $\boldsymbol{E}$ and the *Green-Lagrangian strain tensor* $\boldsymbol{e}$. The strain tensors are defined by

$$\begin{aligned} \boldsymbol{E} &= \frac{1}{2}(\boldsymbol{C} - \boldsymbol{I}) \text{ and} \\ \boldsymbol{e} &= \frac{1}{2}(\boldsymbol{I} - \boldsymbol{C}) \end{aligned} \quad , \tag{3–8}$$

where $\boldsymbol{I}$ is the unity matrix. The *Lagrangian finite-strain tensor* $\boldsymbol{E}$ can be expanded in terms of the displacement $\boldsymbol{u}$:

$$\boldsymbol{E} = \frac{1}{2}\left[\frac{\partial \boldsymbol{u}}{\partial \boldsymbol{X}} + \left(\frac{\partial \boldsymbol{u}}{\partial \boldsymbol{X}}\right)^{\mathrm{T}} + \left(\frac{\partial \boldsymbol{u}}{\partial \boldsymbol{X}}\right)^{\mathrm{T}} \frac{\partial \boldsymbol{u}}{\partial \boldsymbol{X}}\right] \quad . \tag{3–9}$$

For infinitesimal deformations, the term $\left(\frac{\partial \boldsymbol{u}}{\partial \boldsymbol{X}}\right)^{T} \frac{\partial \boldsymbol{u}}{\partial \boldsymbol{X}}$ is neglected, but for large deformations, this term is kept.

The principle invariants of $\boldsymbol{C}$ are defined as

$$\begin{aligned} I_1 &= \mathrm{tr}(\boldsymbol{C}) = \lambda_1{}^2 + \lambda_2{}^2 + \lambda_3{}^2 \\ I_2 &= \frac{1}{2}\left(I_2{}^2 - \mathrm{tr}(\boldsymbol{C}^2)\right) = \lambda_1{}^2\lambda_2{}^2 + \lambda_2{}^2\lambda_3{}^2 + \lambda_1{}^2\lambda_3{}^2 \\ I_3 &= \det(\boldsymbol{C}) = J^2 = \lambda_1^2\lambda_2^2\lambda_3^2 \end{aligned} \tag{3-10}$$

where λ_1, λ_2 and, λ_3 are called the principle stretch ratios and are the eigenvalues of the deformation gradient, $\boldsymbol{F}$. J is called the Jacobian and represents the volume change ratio. If the material is incompressible, I_3=1; the volume change is negligible and J=1.

3.3.2.2 Hyperelasticity

For large deformations, it is common to use hyperelastic models where the non-linear stress-strain relationship is derived from a strain-energy function. The strain-energy function represents the potential energy stored in the material as a result of deformation. The strain-energy function can be expressed as a function of either strain invariants (I_1, I_2 and I_3) or principle stretch ratios (λ_1, λ_2 and λ_3). The stress tensor and the strain tensor can be calculated based on the strain energy. The stress components can be determined by differentiating the strain-energy function with respect to a strain component:

$$S_{ij}=\frac{(\partial W)}{(\partial E_{ij})}=2\frac{(\partial W)}{(\partial C_{ij})} \tag{3-11}$$

where S_{ij} is the *second Piola-Kirchhoff stress tensor*, E_{ij} is the *Lagrangian strain tensor*, and C_{ij} is the *right Cauchy-Green deformation tensor* (Holzapfel, 2000).

Various strain-energy functions can be applied to soft tissue, such as neo-Hookean, Mooney-Rivlin, Ogden, etc. In our study, we used a generalization of the Mooney-Rivlin method. It was initially proposed by Mooney in 1940 and was expressed in terms of the strain invariants by Rivlin and Rideal in 1948 (e.g., Funnell et al., 2017). The Mooney-Rivlin model has been widely applied to model large deformations in nearly incompressible soft tissues such as skin, brain tissue, breast tissue and, more importantly for our purposes, the TM (e.g., Qi et al., 2008; Soleimani et al., 2020).

In the Mooney-Rivlin model, the strain-energy function is written as

$$W=C_{10}(I_1-3)+C_{01}(I_2-3)+\frac{K}{2}(J-1)^2 \tag{3-12}$$

where C_{10} and C_{01} are material constants, κ is the bulk modulus, and J is the Jacobian. Further details about the hyperelastic model can be found in standard continuum mechanics textbooks (e.g., Holzapfel, 2000).

3.3.2.3 Viscoelasticity

Most soft biological materials exhibit both non-linear and time-dependent (viscoelastic) behaviour (e.g., creep, stress relaxation and hysteresis). The following discussion is primarily based on Govindjee and Reese (1997) and Charlebois et al. (2013). Viscoelastic models can be separated into three groups: linear viscoelastic (LV), quasi-linear visco-hyperelastic (QLVH) and fully non-linear visco-hyperelastic (NLVH). For LV models, the stress is linearly proportional to the strain history. For LV and QLVH models, the elastic elements are considered as hyperelastic, and the stress response is decoupled between time and strain. For NLVH models, the deformation gradient has a multiplicative split into a viscous part and an elastic part. LV and NLVH models are beyond the scope of this work and will not be discussed further. The focus here will be on QLVH models. The QLVH model is a single-integral mathematical model that is an extension of the linear viscoelasticity convolution formulations to handle non-linear viscoelastic materials. The strain-energy function and its derivation can be found in the papers cited above (Govindjee and Reese, 1997; Charlebois et al., 2013).

We first introduce the concept of stress and relaxation. Let us consider a model composed of an elastic branch in parallel with an arbitrary number of viscoelastic branches. The elastic branch only includes one elastic spring element, and each viscoelastic branch includes an elastic spring and a dashpot (damper) combined in series. The combination of these branches is usually referred to as the generalized Maxwell model (illustrated in Fig. 3-4) and provides a generalized relaxation and creep response.

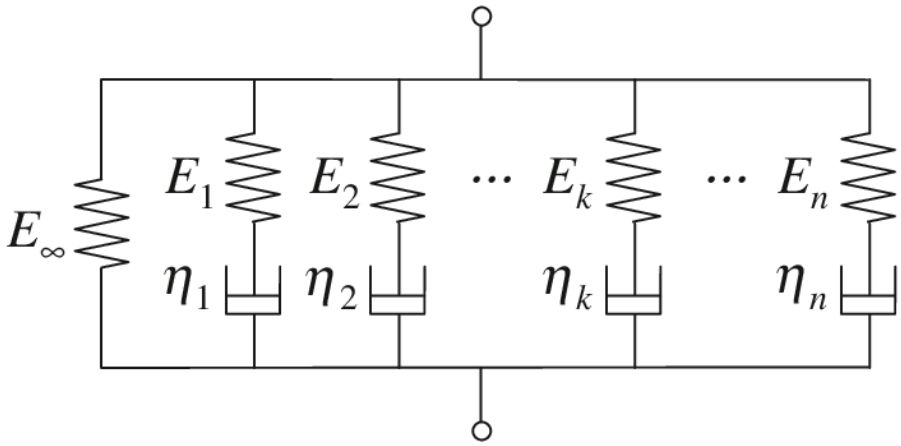

Figure 3-4: Schematic of a generalized Maxwell model (Chae et al., 2010).

Fung (1993) introduced the QLVH model with the assumption that stress depends linearly on the superposed time history of a related non-linear response. The stress response is evaluated by convolving a normalized relaxation function $G(t)$ with the derivative of an elastic response function $\boldsymbol{S}^e$:

$$\boldsymbol{S}(t)=\int_0^t G(t-s)\left(\frac{\mathrm{d}\,\boldsymbol{S}^e}{\mathrm{d}\,s}\right)\mathrm{d}\,s \tag{3–13}$$

where $\boldsymbol{S}^e$ is the instantaneous *second Piola-Kirchhof stress tensor* and can be seen as an equivalent elastic stress; t is time, and s is a dummy variable. $G(t)$ for the generalized Maxwell model is defined by a Prony series. Depending on whether $\boldsymbol{S}^e$ represents the instantaneous or long-term elastic response, $G(t)$ is given by either

$$G(t)=1-\sum_{i=1}^{N} g_i\left(1-\exp\left(-t/\tau_i\right)\right) \tag{3–14}$$

or

$$G(t)=1+\sum_{i=1}^{N} g_i\exp\left(-t/\tau_i\right) \quad , \tag{3–15}$$

respectively. In both equations, g_i (relaxation coefficients) and τ_i (time constants) are material parameters, and N is the number of exponential terms.

3.3.2.4 Viscoelasticity and non-linearity in the TM

The TM has a non-uniform thickness and multiple layers of soft tissues and exhibits a non-linear stress-strain relationship and strain-rate-dependent behaviour.

In the literature, various measurements of the mechanical properties of the TM have been reported. Békésy (1960) measured the Young's modulus (i.e., the elastic modulus) of the human TM to be 20 MPa using a bending test on a rectangular strip of TM modelled as a quasi-static beam. Kirikae (1960) calculated the Young's modulus of the human TM to be 40 MPa based on a dynamic test on a strip of fresh TM. Decraemer et al. (1980) performed a uniaxial tension test on strips of human TM and reported a Young's modulus of 23 MPa. Fay et al. (2005) applied several methods to estimate the material properties of the cat and human TM. First, they used a constitutive model based on known stiffness values of collagen and on observed fibre densities. Then, they used composite laminate theory to reinterprete bending and tensile loading tests to find the range of elastic modulus for the fibre layers. Lastly, they employed a wave-number versus frequency relationship to represent the TM's mechanical structure. From these three methods, they reported the Young's moduli to be between 0.1 and 0.3 GPa for human TM and between 0.1 and 0.4 GPa for cat TM. Their reported values were much higher than previous estimates because they had used a much smaller thickness of the TM that corresponded to only the fibre layers.

In normal hearing (i.e., under low frequencies and low sound pressures), the middle ear behaves linearly, but it becomes non-linear in response to high pressures (i.e., to blast and explosions and in tympanometry). Under these conditions, the soft tissue in the middle ear shows time-dependent behaviour. Fung (1993) discussed common features of soft tissue, including having a hysteresis loop in cyclic loading and unloading, and preconditioning in repeated cycles. Hysteresis is a dynamic phenomenon of soft tissue; the stress-strain curve in the unloading process is different from that in the

loading process. Preconditioning refers to the change in stress-strain curves in successive loading and unloading cycles before the material reaches a steady state after a few cycles. Middle-ear soft tissue also exhibits these phenomena. Cheng et al. (2007a) conducted tensile tests on strips of fresh human TMs to measure their viscoelastic properties. They performed uniaxial tensile, stress relaxation, and failure tests under quasi-static loading conditions and reported Young's moduli (tangent moduli) between 26 and 38 MPa. Preconditioning was observed during successive loading and unloading (see Fig. 3-5). Hysteresis was demonstrated by the non-zero area between the loading and unloading curve within one cycle (see Fig. 3-5c).

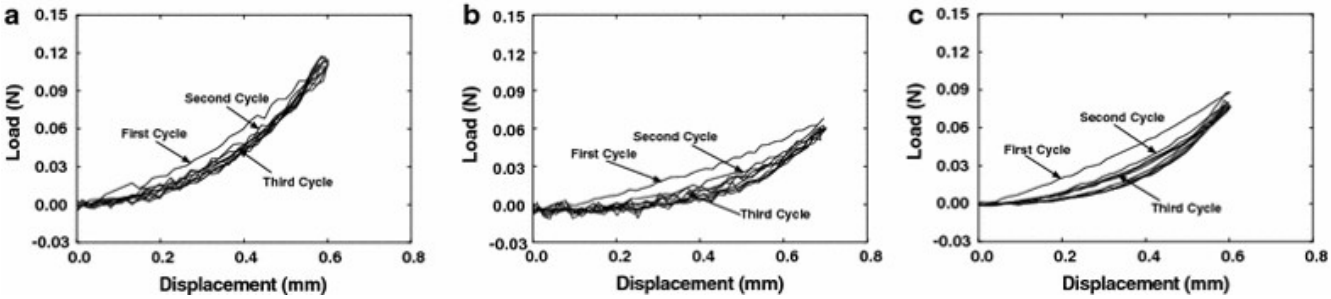

Figure 3-5: Cyclic loading of three TM specimens (a, b and c). Differences between the loading and unloading curves demonstrate hysteresis. Changes in the areas between the curves from cycle to cycle demonstrate preconditioning (Cheng et al., 2007a).

The studies mentioned above assumed the TM modulus to be uniform over the area and thickness of the sample. However, the TM has an inhomogeneous and anisotropic structure, and the measured modulus can differ significantly when the sample is obtained at different locations on the TM. Local measurements, such as nanoindentation, can characterize the TM modulus at different locations and can be used to map the entire TM surface. Huang et al. (2008) established a nanoindentation method to measure both in-plane and through-thickness viscoelastic properties of the posterior and anterior portions of the human TM. They reported the through-thickness Young's modulus to be between 6.2 and 6.8 MPa at steady state and estimated the in-plane Young's modulus to be between 17.4 and 19.0 MPa using a generalized Maxwell model (section 3.3.2.3). The in-plane Young's moduli were similar

to the value of 20 MPa obtained by Békésy (1960). Daphalapurker et al. (2009) used the same technique to measure the Young's moduli of the human TM in four quadrants for both in-plane and through-thickness directions. They obtained Young's moduli of 37.8 MPa and 25.73 MPa in two different human TM samples, which are close to the value (40 MPa) reported by Kirikae (1960) and the value (20 MPa) reported by Békésy (1960), respectively.

Aernouts and Dirckx (2012a) performed an *in situ* sinusoidal indentation test on gerbil TM and obtained Young's moduli between 71 and 106 MPa at an indentation frequency of 0.2 Hz. In a later study (Aernouts and Dirckx, 2012b), they performed step indentation measurements to characterize the viscoelastic properties of the gerbil TM. The obtained data were fitted to a Maxwell model. Later, both types of indentation tests were used to characterize the human TM and resulted in Young's moduli of 2.1 to 4.4 MPa and viscoelastic responses (Aernouts et al., 2012). All of the above measurements were obtained at low strain rates.

Luo et al. (2009a, 2009b) used a split-Hopkinson pressure bar to measure the strain-rate-dependent behaviour of the normal and diseased human TM at higher strain rates, from 300 to 2000 s^{-1} in the radial and circumferential directions. They reported Young's moduli of 45.2 to 58.9 MPa in the radial direction and 34.1 to 56.8 MPa in the circumferential direction and concluded that Young's modulus is strain-rate dependent at high strain rates. Luo et al. (2015) measured the mechanical properties of human TM after exposure to blast waves at high strain rates. The measured Young's moduli were compared to the values they obtained earlier with the intact human TM (Luo et al., 2009a).

Many studies have measured TM properties under high pressures in terms of blast, but these measurements are not relevant to high quasi-static pressures.

Few measurements have been reported for the material properties of the PF. Lim (1968) described the human PF as a continuation of the ear-canal skin, so using the Young's modulus of skin for the PF

may be appropriate. Agache et al. (1980) estimated the average Young's modulus of human forearm skin to be 0.42 MPa in younger subjects and 0.85 MPa in subjects older than thirty years of age.

The ligaments and other soft tissues in the middle ear can also be expected to exhibit viscoelastic behaviour. Gan's group conducted several studies on different middle-ear soft tissues and on the ISJ using a micro-material testing system (Cheng and Gan, 2007, 2008a, 2008b; Gan et al., 2011; Zhang and Gan, 2011). The results show that the middle-ear ligaments, tendons and joints are composed of viscoelastic materials with stress relaxation and hysteresis behaviour.

3.3.3 Finite-element models of the ear

A lumped-parameter model was the first mathematical model of the middle ear. In such a model, each middle-ear component is lumped as an equivalent electrical circuit element (e.g., Zwislocki, 1957). Lumped-parameter models ignore the spatial extents of their components. To address this problem, the development of analytical (e.g., Wada and Kobayashi, 1990) and semi-analytical models emerged (Rabbitt and Holmes, 1986). However, the middle ear is a complicated system containing many interconnected, highly irregular, asymmetrical and non-uniform parts. FE modelling offers the best support to understand such a complex system quantitatively. For a complete review of different approaches to modelling the middle ear, refer to Funnell et al. (2017).

3.3.3.1 Overview of finite-element models of the ear

Funnell and Laszlo (1978) introduced the use of the FE method for the study of the ear. They studied the low-frequency response of the cat TM and developed the first three-dimensional FE model of the TM. In the absence of quantitative shape data, circular arcs were used to represent the curvature of the TM. They assumed a fixed axis of rotation running from the anterior mallear process to the posterior incudal process. This model was extended to higher frequencies by Funnell (1983), investigating the undamped natural frequencies of the TM. Funnell et al. (1987) added the effect of damping on the TM

model. The damping was modelled using mass-proportional Rayleigh damping. The simulation results matched quite well with laser interferometric point measurements on the cat TM (Decraemer et al., 1989). Wada et al. (1992) presented the first three-dimensional FEM of the human middle ear, including the TM and ossicles. They also assumed a fixed axis of rotation, as had been done by Funnell and Laszlo (1978). The model's low-frequency response (below 3 kHz) was comparable to experimental data obtained by time-averaged holography (Tonndorf and Khanna, 1972). An "elastic" boundary condition with linear and torsional springs on the TM annulus, instead of a "fully clamped" condition, was found to produce simulation results closer to experimental data.

The mechanical behaviour of the TM relies heavily on its shape, so reconstructing the realistic geometry of the TM is essential for obtaining a good model. Different imaging techniques have been used to improve the geometrical characteristics of middle-ear models. Funnell and Decraemer (1996) used phase-shift moiré topography to study the shape and deformation of the TM, combined with FE modelling. Daniel et al. (2001) also used moiré shape measurements for the TM, and for the ossicles and ligaments they used histological sections and high-resolution magnetic-resonance microscopy (MRM) data. Sun et al. (2002) used a series of histological images to reconstruct the TM, ossicles, attached ligaments and muscle tendons but could not distinguish between PF and PT. Decraemer et al. (2003) reconstructed the TM and ossicles using x-ray micro-computed tomography (microCT) imaging data. MicroCT imaging techniques allowed a clear observation of TM shape and orientation but could not provide thickness information. Kuypers et al. (2006, 2005) used confocal microscopy to obtain full-field high-resolution thickness measurements of the TM for human and gerbil, respectively. Elkhouri et al. (2006) used a combination of histological sections, microCT and MRM to reconstruct accurate geometries of a gerbil middle ear.

Earlier models assumed linearity and often assumed rigid connections between the ossicles because of the difficulty of creating the models and a lack of experimental data for comparison. With advances in computer hardware and computational power, recent models can process more elements in a shorter simulation time.

A few non-linear FE models of the middle ear emerged, aiming to investigate the effects on the outer and middle ear of the large static pressures that occur during tympanometry or in otitis media. Ladak et al. (2006) made the first non-linear FE model of the middle ear, investigating non-linear deformation of the cat TM considering only geometric non-linearity. They investigated the effects of large static pressures on the displacement of the TM. Their numerical results agreed with experimental shape and displacement measurements made using phase-shift shadow moiré topography (Ladak et al., 2004). They reported that the location of the maximum displacement changes when the pressures are altered, and concluded that geometry alone might be sufficient when simulating the TM response to high pressures.

Qi et al. (2006) developed the first non-linear FE model of a human newborn ear canal and examined soft-tissue deformation in response to high static pressures. Their model included both geometric and material non-linearities and used a hyperelastic constitutive law. In a later model, the same method was used to model the response of the newborn middle ear to high pressures (Qi et al., 2008). Wang et al. (2007) combined static hyperelastic material properties and geometric non-linearities in their human middle-ear model and simulated the dynamic behaviour of the middle ear in the presence of static pressures. Their analysis indicated that the reduced vibration amplitudes of the TM and footplate under positive static pressures was mainly due to material non-linearity, while the reduced vibrations under negative pressures was caused by both geometrical and material non-linearities. Motallebzadeh et al. (2013) modelled the TM as non-linear and viscoelastic. The simulation

results were able to match both the loading and unloading curves with the TM deformation data reported in Cheng et al. (2007b). Choukir (2017) developed the first non-linear middle-ear model that could simulate responses to an acoustic stimulus in the presence of large quasi-static pressures. She simulated the response of the gerbil TM to a 226-Hz pure tone and to a wideband chirp. A fixed axis of rotation was assumed, and the ossicles were simplified as a rigid wedge. The model response to triangular pressure sweeps was validated against experimental data from rabbits (Dirckx et al., 2006; Salih et al., 2016). The present work is an extension of Choukir's model.

Most FE models of the middle ear have been developed for humans. However, animal models are also used in middle-ear modelling because they can be validated with better data obtained *in vivo*. Models have been developed for various species, including cats (Funnell and Laszlo, 1978; Ladak et al., 2006), gerbils (Elkhouri et al., 2006; Maftoon et al., 2015), rabbits (Aernouts et al., 2010) and chinchillas (Ravicz and Rosowski, 2013; Wang and Gan, 2016).

3.4 Experimental measurements

There have been various experimental measurements made to study middle-ear mechanics in multiple species, both *in vivo* and *post mortem*. This section provides a review of previous studies relevant to our research. Section 3.4.1 contains a summary of non-gerbil studies, with an emphasis on human-related studies. Section 3.4.2 reviews experimental studies of unpressurized gerbil TM vibrations. Finally, section 3.4.3 presents experimental measurements made on pressurized TMs, using both acoustic stimuli and quasi-static pressures.

3.4.1 Unpressurized non-gerbil tympanic-membrane vibrations

Funnell and Laszlo (1982) reviewed early experimental measurements of TM vibrations. In this section, we highlight some of the critical studies mentioned in that review and then present more recent studies.

The earliest observations on TM vibrations were done with a magnifying glass, a mirror and mechanical probes. The first observations of TM vibration patterns using laser holography were made by Tonndorf and Khanna (1972) and Khanna and Tonndorf (1972). They used time-averaged holography at frequencies up to 6 kHz. Their method was much more sensitive than earlier methods, allowing lower sound-pressure levels. In both cat and human, they observed maximum displacements in the posterior region of the PT, and the spatial pattern remained simple up to around 2 kHz. For frequencies beyond 2.5 kHz, the simple low-frequency vibration pattern began to break up, and vibration patterns became more complex. Time-averaged, phase-modulated speckle-pattern holography was used by Wada et al. (2002) to study guinea-pig TM vibrations up to 4 kHz. Sinusoidal phase modulation (SPM) allowed measurement of both the amplitude and the phase of the motion of the entire TM. They again reported that complex vibration patterns appeared at frequencies above 2.5 kHz.

Although time-averaged holographic and speckle-pattern measurements offer full-field observations of the TM surface motion in response to sound stimuli, point-by-point laser interferometry provides more precise measurements of the magnitude and phase of the TM motion. Tonndorf and Khanna (1968) developed a laser interferometer and observed the vibration of the cat TM at the umbo. Konrádsson et al. (1987) studied the vibration of the human TM using scanning laser Doppler vibrometry (LDV) and reported data at 578, 3,107, and 3,113 Hz that were consistent with earlier studies. Decraemer et al. (1989) utilized a homodyne laser interferometer and reported the phase and magnitude for a wide frequency range (130 to 20 kHz) for a few points on the cat TM and manubrium. They reported that all points on the PT moved almost in phase for frequencies up to 1 kHz, but the phase differences increased beyond 1 kHz. For frequencies above 5 kHz, each point moves very differently.

Using a computer-assisted fibre-optic-based opto-electric holographic (OEH) interferometer system, Rosowski et al. (2009) studied TM vibrations up to over 20 kHz in human, cat, and chinchilla. They found increasingly complex vibration patterns for frequencies higher than 0.8 kHz for chinchilla and 2 kHz for cat and human. They observed ring-like patterns in chinchilla for frequencies higher than 1 kHz and in cat and human for frequencies higher than 4 kHz. The same group later used stroboscopic holographic interferometry to study the amplitude and phase at a few frequencies in human temporal bones. They applied sound stimuli of 0.5, 1, 4, and 8 kHz and described TM motion as a combination of standing waves and "some smaller travelling-wave like components" (Cheng et al., 2010).

3.4.2 Unpressurized tympanic-membrane vibrations in gerbils

Admittance measurements and LDV measurements have been used to study the gerbil middle and external ear. Some studies examined the input admittance of the gerbil ear in response to acoustic stimuli at different frequencies as an indirect measure of the TM vibration (e.g., Ravicz et al., 1992; Ravicz and Rosowski, 1997; Teoh et al., 1997). Although there have been many experimental studies of the gerbil middle ear, the only measurements of the vibration patterns of the gerbil TM have been those made at a few points on the PT near the umbo by de La Rochefoucauld and Olson (2010) and studies in our laboratory (e.g., Ellaham et al., 2007; Nambiar, 2010; Maftoon et al., 2013, 2014). Ellaham et al. (2007) reported *post mortem* LDV measurements at multiple points on the TM over a frequency range of 0.15 to 10 kHz. Single-point LDV was used to record measurements on glass-coated plastic microbeads at five locations on the TM. Using a similar protocol, Nambiar (2010) performed *post mortem* studies on gerbil TMs but with better hydration techniques as an attempt to reduce the *post mortem* effects of drying. Maftoon et al. (2013, 2014) investigated the *in vivo* vibrations of the gerbil TM using the same protocol. They presented vibration data for two PF conditions: naturally flat, and retracted into the middle-ear cavity. At low frequencies, they reported a shallow minimum and a

shallow maximum in the magnitude plot of the manubrial frequency response, which was explained as the anti-resonance of the PF when in its flat condition. On the other hand, the manubrial response with a retracted PF showed a decreased magnitude and no anti-resonance feature. At higher frequencies, the frequency-response irregularities occur for both PT and manubrium, but are greater for the PT.

3.4.3 Pressurized tympanic-membrane vibrations

3.4.3.1 Tympanometric measurements

Some reports have shown that the direction of the pressure sweep affects admittance measurements (e.g., Decraemer et al., 1984; Kobayashi et al., 1985; Shanks and Wilson, 1986). In bidirectional tympanometry, two different peak pressures are found corresponding to the negative and positive directions of pressure change. The peak pressure difference (PPD) defines the difference between those two peaks. Early studies reported that the PPD was dependent on the pressurization rate (e.g., Feldman et al., 1984; Gaihede, 1996). However, using a modern high-speed tympanometer, Therkildsen and Gaihede (2005) reported a consistent PPD of 120 Pa for four different pressurization rates (50, 100, 200 and 400 daPa/s). They attributed the presence of PPD to hysteresis and associated the early observations of rate dependence to phase delays in the older instruments.

3.4.3.2 Static pressure deformations

To better understand the effects of tympanometry-like quasi-static pressures, the Antwerp group measured the deformation of the gerbil TM under quasi-static pressures in several studies. Von Unge et al. (1993) studied gerbil PT deformation under static pressure using real-time differential moiré topography. They reported hysteresis between the loading and unloading phases and convergence to a preconditioned state after the second cycle. They observed two areas to have large deformation, one in the anterior region of the PT and the other one in the posterior region. As the static pressure was increased, the locations of the areas remained constant. Dirckx et al. (1998) measured volume

displacements of the gerbil PF in response to middle-ear pressures between −2 kPa and +2 kPa. They reported that the displacement of the PF was highly non-linear and did not distinctly increase beyond 800 Pa. Dirckx and Decraemer (2001) studied changes in gerbil TM motion under quasi-static pressure when middle-ear components were removed in sequence. They concluded that the cochlea, stapes and tensor tympani have little to no effect on the TM deformation under static pressure, but the TM deformation is strongly influenced by the ossicles for pressures between 0 and 400 Pa. They also reported that damage to the posterior incudal ligament (possibly induced by exposing the IMJ) changed the TM response to the static pressure. Disruption of the anterior mallear bony attachment also affected the shape of the TM at 0 Pa.

3.4.3.3 Laser Doppler vibrometry measurements

Lee and Rosowski (2001) used LDV to analyze the acoustic behaviour of the gerbil PT and PF in response to middle-ear static pressure sweeps that mimic the pressure changes in clinical tympanometry. They found that a non-zero middle-ear static pressure generally reduces the velocity magnitude of both the PT and PF in response to sound stimuli. Negative middle-ear pressure reduces the velocity magnitude more than positive middle-ear pressure does. They also reported the frequency dependence of the velocity measurements; hysteresis between pressure sweeps in different directions; and asymmetry in the velocity measurements obtained when applying positive and negative middle-ear pressures. Such asymmetry between the effects of negative and positive middle-ear pressures agreed with other studies (e.g., Dirckx and Decraemer, 2001; Dirckx et al., 2006).

In our group, Shapiro (2014) performed preliminary *post mortem* LDV measurements under quasi-static pressure and measured displacements at multiple points on the gerbil TM in response to a chirp over the range of 0.2 to 11 kHz. Using a similar protocol, Kose et al. (2020) reported *in vivo* vibration responses in 11 gerbils under quasi-static pressures. Cycles of static pressure steps over a range of

±2500 Pa in 500-Pa increments were applied to the TM. The pressure was held for 10 seconds at each step, and successive 128-ms chirps from 0.5 to 10 kHz were applied as the acoustic stimulus. They observed that, with increasing static pressure (loading), the magnitude of the frequency response at the umbo decreased, and the resonance frequency shifted towards higher frequencies. They generally observed a somewhat larger magnitude of vibration in the loading phase as compared to the unloading phase, which indicated hysteresis between loading and unloading. We report a comparison of our model response with the pressurized vibration data of Kose et al. in chapter 5.

3.5 Incudostapedial-joint measurements and modelling

The computational cost trade-off in FE modelling requires deliberation. Researchers often take out or simplify geometrically complicated structures like the ossicular chain to reduce the computational cost of their FE models. However, accurate geometry is essential for simulating sound transmission. Under low sound pressures, the middle ear is considered to function as a linear impedance transformer. Under high-intensity sounds, however, the ossicular joints may contribute to additional roles for the middle ear. Of the two middle-ear joints, the IMJ is larger and is thus visualized more clearly than the ISJ when processed with the same imaging modality. The IMJ is also believed to have greater ability to suppress the sound wave peak amplitude, while the ISJ is believed to shift the peak amplitude (Gottlieb et al., 2018). Our group had conducted several studies to model the mechanical behaviours of the ISJ, and therefore, in this work, we chose to focus on the ISJ structure. The function of the IMJ is beyond the scope of this work, so only FE models related to the ISJ will be discussed below.

Wang and Gan (2016) obtained the first experimental measurements on the mechanical properties of the human ISJ and built an FE model to quantitatively examine the effects of the ISJ on middle ear sound transmission. They performed tension and compression tests, stress relaxation tests, and failure

tests on eight human ISJ specimens. They concluded that the frequency-dependent viscoelastic behaviour of the ISJ protects the cochlea from high-intensity sounds.

There have been a few modelling studies of the mechanical behaviour of the ISJ. Ghosh and Funnell (1995) developed a simple FE model of the cat ear that included a single-block representation of the ISJ and investigated the effects of ISJ flexibility. Funnell et al. (2005) used a pedicle-and-joint model to represent the ISJ. The ISJ block had three layers: the lenticular plate, the articulation, and the head of the stapes; together, they were enclosed by a ligamentous joint-capsule structure. Based on examination of histological images of the cat middle-ear, Funnell et al. (2005) assumed the cartilage layers on the two sides of the joint to be in direct contact during acoustic vibration and consequently modelled the joint articulation as a single block of cartilage with a single Young's modulus value. Their modelling results suggested that the ISJ makes a significant contribution to the flexibility of the coupling between the incus and stapes. In this work, we used a similar approach to represent the ISJ.

For moderate sound pressures, FE modelling of the ossicular joints as simple blocks of viscoelastic material has been shown to result in reasonable agreement with experimental data, particularly at low frequencies (e.g., Maftoon et al., 2015; O'Connor et al., 2017). Even for higher frequencies, de Greef et al. (2017) reported that a solid ISJ model and a fluid-interior ISJ model produced similar responses. However, they did comment that the quality of the microCT data certainly limited the structural detail they had for the joint, and that the characteristics of the interior material may not be as significant without further details of the joint geometry. Gottlieb et al. (2018) performed a joint-fusing experiment on human temporal bones to examine the role of the two ossicular joints in sound transmission. They reported three main effects of joint fusion: reduction in peak umbo velocity, elimination of the delay between malleus head and incus body, and increase and shift of the peak amplitude of the stapes velocity. The 3D motion of the ossicular chain was also different before and after joint fusion.

Several FE models of human and gerbil ISJs have been developed by our group in collaboration with observations by Decraemer's group. They observed non-linearity and strong asymmetry in experimental quasi-static tension and compression tests and developed FE models to reproduce the ossicular chain motion under such conditions. Soleimani et al. (2018) developed a simplified analytical model of the ISJ, modelling the joint capsule as a cylindrical membrane, and studied the mechanical behaviour of the joint. They concluded that the non-linear asymmetric behaviour might be due to mechanical instability of the joint capsule that is governed mainly by the joint-capsule length and the amount of synovial fluid in the joint. Soleimani et al. (2020) studied the effect of synovial membrane curvature and compared the model behaviour to the measurements of Zhang and Gan (2011). They replicated the uniaxial tension and compression tests done experimentally on the human ISJ and found that the geometry of the joint has a significant effect on its function.

Chapter 4: Methods

4.1 Introduction

In this chapter, we present details of our FE model. In section 4.2, we describe the geometry and mesh of the model. In section 4.3, we explain how the boundary conditions are defined. In section 4.4, we report the material properties of the model components. In section 4.5, we present the rationale for the loading conditions and the time-step analysis.

4.2 Geometry, model components and mesh

The 3D geometry of the model is an update of the geometry used by Choukir (2017), which was a simplification of the geometry used by Maftoon et al. (2015). A dynamic non-linear viscoelastic analysis was performed by Choukir, and the model's responses to long quasi-static pressure sweeps, ramps and sinusoids in combination with acoustic stimuli were evaluated. For slowly varying static pressures waves, it is necessary to calculate 2 to 3 minutes of simulated response, requiring millions of time steps. Considering that the acoustic chirps have frequencies up to 10 kHz, the time step for simulations that have both the quasi-static pressure and the acoustic stimuli should be on the order of 20 μs to model the response to high frequencies adequately. Taking into account the small time step needed and the long duration of the simulation, Choukir decided to simplify Maftoon's model for preliminary studies of the model's response under the conditions of tympanometry. The ossicles and ligaments were replaced by a wedge and block structure. Maftoon's mesh was simplified from 50000 second-order solid elements to 18000 second-order solid elements in Choukir's mesh. However, this oversimplification of the ossicles may result in missing details in the middle ear response. As mentioned in section 3.5, studies have suggested that the contributions of the ISJ to the middle-ear response to high quasi-static pressures and high-frequency sound pressures should be examined.

Therefore, we decided to add the ISJ, the stapes and their surrounding structures to Choukir's model. We also added components representing ligaments to the model to reflect more realistic boundary conditions of the middle ear.

The complete middle-ear model of Maftoon et al. (2015) was segmented from a microCT data set, supported by histological images. When first developing the model geometry, Elkhouri et al. (2006) and Maftoon et al. (2015) used in-house pre-processing software (i.e., Fie, Tr3 and Fad) to perform image segmentation and surface tesselation. The open-source software Gmsh (Geuzaine and Remacle, 2009) was then used for volume mesh generation and mesh optimization. Choukir (2017) replaced the middle-ear ossicles with a wedge defining a fixed axis of rotation and an equivalent ossicular mass. A block structure was added to provide an equivalent ossicular stiffness. Fad was used by Choukir to export the 3D mesh to text files that could then be imported into open-source FE pre-processing software, Salome-Meca (2016) and Preview (v1.20.4). Choukir used two FE solvers (Code_Aster v12.7 and FEBio v2.6.4) for model verification. These two FE packages are powerful and well-supported. Our group has developed FE models with them in many studies (Code_Aster: e.g., Maftoon et al., 2015; Motallebzadeh et al., 2017b; FEBio: e.g., Motallebzadeh et al., 2013; Soleimani et al., 2020). Choukir verified that both solvers performed well in simulating models with dynamics, non-linearity and viscoelasticity.

The model we present here includes, in addition to the PT, PF and manubrium, several structures replacing Choukir's wedge and block: two wedge structures representing the malleus and part of the incus; the pedicle; the lenticular plate; the ISJ; and a block representation of the stapes (see Fig. 4-1). The model also includes discrete elements, including springs that represent the anterior mallear process, the posterior incudal ligament, and the stapedial annular ligament; and dashpots that account for the cochlear load. Geometry modification and component insertion were performed in Salome-

Meca (2017). Fad was also used to convert the 3D mesh of Code_Aster to text files that can be read by FEBio. PreView and MATLAB were used to edit some of the boundary conditions and material properties. Code_Aster (v14) and FEBio (v2.9.1) were used as the solvers. Code_Aster has both a linear solver and a non-linear solver, and we used its linear solver (operator DYNA_LINE_TRAN). FEBio only has a non-linear solver but can be used to simulate model responses to small amplitude inputs in the linear regime.

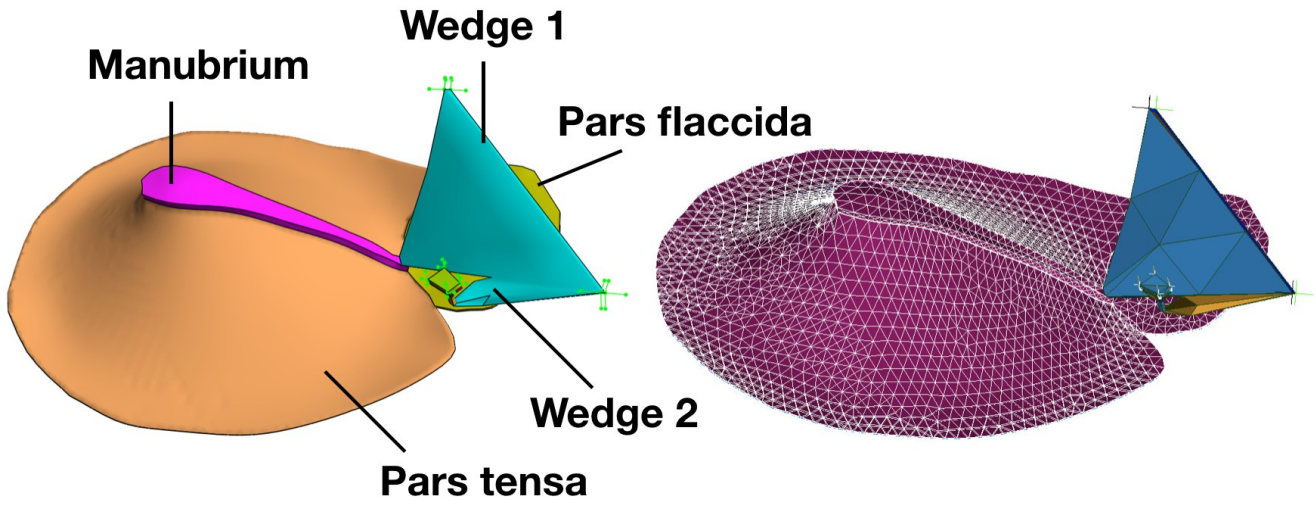

Figure 4-1: FE model of gerbil middle ear. A: FE model in PreView. B: FE model in Salome-Meca.

We used two FE solvers but with different models and for different purposes. We observed, as had Choukir, that FEBio's parallelism can greatly reduce the computation time for the non-linear analysis. Therefore, we decided to only use Code_Aster for linear analysis and for adjusting baseline model parameters. Upon verification of the linear model in Code_Aster by comparison with Maftoon (2015), we then converted the model to FEBio and verified the FEBio model by comparing its response in the linear regime to that of the Code_Aster model. (This is discussed further in section 4.4.) After that, we performed simulation of the model's response to quasi-static pressures using FEBio.

As discussed in section 3.3.2.4, the TM is an inhomogeneous structure composed of multiple layers and with anisotropy in the radial, circumferential and through-thickness directions. However, in this study, we assumed the TM to be homogeneous and isotropic. This has been effective in many other middle-ear modelling studies, including Maftoon et al. (2015) and Choukir (2017).

In the model of Maftoon et al. (2015), the TM was modelled using Code_Aster's seven-node second-order TRIA7 COQUE_3D shell elements. The PT had a variable thickness calculated using an interpolation algorithm developed to reconstruct a thickness map based on the measurements of Kuypers et al. (2005), who reported thicknesses along four lines across the PT and eight lines across the PF in the gerbil, as shown in Fig. 4-2. In Choukir's model, the TM thickness was taken to be the mean of what was used in the model of Maftoon et al., namely, constant thicknesses of 15.78 um for the PT and 23.5 μm for the PF. These mean TM thickness values are similar to the measurements obtained in gerbils by Teoh (1997) (i.e., 19.1 ± 3.2 μm for the PT, and 32.2 ± 12.7 μm for the PF). The manubrium was modelled with a larger thickness, 80 μm, to ensure its rigidity under both quasi-static and acoustic pressures.

Unfortunately, the shell elements in Code_Aster do not support material non-linearity. Moreover, testing shell elements in FEBio led to abnormal behaviour in dynamic analysis. On the other hand, solid elements in both FEBio and Code_Aster do support material non-linearity and agree well with analytical solutions. Choukir (2017) first converted the second-order shell elements in the model of Maftoon et al. to first-order shell elements and then extruded them along the element normals using Code_Aster's COQU_VOLU subfunction in the CREA_MAILLAGE module. The PT was extruded as one layer, the PF as two layers and the manubrium as three layers. Higher-order elements are less stiff than first-order elements and therefore give better displacement predictions and have better convergence rates. The model of the TM and manubrium was made with ten-node second-order

tetrahedral solid element in both FEBio (tet10) and Code_Aster (TETRA10). Choukir tested the effect of the number of layers in the PT, PF and manubrium and found that with a maximum of 4 layers for the PT, 5 layers for the PF and 6 layers for the manubrium, all of the configurations produced similar results. Choukir's model of the TM and manubrium were adopted for our model.

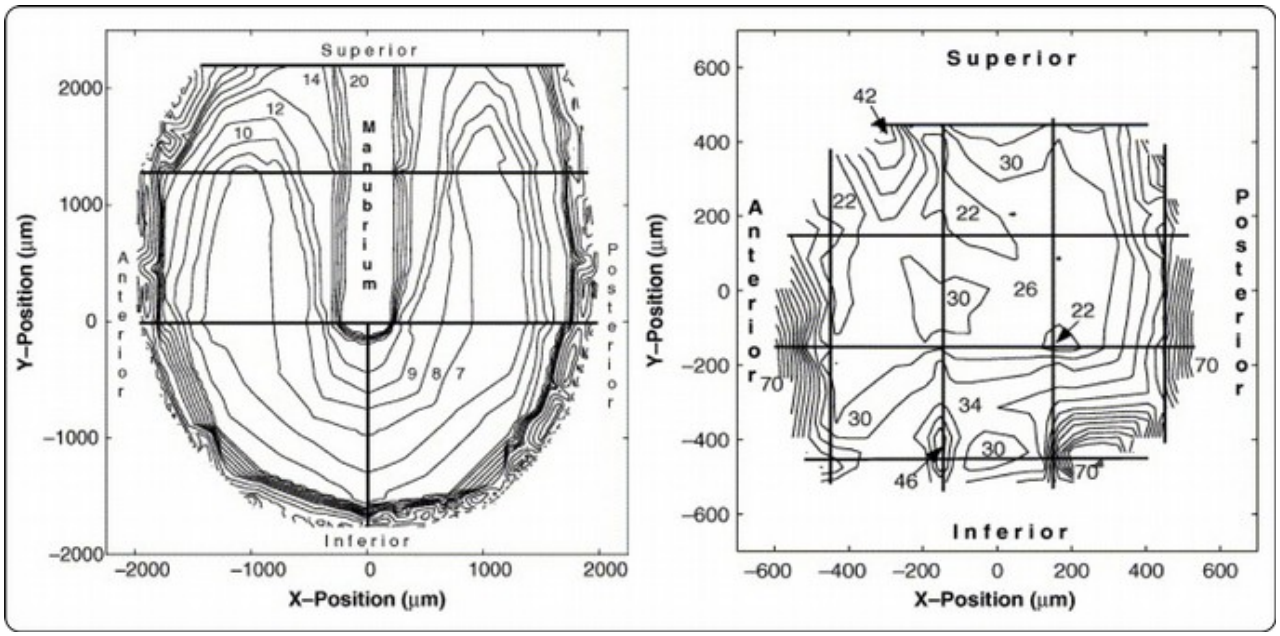

Figure 4-2: Contour plots of the thickness distribution of a gerbil TM. A: PT; B: PF (Kuypers et al., 2005).

In the model of Choukir (2017), the effective load exerted on the eardrum by the ossicular chain was modelled by stiff tetrahedral elements (i.e., the "wedge"). A fixed axis of rotation was defined by two points corresponding to the most anterior point on the anterior mallear process and the most posterior point on the posterior incudal process. The coordinates of these two points were taken from the model of Maftoon et al. (2015). Inspired by Funnell et al. (2005), the block structure in the Choukir model that represented the stiffening effect of the middle-ear ligaments was removed and replaced by new structures explicitly representing the pedicle, the lenticular plate, the ISJ and the stapes (see Fig. 4-3). Crude hexahedral representations were created by connecting nodes extracted from the model of Maftoon et al. for each of the aforementioned structures. The stapes head, crura and footplate are all

combined into a single hexahedron. The hexahedron between the pedicle structure and the original wedge in the Choukir model was reshaped as a second wedge (wedge 2) to facilitate its attachment to the Choukir model (see Fig. 4-1). We refer to the wedge adopted from Choukir's model as wedge 1 to differentiate between the two structures. Both wedges are given the same material properties.

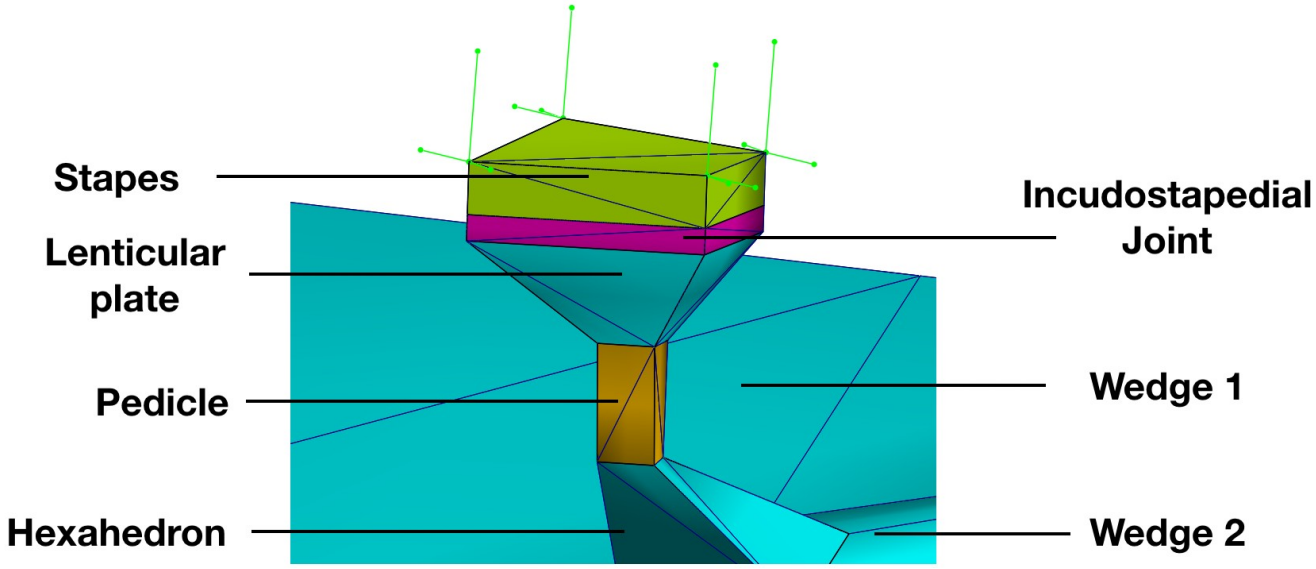

Figure 4-3: A zoomed-in view of the model, showing the wedge 1, the wedge 2, the pedicle, the lenticular plate, the ISJ, the stapes and the springs and dashpots.

To model the effects of the anterior mallear process and the posterior incudal ligament, two sets of springs extending in all three translational directions were placed at each end of the wedge (see Fig. 4-4). The medial two sets are assumed to be rigid (i.e., having very high spring constants, equivalent to clamping the nodes that they are attached to) while the lateral two sets provide the effective ossicular stiffness. To model the stapedial annular ligament, a set of springs is placed at each of the four corner nodes on the top (medial) surface of the stapes structure to represent the stapedial annular ligament. To model the cochlear load, four dashpots are placed at the same four nodes to apply viscous damping to the model. A similar approach to the load on the stapes was used by Maftoon et al. (2015). To ensure consistency in node numbering, we converted the model in Salome-Meca's *mesh* module from quadratic to linear before updating the geometry. The modified middle-ear model was

then converted into a text-only mesh file with Salome-Meca's mesh converter in ASTK. Following that, the text file was imported into Fad and exported to a mesh in the FEBio format. We then used the *convert* function in PreView to transform the FEBio mesh from linear to quadratic.

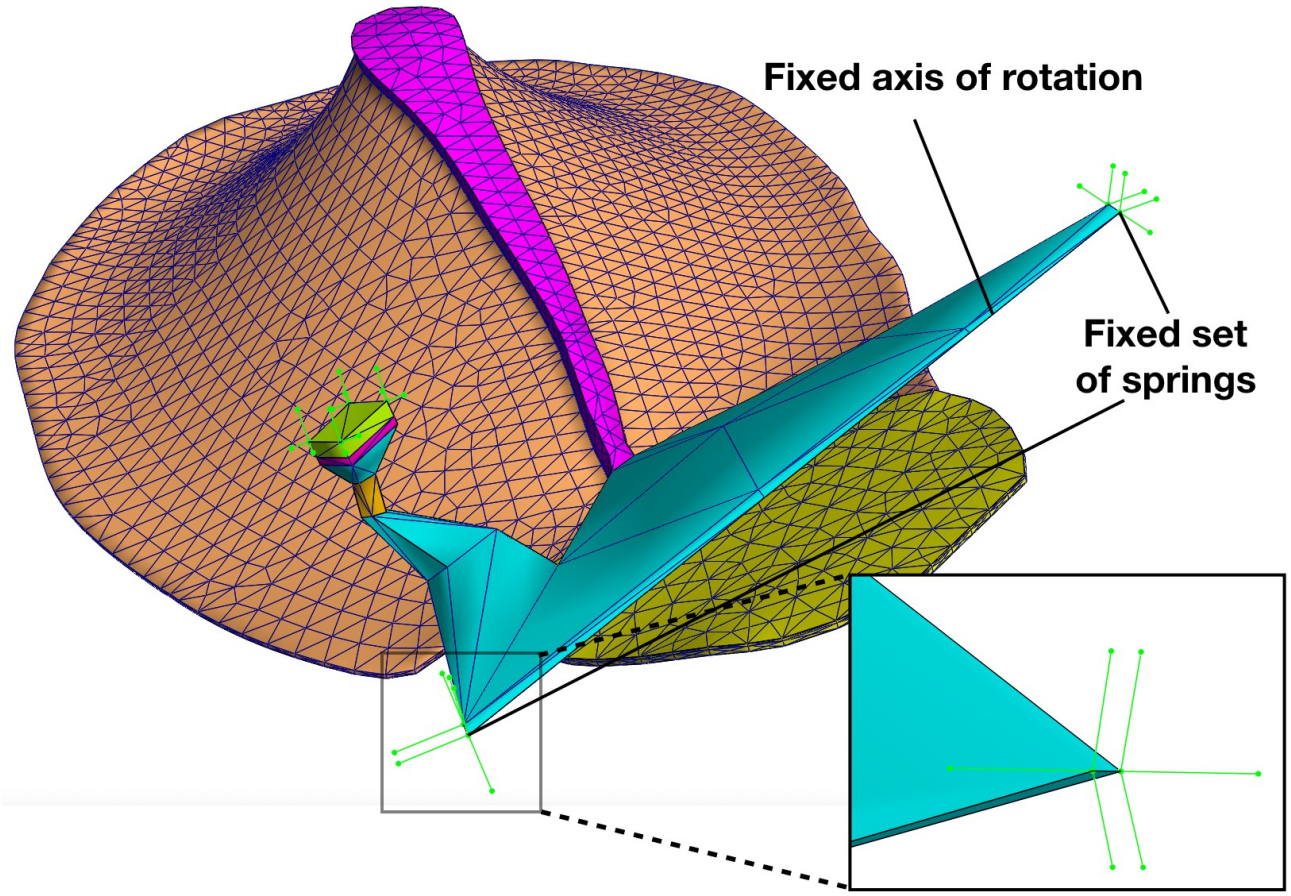

Figure 4-4: Illustration of the boundary conditions at the wedge and the springs. The box shows a close-up view of the two sets of springs at one end of wedge 1.

The original mesh of the middle-ear model (including the PT, PF, manubrium and wedge) in Choukir's model consisted of about 14600 tetrahedral elements and about 28000 nodes. Her model was a simplification of the model of Maftoon et al. (2015), which had around 80000 nodes. Mesh convergence was performed by Choukir using Code_Aster's Homard utility to refine the mesh by dividing each tetrahedral element into eight smaller tetrahedral elements. She performed two iterations

of refinement to the mesh and compared the umbo displacement magnitude in response to sound pressures for each refinement. The first refined mesh resulted in an increase in the displacement magnitude at the umbo of less than 1.4% for frequencies below 200 Hz, less than 3% for frequencies between 200 and 2000 Hz, and less than 5.3% for higher frequencies. The original mesh was chosen for further study. The other structures were made very coarse because their shape was not intended to be realistic and (except for the ISJ block) they were effectively rigid. Since we adopted the complete mesh of the TM from Choukir's model, we also chose to perform the subsequent analyses with the original mesh.

Simulations using the non-linear solver in FEBio are computationally costly and were thus mostly done on the supercomputer Beluga of Compute Canada. Beluga is a cluster of Intel Gold 6148 Skylake 2.4-GHz processors connected by a Mellanox Infiniband EDR network. Such simulations were performed using six processors to take advantage of FEBio's parallel solver using OpenMP and we requested 10 GB of RAM. Instead of showing improvements in run time, an increase in the number of processors beyond six resulted in decreased performance because the software wasted time in data allocation. A simulation for one set of parameters for obtaining 0.153 s of model response to a combination of acoustic stimulus and static pressure lasted about 32 hours. Simulations of a low-amplitude acoustic input using the linear solver in Code_Aster and the non-linear solver in FEBio were performed using one processor and 4 GB of RAM, and took about 1.5 hours with Code_Aster's linear solver and 6 to 7 hours with FEBio's non-linear solver.

4.3 Boundary conditions

To model the constraints provided by the ligaments in the middle ear, we applied several boundary conditions to the model. The PT and the PF were considered to be fully clamped around their

peripheries. This choice of considering the TM to be firmly anchored to the bony tympanic ring around its entire circumference represents an approximation of the TM anatomy.

As mentioned in the previous section, we assumed a fixed axis of rotation between the two points defined by the most anterior node and the most posterior node (Fig. 4-4). The two ends of the inferior edge are fixed in space by the medial two sets of springs with very high spring constants (1000 N/m). The lateral two sets of springs provide finite ossicular stiffness and are given spring constants of 10 N/m (both in Code_Aster and in FEBio).

The four sets of springs representing the stapedial annular ligament are connected to the stapes on one end and fixed in space in all three translational degrees of freedom on the other end. In the Code_Aster model, the spring constant was defined to be 52 N/m by matching the low-frequency magnitude at the umbo to that of the model of Maftoon et al. In the FEBio model, the spring constant was adjusted to 55 N/m. (This difference was presumably because damping was modelled differently in Code_Aster and FEBio.)

4.4 Material properties

Because of the scarcity of data available for the material properties of the gerbil middle ear, all of the parameters describing the material properties of the components had to be estimated. Most of the parameters were adopted from the models of Maftoon et al. (2015) and Choukir (2017), and the rest were taken from the literature as mentioned below. To establish the baseline model in Code_Aster, we evaluated the dynamic response of our model to a unit-step sound pressure and compared the resulting frequency responses with those from the validated linear gerbil middle-ear model of Maftoon et al. (2015). That model was validated against experimental data obtained by the same author (Maftoon et al., 2014) and against those measured by other groups (Lee and Rosowski, 2001). After converting the model to FEBio (with the same geometry), we first adopted the viscoelastic material properties from

Choukir's model and then adjusted them by comparing the model's frequency responses (again based on a unit-step response) with those from our Code_Aster model. In the rest of this section, we report the material properties for both the Code_Aster model and the FEBio model.

4.4.1 Tympanic membrane

4.4.1.1 Governing equations

As mentioned in section 3.3.2.3, we used a QLVH model similar to that of Choukir (2017) and Motallabzadeh (2013) and assumed linear viscosity and non-linear elasticity (hyperelasticity). The governing equation of the linear viscoelastic material property is given by equation 3-13, and the relaxation function is defined by equation 3-14 or 3-15, depending on whether the response is instantaneous or long-term. To model the material hyperelasticity, we chose to use the Mooney-Rivlin model, of which the strain-energy function is composed of deviatoric and volumetric energies (i.e., energy due to distortion and to change of volume, respectively) and is given by

$$W = C_{10}(\bar{I}_1 - 3) + C_{01}(\bar{I}_2 - 3) + W_{\text{vol}}(J) \quad . \tag{4-1}$$

C_{10} and C_{01} are material coefficients. $W_{\text{vol}}(J)$ defines the volumetric change of the energy function in the form of

$$W_{\text{vol}} = \kappa(\ln J)^2 \quad . \tag{4-2}$$

W_{vol} is assumed to be negligible in nearly incompressible tissue (e.g., Humphrey, 2003). The bulk modulus κ is set high enough to make W_{vol} very small. The terms $\bar{I}_1$ and $\bar{I}_2$ are the invariants of the deviatoric part of the right Cauchy-Green deformation tensor and are related to the strain invariants as follows:

$$\begin{aligned} \bar{I}_1 &= J^{\frac{-2}{3}} I_1 \\ \bar{I}_2 &= J^{\frac{-4}{3}} I_2 \end{aligned} \quad . \tag{4-3}$$

Material properties for a hyperelastic material can be determined experimentally. The deviatoric properties can be determined by performing an unconfined tensile or compression test, and the volumetric part can be defined by performing a confined compression test. Under small strains, assuming incompressibility, the equivalent Young's modulus is given (e.g., Hackett, 2015, chap. 4) by

$$E = 6\left(C_{10} + C_{01}\right) \quad . \tag{4-4}$$

The QLVH model is readily available in FEBio.

4.4.1.2 Hyperelastic parameters

As shown in section 3.3.2.3, there are two possibilities for characterizing the elastic part in equation 3-13: the instantaneous response or the long-term response (equations 3-14 and 3-15, respectively). In those two limiting conditions, the viscosity of the material does not contribute to its response. However, it is not possible to directly measure either the instantaneous or the long-term response for practical reasons (Wu et al., 2003). For example, loading tests on the TM are not fast enough to provide an instantaneous response and do not last long enough to provide a long-term response. Therefore, the viscosity of the material actually affects the shape of the stress-stretch curve. If the parameters obtained from fitting the Mooney-Rivlin model to the experimental data were used as the instantaneous response of the hyperelastic part of the QLVH model, the resultant stress-stretch curve would be lower than the experimental data. On the other hand, if the fitted hyperelastic parameters were used as the long-term response, then the resultant stress-stretch curve would be higher than the experimental data. In either case, the Mooney-Rivlin parameters must be adjusted to reproduce the experimental curves (e.g., Motallebzadeh et al., 2013). Choukir chose to take the elastic part of the model to be the instantaneous elastic response, and the Prony series of equation 3-15 was therefore used as the time-dependent part.

Choukir (2017) obtained the parameters in Table 4-1 for her FEBio model by matching the responses at the umbo and at the centre of the PF with those from the model of Maftoon et al. (2015).

For the PT, these Mooney-Rivlin coefficients correspond to a small-displacement Young's modulus (obtained from equation 4-4) of 9.9 MPa, very close to the 10 MPa used by Maftoon et al. (2015). Choukir found model responses to both acoustic pressures and quasi-static pressures to be insensitive to different ratios of C_{10} to C_{01} as long as the sum was kept constant at 1.68 MPa. This is consistent with the result of Qi et al. (2008), who used the Mooney-Rivilin model for the soft tissue in a newborn middle-ear model. They also found the different ratios of C_{10} and C_{01} to have little effect on model displacements in response to static pressures of ±3 kPa. A 3:1 ratio of C_{10}:C_{01} was adopted here, giving the values of C_{10} and C_{01} shown in Table 4-1.

Table 4-1: Estimated parameters for the Mooney-Rivlin model

	Estimated parameters		
Component	C_{10} (MPa)	C_{01} (MPa)	K (MPa)
PT	1.0708	0.6071	167.785
PF	0.0812	0.0406	12.18

The density of the PT was defined to be 1300 kg/m^3, as in the model of Choukir. This value is beyond the range from the density of water (1000 kg/m^3) to that of undehydrated collagen (1200 kg/m^3), as suggested in Funnell and Laszlo (1982). It was adopted by Choukir in order to match the resonance frequency obtained by Maftoon et al. (2015) at the umbo and at points on the anterior and posterior PT. Alternatively, we could have reduced the effective Young's modulus by reducing the sum of the Mooney-Rivlin coefficients. In that case, we would have had to adjust the ossicular load to stiffen the response at the lower frequencies. For consistency we have used Choukir's value.

The density of the PF was defined to be 1100 kg/m^3. The Mooney-Rivlin coefficients were taken to be C_{10}=0.0812 MPa and C_{01}=0.0406 MPa, as in Choukir (2017), which correspond to a small-displacement Young's modulus of 0.74 MPa, compared to 2 MPa as used by Maftoon et al. (2015). The

difference between the two Young's moduli is attributed to the difference in boundary conditions between the two models. In this model and the model of Choukir, the PF boundary was fully clamped, while in the model of Maftoon it was simply supported. Choukir calculated that the change of the boundary condition from simply supported to fully clamped reduced the Young's modulus by a factor of about 3.8. The Young's modulus of 0.7 MPa used by Choukir is about a factor of 2.9 smaller than that used by Maftoon (2015).

The bulk modulus was taken to be 167.785 MPa and 12.18 MPa for the PT and the PF as in Choukir (2017), respectively. The values were calculated with a Poisson's ratio equal to 0.49. It was also confirmed that changing the bulk modulus by decreasing the Poison's ratio to 0.45 did not have a noticeable effect on the model's frequency response.

4.4.1.3 Viscoelastic parameters

In wideband tympanometry and LDV experiments, the acoustic stimulus is usually within the range of 0.2 to 10 kHz. The linear rate of change of the quasi-static pressure in tympanometry and in sweep pressurization experiments on the middle-ear vary from ±50 Pa/s to ±4000 Pa/s. In our study, we only examined the response of the middle ear to pressure rates of change from ±200 Pa/s to ±1500 Pa/s, which is equivalent to a frequency range from 20 mHz to 150 mHz.

To cover the range from the ultra-low frequencies (20 mHz) of the quasi-static pressure variations to the high frequencies (10 kHz) of the acoustic stimulus, for both the PT and PF, six time constants were predefined. (The number is limited to six by FEBio.) The inverse of each time constant corresponds to an angular frequency (because $\omega_i=1/\tau_i=2\pi f_i$) for which the damping represented by the coefficient (g_i) is maximum. A common practice is to take one time constant per decade in the time domain or in the frequency domain (e.g., Knauss and Zhao, 2007; Charlebois et al., 2013). Therefore, for the six time constants, we used constants ranging from 10 μs to 52 s that are approximately equally logarithmically

spaced to cover the frequency range of interest. In this case, the six time constants are about two decades apart from each other: τ_1=10 μs, τ_2=220 μs, τ_3=5 ms, τ_4=10 μs, τ_5=2.3 s and τ_6=52 s.

Each Prony-series time constant is associated with a relaxation coefficient, which represents the amount of damping at the corresponding frequency. As discussed in section 3.3.2.3, for an *n*-term series, the sum of the *n* relaxation coefficients needs to be less than or equal to 1 (Simo and Hughes, 1998). A common feature of the hysteresis of soft tissues is its insensitivity to frequency, with a more or less flat relaxation spectrum over a wide range of frequencies, as shown in Fig. 4-5. This suggests that one should consider equal relaxation coefficients for all of the time constants. Thus, taking into account the constraint on the sum of the relaxation coefficients (Eq 3-15), each of the six equal coefficients must be greater than 0 and less than or equal to 1/6 ≈ 0.167. Choukir compared the linear dynamic response of her model to that of the model of Maftoon and decided on a coefficient of 0.07 for all time constants. Fig. 4-6 shows a comparison using a coefficient of 0.035, 0.07 and 0.14 for all time constants. We can observe that increasing the coefficient increased damping at all frequencies, as expected, although the differences were fairly small. As done by Choukir, we also adjusted the relaxation coefficient related to the time constant 220 μs for the PF to 0.4 to better represent the damping present in Maftoon's model at the centre point of the PF. Increasing the coefficient to 0.4 was justifiable because the new sum of the time constants, 0.75, still respects the constraint that the sum of all the time constans should be less than or equal to 1.

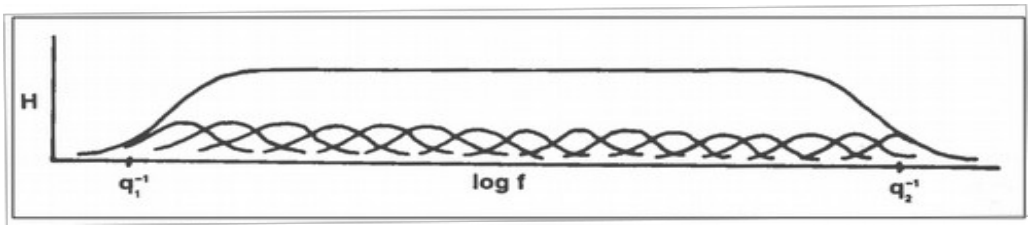

Figure 4-5: Typical hysteresis-log frequency relationship for living soft tissues. Each small bell-shaped curve corresponds to the contributions of one Prony series term (gi, τi). The sum is almost flat over a wide range of frequencies (Fung, 1993).

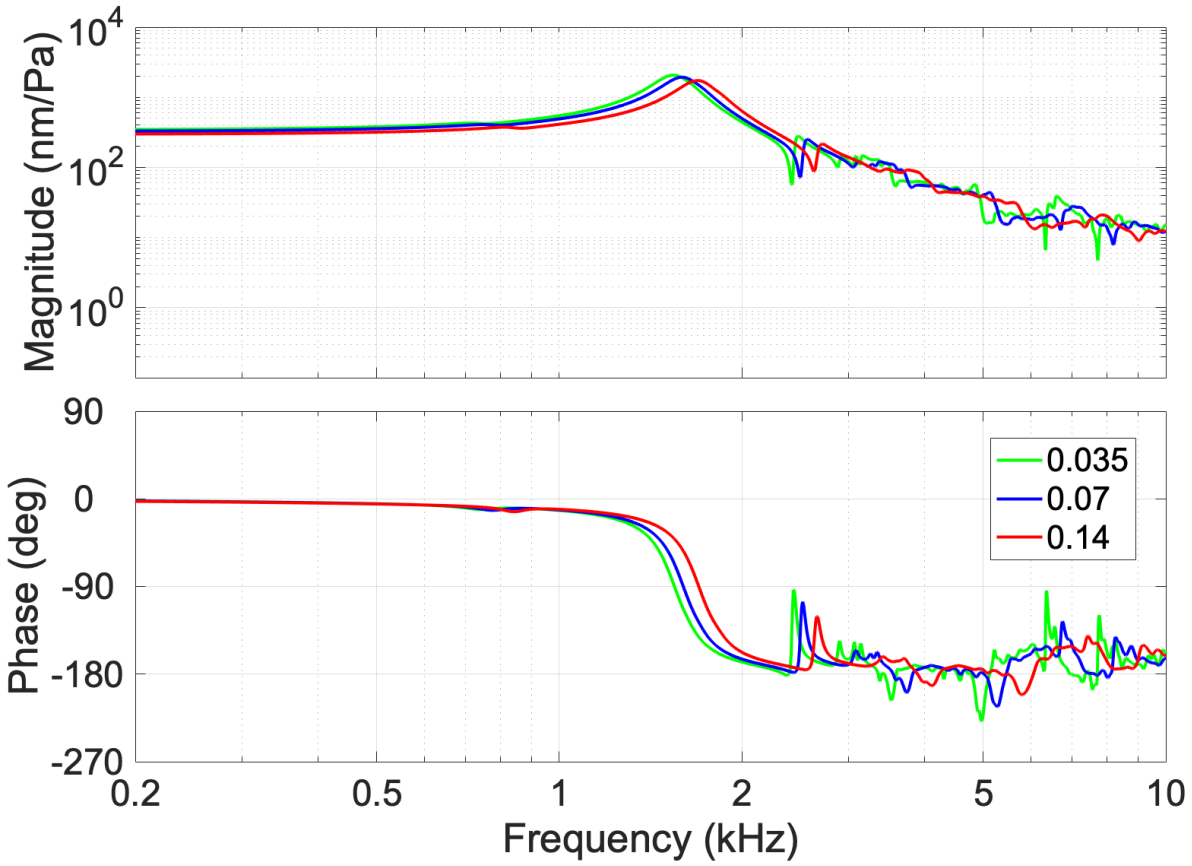

Figure 4-6: A comparison of the FEBio model frequency response when using a coefficient of 0.35, 0.07 or 0.14 for all time constants.

In our Code_Aster model, the TM was defined as linear elastic, and Rayleigh damping was used for all model components. The material properties are mostly adopted from those used by Maftoon et al. and Choukir. The Young's modulus was taken to be 10 MPa for the PT and 2 MPa for the PF, as used in the model of Maftoon et al. The Poisson's ratio was taken to be 0.49 for soft incompressible materials. The density of the PT was taken to be 1100 kg/m^3, and the density of the PF was taken to be

1300 kg/m^3, both adopted from Choukir's model. Rayleigh damping is a mathematical representation of the damping matrix that linearly combines the stiffness matrix and the mass matrix. It is described by $\alpha\mathbf{M} + \beta\mathbf{K}$, where **M** is the mass matrix and **K** is the stiffness matrix. As suggested by Maftoon et al. (2015), we assumed stiffness-proportional damping (i.e., α=0) for all middle-ear structures. We used a damping parameter β of 2×10^{-6} s for the structures with highly organized collagen fibres (i.e., the PT) and 3×10^{-5} s for the structures with abundant elastic fibres (i.e., the PF).

4.4.2 Manubrium, wedges and pedicle

In the Code_Aster model, the manubrium, wedge and pedicle were modelled as isotropic elastic materials. The elasticity of an isotropic linear material is completely described by the Young's modulus and Poisson's ratio. We determined the Young's moduli of the manubrium, wedge and pedicle to be 16.0 GPa by trial and error by matching the frequency-response magnitude of the umbo at low frequencies to that of the model of Maftoon et al. (2015) and Choukir (2017). This value is close to the Young's modulus used in the model of Choukir (14.5 GPa) and the same as the value used in the model of Maftoon et al. (16.0 GPa). The Poisson's ratio is set to be 0.3 for these structures. The density of these structures is set to be 1100 kg/m^3, as in the model of Choukir. This value is lower than the ones used in the model of Maftoon et al. (2015) for the ossicles (1918, 1855 and 1565 kg/m^3 for the malleus, incus and stapes, respectively). Based on Maftoon et al. (2015), we assumed the Rayleigh damping parameter β to be 2×10^{-6} s for the manubrium and the pedicle and adjusted β for the wedge to be 2×10^{-4} s by matching our model's frequency response at the umbo to that of Maftoon et al.

For the FEBio model, the manubrium and wedge were modelled as viscoelastic. The same Young's modulus and Poisson's ratio were used as in the Code_Aster model. The relaxation coefficients were again set to 0.07 except that at time constant 2.3 s the coefficient was adjusted to 13.0 to match the magnitude of the resonance frequency of our model to that of the model of Maftoon et al. Although this

adjustment violates constraints on the Prony-series coefficients discussed in section 3.3.2.3 (Viscoelasticity), it can be thought of as following the common practice of representing the cochlea by a first-order mass-spring-dashpot system. The damping coefficient is set to be higher than 1 for an overdamped system (Choukir, 2017, p. 72).

4.4.3 Incudostapedial joint

Considering the simple geometry being used for the ISJ, we decided to model the structure as a simple cartilage layer. In the Code_Aster model, the ISJ was considered to be isotropic elastic (E=0.3 MPa and ν=0.49). The Young's modulus was adjusted to be slightly higher than the value of 0.27 MPa used in Maftoon et al. (2015) because our ISJ structure had a smaller cross-sectional area and was thinner. In the FEBio model, we considered the ISJ to be viscoelastic and used the material properties of the cartilage layers in the human ISJ model of Soleimani et al. (2020). For the elastic part, we used an isotropic linear-elastic material with the same Young's modulus and Poisson's ratio as were used for the cartilage by Funnell et al. (2005) and by Soleimani et al. (2020), E_c=10 MPa and ν_c=0.3. For the viscous part, as suggested by Soleimani et al. (2020), a two-term Prony series was used with time constants τ_1=1.5 s and τ_2=35 s, and coefficients g_1=0.8 and g_2=0.5, respectively.

4.4.4 Stapes and cochlear load

Since the stapes is assumed to be rigid in both the Code_Aster model and the FEBio model, we use a simple block structure to represent it and to provide points of connection for the representations of the annular ligament and cochlear load. The stapes is modelled as isotropic elastic and is given material properties similar to those of the manubrium, wedge and pedicle. We used a Young's modulus of 16.0 GPa and a Poisson's ratio of 0.3. The damping coefficient was adjusted to different values in the Code_Aster model and the FEBio model. Here, we report the values we used in the two models separately.

The cochlear load is said to approximate a pure viscous damping for frequencies under 30 kHz (e.g., de La Rochefoucauld et al., 2008; Ravicz et al., 2008). The average magnitude of the cochlear damping was estimated to be 15.4×10^{-3} Ns/m^3 with a stapes footplate area of 0.62 mm^2 for gerbil in de La Rochefoucauld et al. (2008). In the model of Maftoon et al., each of the four dashpots had a damping coefficient of 3.85×10^{-3} Ns/m^3. After comparing the linear low-frequency model response at the umbo to the response of the model of Maftoon et al., we adjusted the damping coefficient per dashpot to 6.3×10^{-3} Ns/m^3 in the Code_Aster model.

The cochlear load in the FEBio model is also implemented using four dashpots connected perpendicularly to the footplate. In FEBio the dashpots must be connected via rigid-body interfaces, and the other ends of the dashpots are connected to rigid bodies fixed in space; since the rigid connectors are configured not to have bending stiffness, the <*check_zero_diagonal*> flag must be set to 0 (false) to avoid simulation errors. We adjusted the damping coefficients to 6.0×10^{-3} Ns/m^3 by matching our model's linear response at the umbo to that of the model of Maftoon et al.

4.5 Loading conditions and time-step analysis

For the acoustic stimulus, the choice of the time step is crucial and is determined by the highest frequencies of interest. To study the effects of time-step sizes on the responses, we performed simulations with time steps of 50, 30, 15, 10 and 5 μs. Fig. 4-7 shows the effect of the time step on the umbo frequency response. Below a time step of 30 μs, we observe a negligible increase (less than 0.1 nm/Pa) in magnitude at low frequencies as the time step became finer. Above 6 kHz, we observed a dramatic difference in the frequency roll-offs for a time step of 30 μs and 50 μs. We chose a time step of 10 μs for our simulations, in an endeavour to balance the trade-off between accuracy and computation time.

We examined the model response to different loading conditions. To evaluate the material properties, we applied a unit-step sound pressure of 1 Pa on the TM surface and performed transient FE analysis. Simulations were performed with a time step of 10 μs and were continued for 75 ms following the onset of the unit-step sound-pressure input. By the end of 75 ms, the velocity magnitude at different locations on the TM and footplate had reached almost zero. Increasing the time span of the simulation from 75 ms to 100 ms changed the response by less than 0.03 dB, so the time span of 75 ms was used to save computation time. Frequency responses were obtained by computing the fast Fourier transforms of the velocities at different locations. For results obtained from simulations run with the linear solver in Code_Aster, displacement responses were differentiated to get velocities. For simulations computed in FEBio, the velocity results were directly exported and used in the frequency response analysis. The selected time span provided a frequency resolution of 12 Hz. The response of our model was compared with those of the models of Maftoon et al. (2015) and Choukir (2017).

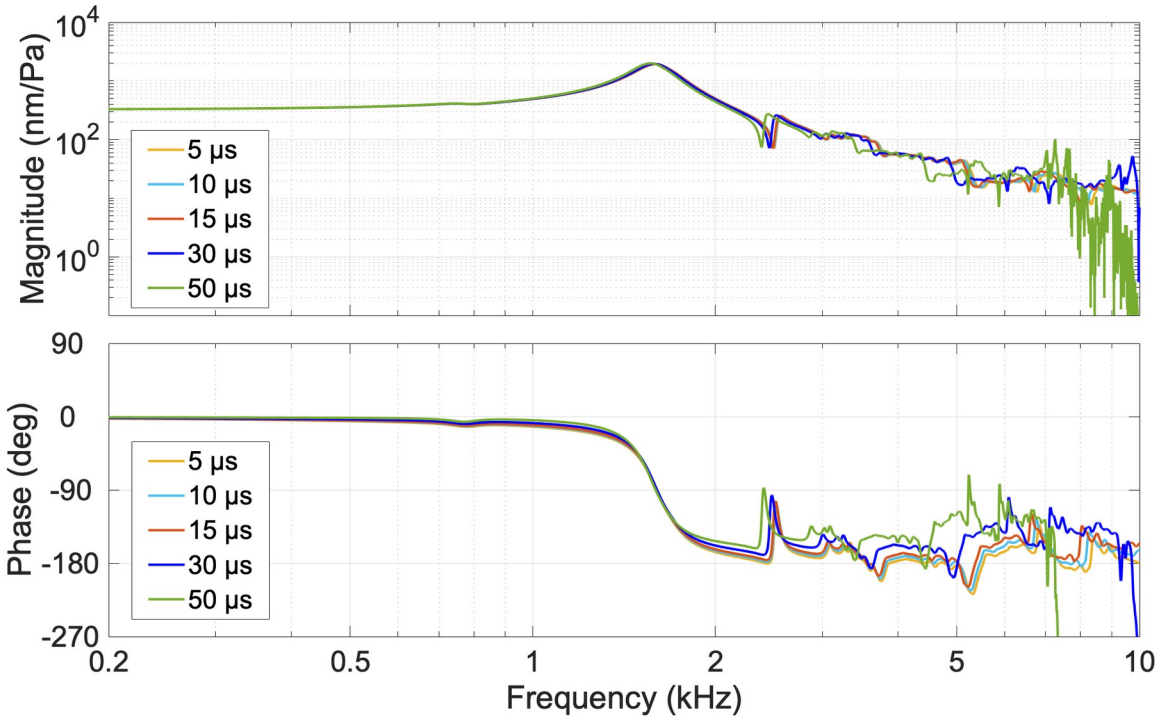

Figure 4-7: Effect of size of time step on simulated umbo frequency response.

We also evaluated the response of our middle-ear model to quasi-static triangular pressure inputs changing at linear rates between 200 Pa/s and 1.5 kPa/s with the amplitude varying between ±2.5 kPa as done by Dirckx et al. (2006) and with the amplitude varying between ±2.0 kPa as done by Dirckx and Decraemer (2001). To obtain stable results, we simulated at least 3 pressurization cycles at each pressure-change rate. To replicate the condition of tympanometry, we followed the same approach used by Choukir (2017) and added a 0.3-s sinusoidal acoustic stimulus of 1 Pa amplitude to the quasi-static triangular pressure stimulus changing at 1.5 kPa/s. The sinusoidal acoustic stimuli were added onto both the ascending (from −2.5 kPa to +2.5 kPa) and descending (from +2.5 kPa to −2.5 kPa) branches, near the 0-Pa pressure as presented in Fig. 4-8. We plotted vibration displacement versus pressure for periods where the acoustic stimuli were applied to study how the peak pressure changes between the two branches as a function of the pressure-change rate.

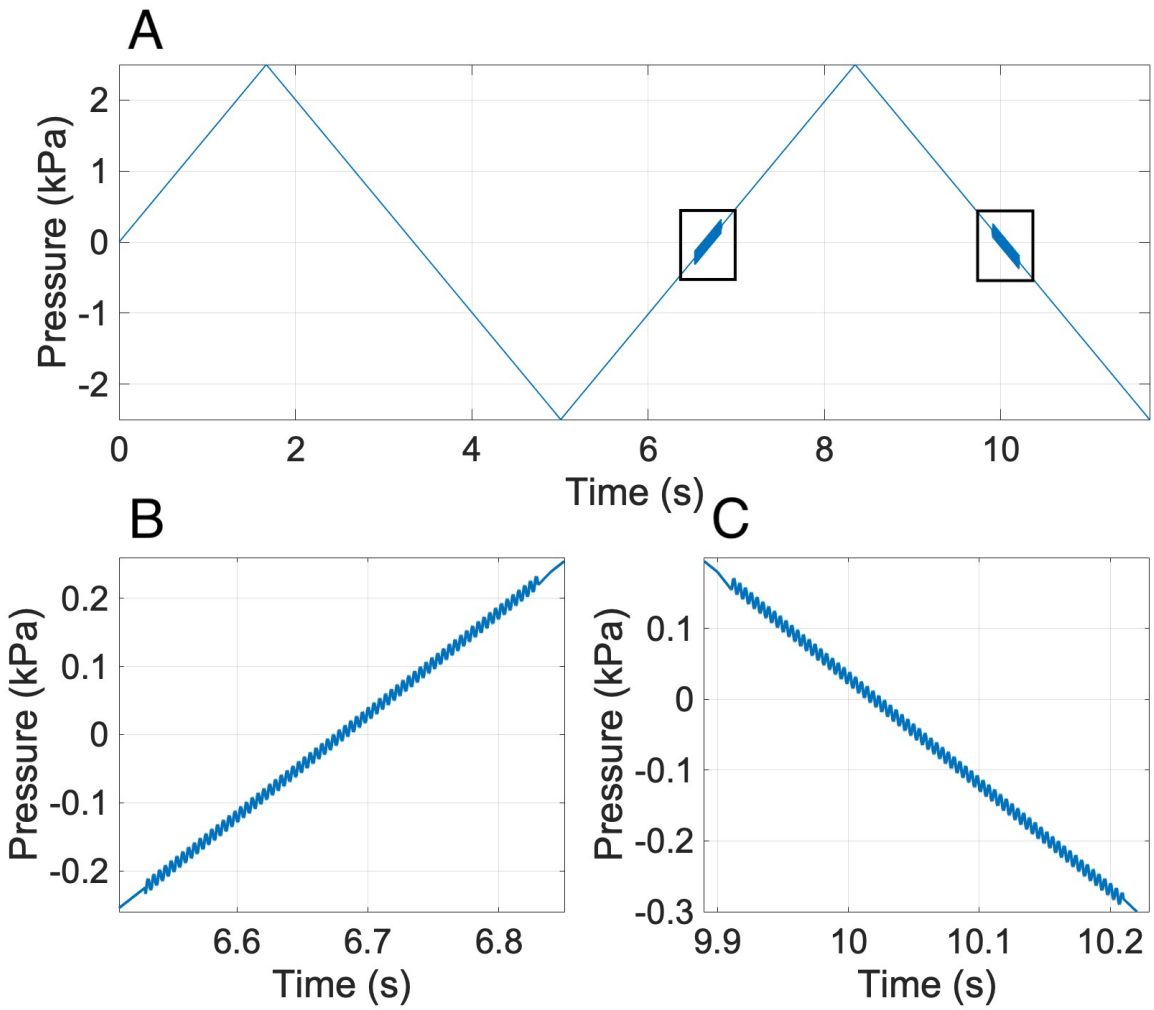

Figure 4-8: Illustration of the loading condition for quasi-static pressure changing at 1.5 kPa/s with a superimposed pure tone of 226 Hz. A: Pressure as a function of time with a magnification of the acoustic stimulus (a factor of 100 was applied to the acoustic stimulus for better visualization). B: A closer view of the left-hand rectangle in A. C: A closer view of the right-hand rectangle in A. For panel B and C, a factor of 10 was applied to the acoustic stimulus for better visualization.

This loading condition of quasi-static pressure plus acoustic stimulation requires lengthy simulation times. Therefore, multiple steps are used in FEBio to shorten the run time. When only the quasi-static pressure is applied, we specified a constant time step of 10 ms. We had to set the parameter for the maximum number of updates (i.e., <*max_ups*>) in FEBio to 50 for the solver to converge during the transients. When an acoustic stimulus is applied in addition to the quasi-static pressure, a constant time step of 10 μs was employed.

We also studied the response of the middle ear to a sudden increase in static pressure (mathematically represented by a fast ramp function) followed by an acoustic signal. The input pressure was increased linearly from 0 to 250 Pa in 10 ms and maintained at 250 Pa for the rest of the input. At 25 ms, an acoustic pressure of 2 Pa peak to peak was introduced as a sinusoidal wave at 226 Hz for 50 ms, or as a chirp with frequency changing linearly from 0.12 to 3 kHz for 128 ms. This loading condition was intended to evaluate the ability of the model to simulate conditions present in step-wise pressurization cycles in LDV experiments in our lab (e.g., Kose et al., 2020). For these loading conditions, we used a uniform step size of 10 μs for the simulations.

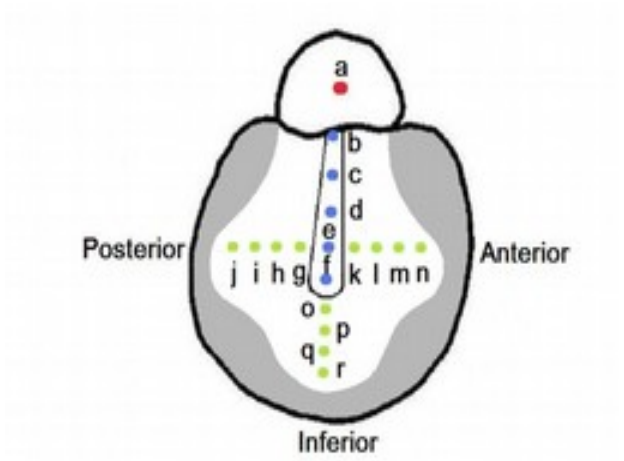

Figure 4-9: A schematic of the general layout of eighteen micro-beads on a right gerbil TM; the shaded area represents the remaining hidden region of the PT (He, 2012).

As done in Maftoon et al. (2015) and Choukir (2017), we chose to export the displacement or velocity values for only a limited set of nodes corresponding to where LDV measurements were made by Maftoon et al. (2014) and Kose et al. (2020). We considered only two nodes on the manubrium (d and e in Fig. 4-9), a node on the posterior PT (g), a node on the anterior PT (k) and a node at the centre of the PF (a).

Chapter 5: Results

5.1 Introduction

In this chapter, we present the responses of our FE model of the gerbil middle ear to the different loading conditions described in the previous chapter. In section 5.2, we report the model response to low-amplitude sound stimuli and compare results from the two FE solvers with those from the model of Maftoon et al. (2015). In the subsequent sections, results are presented for the non-linear regime based on the FEBio model. In section 5.3, we present the model response to high quasi-static pressures in the form of triangular waves as well as a combination of high quasi-static pressure with a low-amplitude, low-frequency (226-Hz) pure tone. Simulation results are compared with those obtained from the model of Choukir (2017) and with experimental measurements. In section 5.4, we report the model response to a large pressure step followed by low-amplitude sound pressures, including a low-frequency pure tone and a chirp. The chirp results are compared with experimental measurements made by Kose et al. (2020).

5.2 Unpressurized vibrations

In this section, we first present and compare the low-amplitude responses of our model with two different solvers (Code_Aster and FEBio). Then, we present the frequency responses of our FEBio model at the umbo and at two nodes on the manubrium, two nodes on the PT and one node on the PF (as discussed in section 4.5) and compare them with the responses of the model of Maftoon et al. (2015) and previous experimental results.

5.2.1 Comparison of FEBio and Code_Aster models

As mentioned in section 4.2, we ran linear (low-amplitude) simulations with the same model geometry using two different linear FE solvers, for model verification. In the Code_Aster model, the TM was

linear elastic. In the FEBio model the TM material was hyperviscoelastic but with an effective low-amplitude Young's modulus that was the same as the Young's modulus in the Code_Aster model. The different damping representations in the two solvers were adjusted to produce very similar displacement magnitudes at the main system resonance. This step was done to confirm that FEBio and Code_Aster would provide the same results at low amplitudes and low frequencies, and that they could provide similar results at higher frequencies, to increase our confidence in the FEBio results.

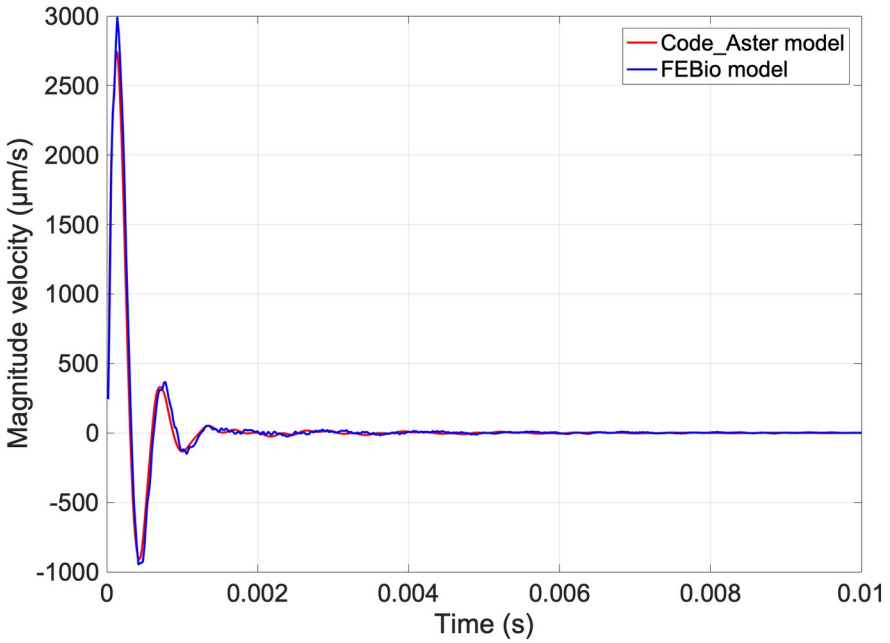

Figure 5-1: Comparison of time-domain umbo velocities in FEBio and Code_Aster.

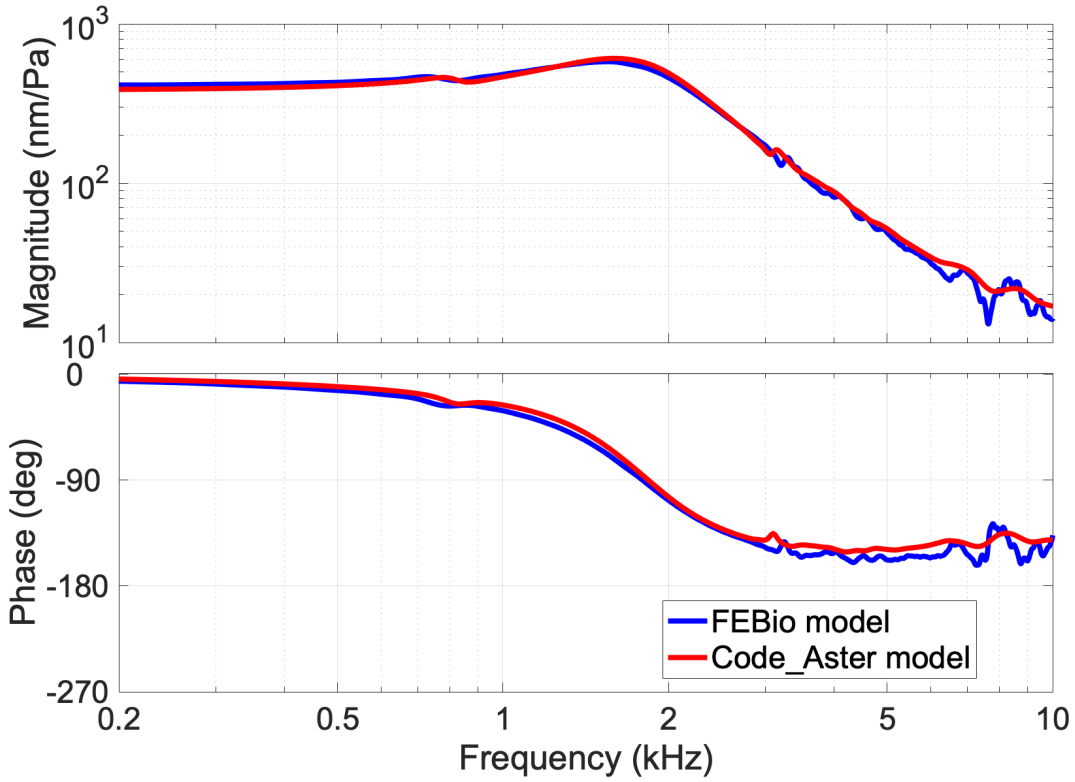

Figure 5-2: Comparison of umbo displacement frequency responses in FEBio and Code_Aster.

Fig. 5-1 shows the *z* component (i.e., perpendicular to the plane of the TM annulus) of the velocity magnitude in the time domain for the umbo in both FEBio and Code_Aster in response to a step pressure of 1 Pa. The two FE solvers produced very similar responses. Fig. 5-2 shows the corresponding displacement frequency responses, which are also very similar. The difference in magnitude of the frequency response at 0.2 kHz is 24 nm/Pa. For frequencies between 0.2 and 2 kHz, the difference in magnitude is less than 10 nm/Pa.

5.2.2 Umbo and pars-flaccida responses

Some of the material properties of the components of our model were estimated based on matching the umbo response to that of the model of Maftoon et al. (2015). In earlier experimental studies (e.g.,

Lee and Rosowski, 2001; Rosowski and Lee, 2002; Maftoon et al., 2014), it was observed that the PF affects responses measured at the umbo. Here we present the umbo and PF responses together.

5.2.2.1 Low frequencies

Fig. 5-3 shows our model frequency response from 0.2 kHz to 10 kHz in comparison with that from the model of Maftoon et al. The magnitude and phase of the umbo at the lowest frequency in our model were 384.4 nm/Pa and –3.8°, compared with 382.2 nm/Pa and –3.3° for the model of Maftoon et al., resulting in a difference of 1.6% for the magnitude and a difference of 15% for the phase.

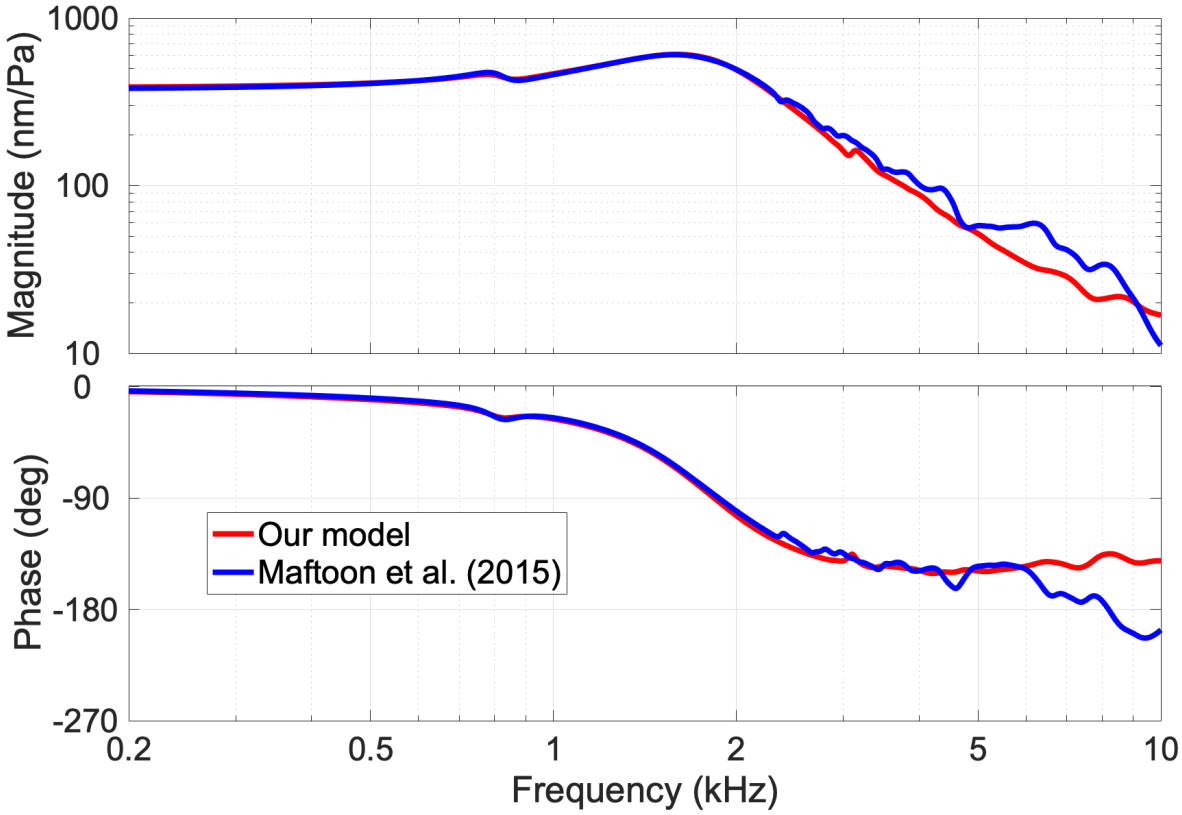

Figure 5-3: Comparison of our model's umbo response with that of the model of Maftoon et al.

Fig. 5-4 shows our model response at the centre of the PF in comparison with that from the model of Maftoon et al. The magnitude of the simulated response at the centre of the PF at resonance (820 Hz) is 9.6 μm/Pa, which is 36% lower than the 15 μm/Pa magnitude from the model of Maftoon et al.

Although the PF material density and Young's modulus are predefined to match the width and frequency of our model's PF resonance to those of the model of Maftoon et al., our PF response is lower in magnitude. This is attributed to differences in the material density and boundary conditions for the PF in the two models. The PF is simply supported in the model of Maftoon et al. but is fully clamped in our model.

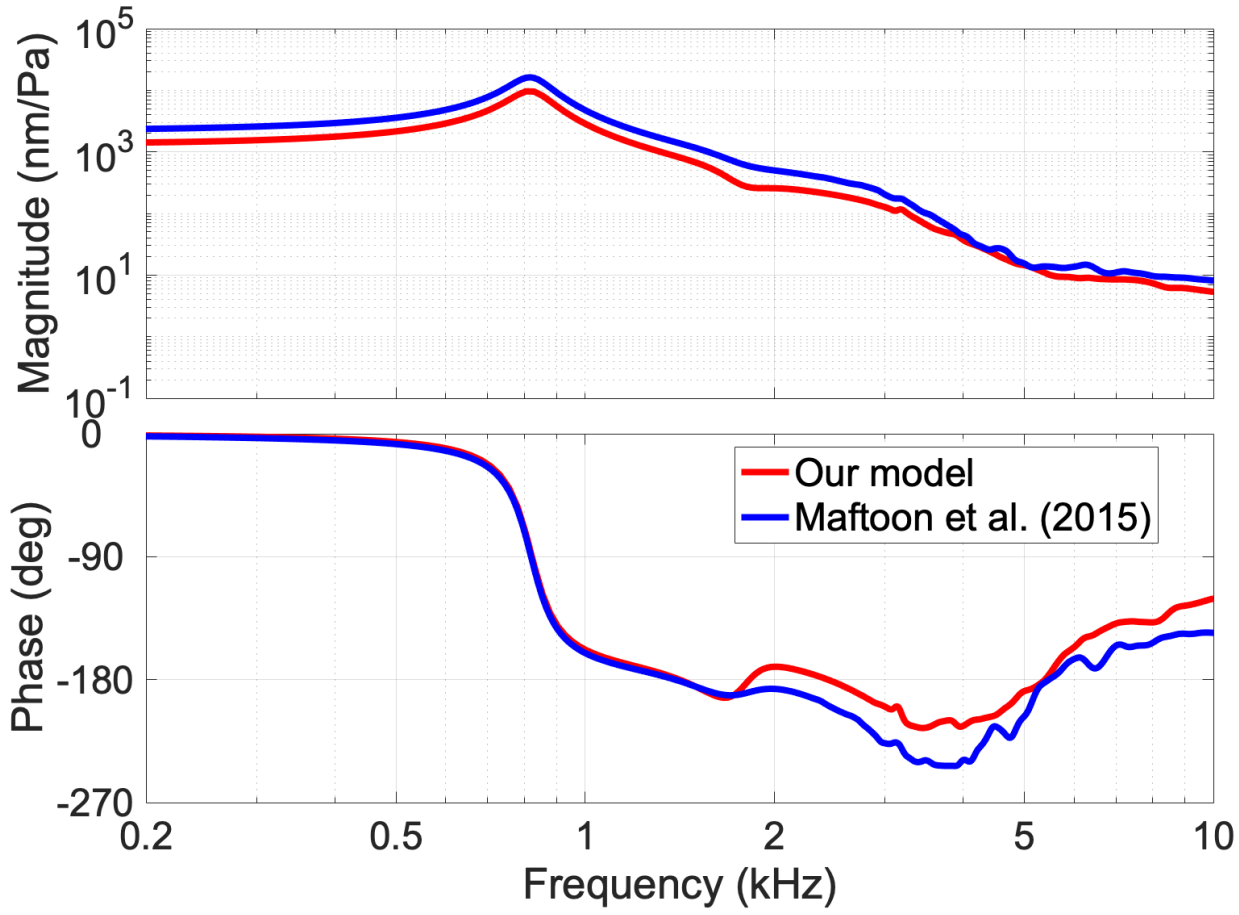

Figure 5-4: Comparison of our model's PF response with that of the model of Maftoon et al.

Fig. 5-5 shows a magnified view of the umbo response from 0.2 to 2 kHz, presenting the PF-related feature more clearly. The umbo response exhibits a feature that includes a shallow magnitude maximum (790 Hz) followed by a shallow minimum (890 Hz), and a local minimum in the phase (830 Hz). By comparison, in the model of Maftoon et al. the feature is located at a similar frequency, with a

shallow magnitude maximum at 780 Hz followed by a shallow minimum at 880 Hz, and a local minimum in the phase at 820 Hz. As discussed in section 5.2.4, this feature in the umbo response corresponds to the resonance in the PF response when the PF is flat. The PF shows a resonance around 820 Hz in both our model and that of Maftoon et al., corresponding to the frequency of the local minimum in the umbo response. This feature is more pronounced in the model of Maftoon et al. than in our model, due partly to our PF resonance having a lower magnitude, and partly to the coupling between the PF, PT and manubrium, which we will discuss in section 5.2.4 (PT response).

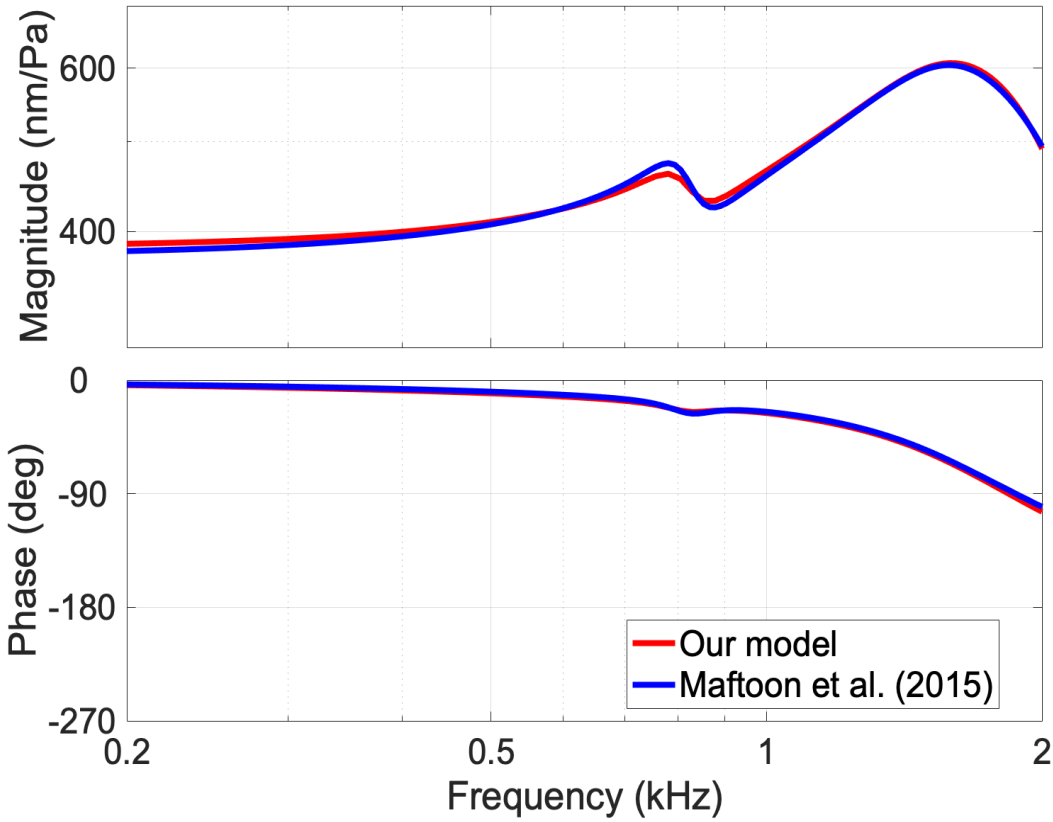

Figure 5-5: A magnified view of part of Fig. 5-3 (model umbo response) to show the effect of a flat PF on the umbo response. A local maximum followed by a local minimum can be seen in the displacement magnitude, corresponding to the resonance of the PF response in Fig. 5-4.

5.2.2.2 Mid and high frequencies

The simulated umbo response (Fig. 5-3) shows a rather broad resonance with a peak magnitude of 604 nm/Pa at 1.6 Hz, very similar to what was obtained with the model of Maftoon et al., which also has a peak magnitude of 604 nm/Pa at 1.6 Hz. The width and magnitude of the resonance are mainly controlled by the Rayleigh damping parameters and the cochlear load; the frequency of the resonance is mainly controlled by the material properties of the PT, including its material density and elastic parameters. The material properties of the PT and the Rayleigh damping parameters were adapted from the model of Choukir, and the damping coefficient at the footplate was selected to match the model of Maftoon et al.

For frequencies above the resonance frequency, the umbo response of our model (Fig. 5-3) starts to show differences from that of the model of Maftoon et al. Our model also appears to be more heavily damped than that model, having fewer irregularities above 2 kHz. To match the umbo resonance magnitude, we adjusted the cochlear damping to be 6.3×10^{3} Ns/m per dashpot, which is higher than the coefficient of 3.85×10^{3} Ns/m used in the model of Maftoon et al. The phase responses deviate substantially above 6 kHz. The differences between the two models at higher frequencies can be attributed to the assumptions we made in our model. At higher frequencies, the vibrations of the ossicles become more complex and the ossicles no longer rotate around a fixed axis of rotation, as observed by Maftoon et al. (2015). Since our model assumes a fixed axis of rotation and does not include all the anatomical details of the ossicles, it is to be expected that the response of our model at high frequencies deviates from that of the model of Maftoon et al. For the PF, apart from the shift in the magnitude, the shape and features are similar in the two models up to about 1.6 kHz.

As mentioned above, the amount of cochlear damping significantly affects the magnitude of the resonance. In Fig. 5-6, we compared the umbo responses of our Code_Aster model to the model of

Maftoon et al. with cochlear damping (solid lines, as in Fig. 5-3) and without cochlear damping (dashed lines). Both models used Rayleigh damping for the TM and cochlear damping at the footplate. The resonance magnitude of our Code_Aster model without cochlear damping is higher than that of the model of Maftoon et al. without cochlear damping, although the curves with cochlear damping are very similar. In our FEBio non-linear model, we used a Prony series instead of Rayleigh damping to represent damping in the viscoelastic components and implemented dashpots at the stapes footplate to model the cochlear load. In Fig. 5-7, we compare the umbo responses of our models in the two different solvers with and without cochlear damping. From the curves without cochlear damping, it is clear that the damping provided by the Prony series in the FEBio model is less than that provided by the mass-proportional Rayleigh damping. Prony series can be used to adjust damping separately in different frequency ranges, while Rayleigh damping affects all frequencies with a single parameter. Due to the lack of knowledge about both the TM damping and the cochlear impedance in gerbils, it is not clear to us whether the TM damping or the cochlear damping plays a more dominant role in middle-ear sound transmission. In any case, for our subsequent analyses we only look at responses below 3 kHz, where the effect of damping (except for the cochlear load) is relatively small.

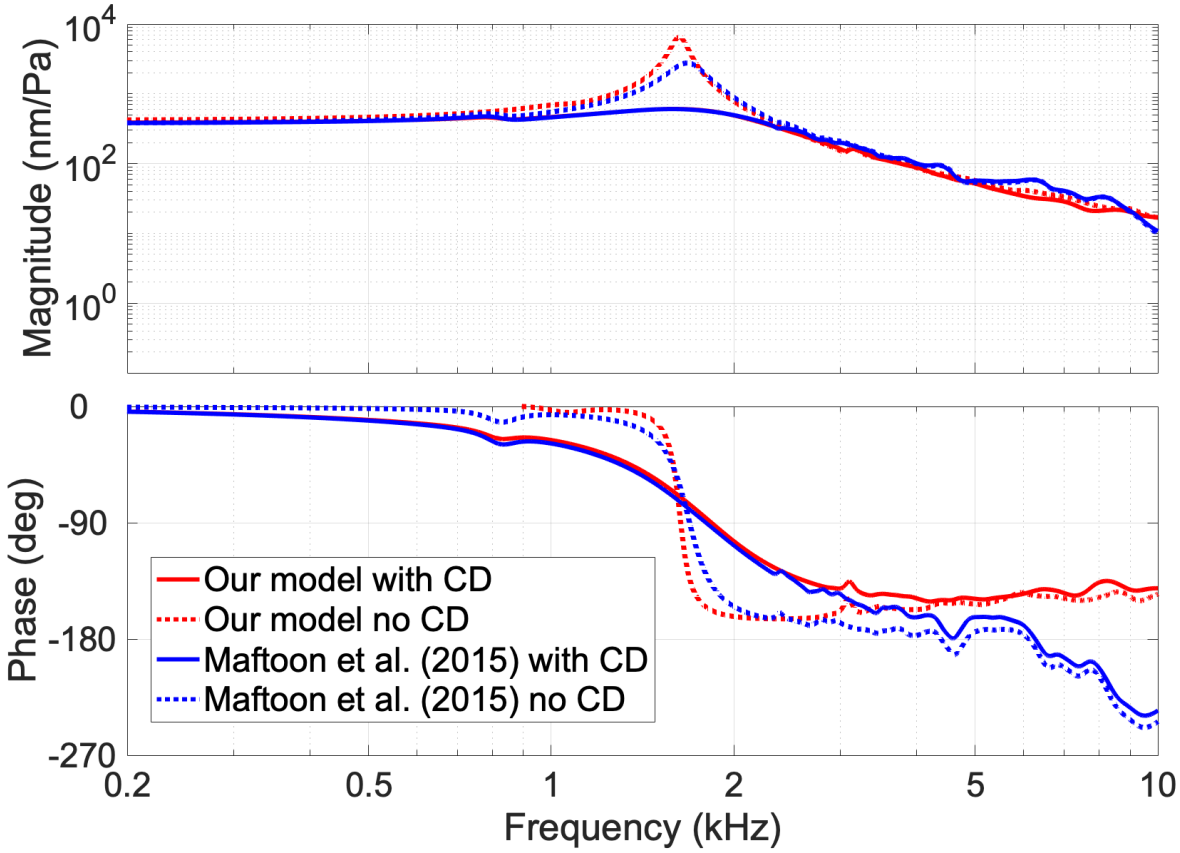

Figure 5-6: Comparison of umbo responses of our Code_Aster model and the model of Maftoon et al., with and without cochlear damping (CD).

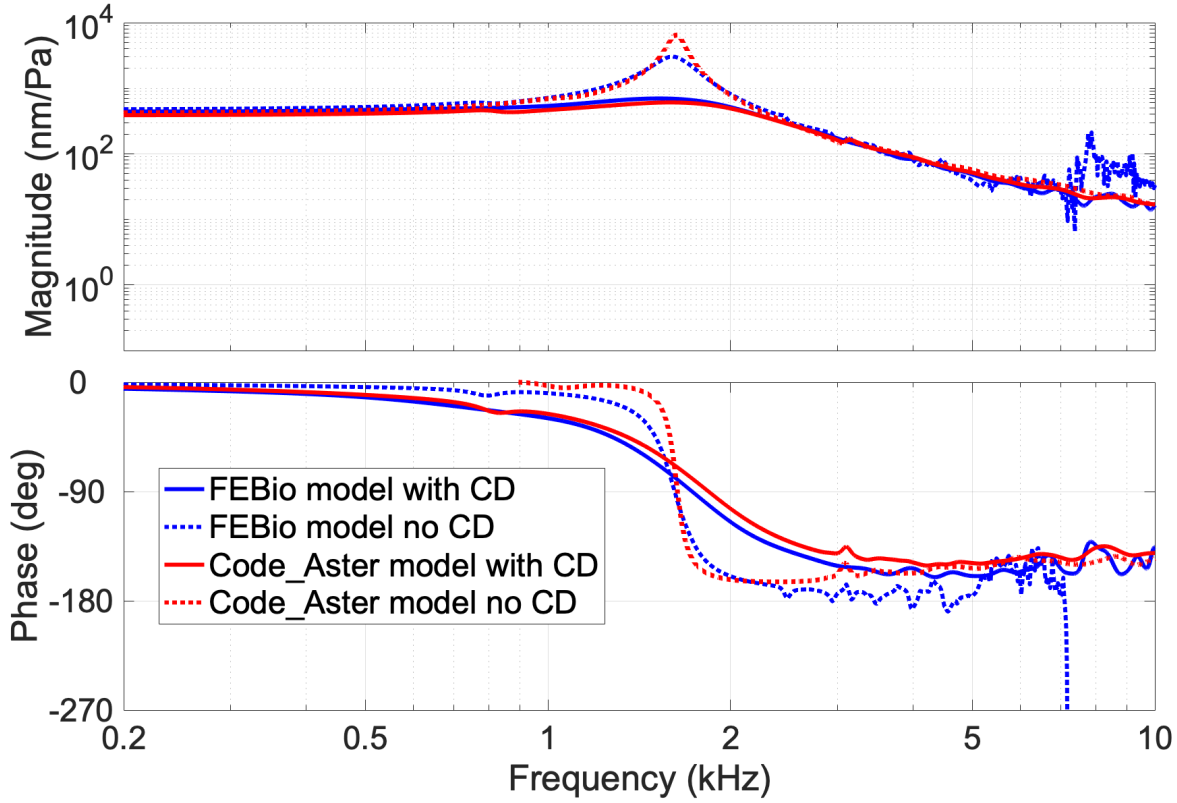

Figure 5-7: Comparison of our models in FEBio and Code_Aster with and without cochlear damping (CD).

5.2.3 Manubrial response

Fig. 5-8 shows the responses for our model at three points along the manubrium. Similar to the experimental observations by Maftoon et al. (2014) and to the behaviour of the model of Maftoon et al., the magnitude increases towards the umbo (from purple to maroon to yellow), and all points along the manubrium move almost exactly in phase with each other up to very high frequencies. This pattern in the responses is consistent with the fact that, in our model, the malleus is assumed to rotate around a fixed axis of rotation. Thus, the displacement along the manubrium is proportional to the distance from the axis of rotation.

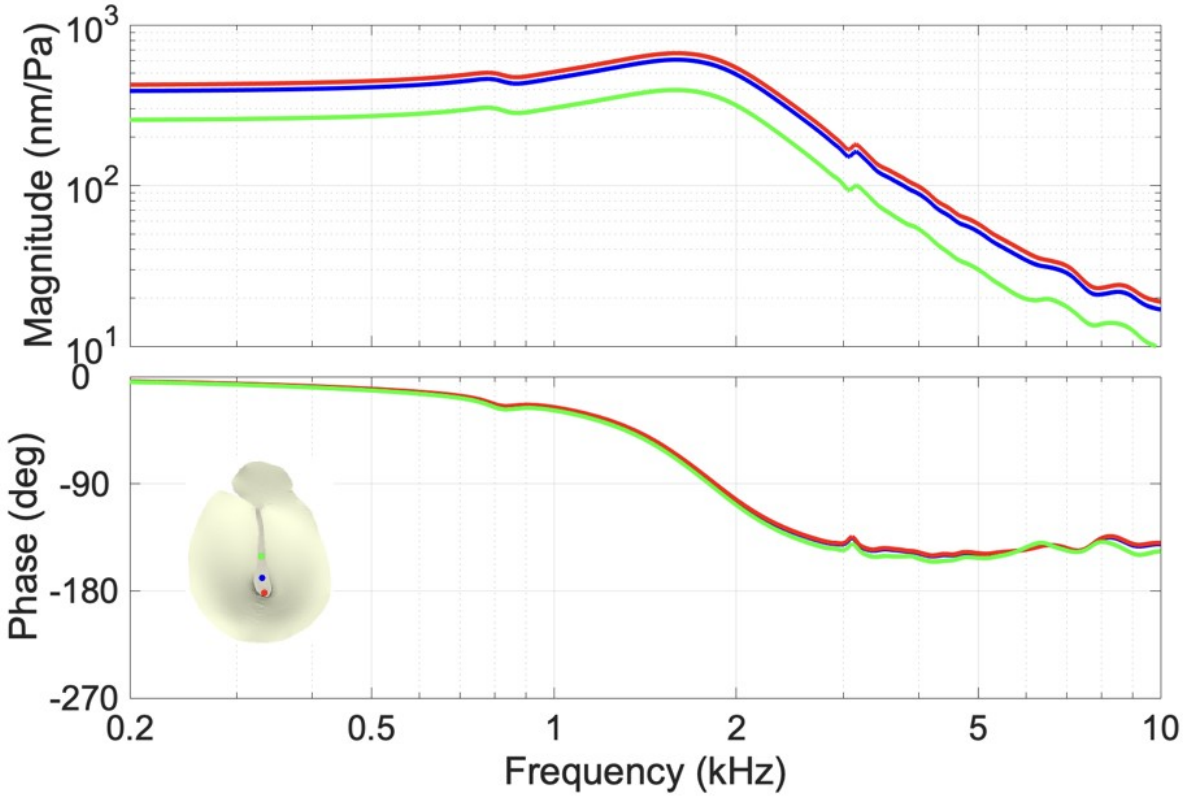

Figure 5-8: Model displacement responses at three locations along the manubrium.

Fig. 5-9 shows the responses of our model at the umbo and also mid-manubrium, compared with those from the model of Maftoon et al. The displacements at corresponding points are almost the same for the two models up to around 2 kHz. Maftoon et al. (2015) measured the location of their axis of rotation for different frequencies. They found that at frequencies between 200 Hz and 1.5 kHz (i.e., the resonance peak), the manubrium rotates as a rigid body around a fixed axis of rotation whose location is close to that of the anatomical axis defined to run from the anterior mallear process to the posterior incudal process, as assumed in our model (see section 4.2). Above 2 kHz, the position of the axis of rotation in the model of Maftoon et al. started to shift. This does not happen in our model because we assumed a fixed axis of rotation that is independent of frequency.

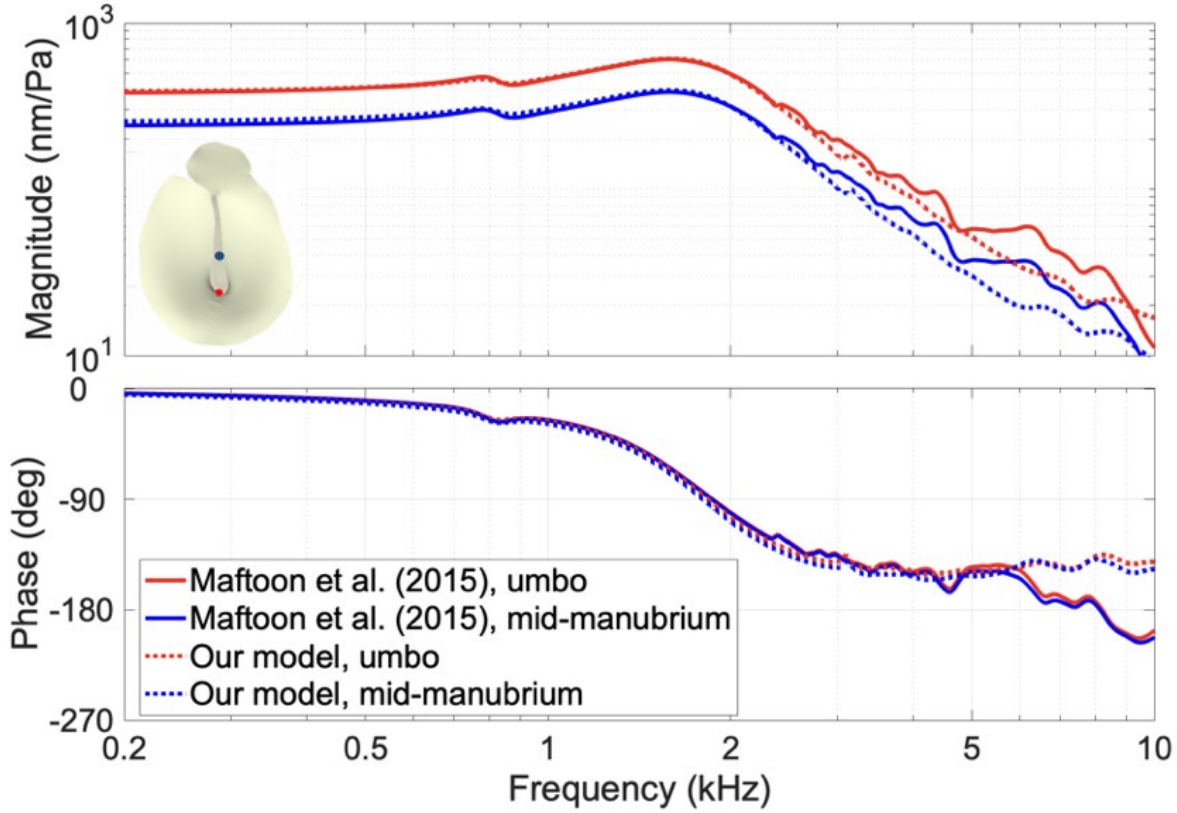

Figure 5-9: Comparison of our model response with that of Maftoon et al. at umbo and at mid-manubrium.

5.2.4 Pars-tensa response

Fig. 5-10 shows our model responses for two PT points, anterior and posterior at the level of the middle of the manubrium, and compares them to responses from the model of Maftoon et al. The two points vibrate in phase with each other for frequencies up to about 2 kHz in both models. At these frequencies, the PT points exhibit a simple motion pattern. The PT responses also show the same PF feature as seen at the umbo, but it is smaller. As observed in gerbil ears experimentally, in both models the point on the posterior side shows larger displacements than the one on the anterior side. The responses of our model at low frequencies are very similar to those of the model of Maftoon et al., and the magnitudes are within the range seen in the experimental responses (Maftoon et al., 2014). For frequencies above 2

kHz, our model responses are somewhat lower in magnitude than those of the model of Maftoon et al. because the PT in our model is stiffer than the one in the other model, as discussed in section 4.5.

The resonance has a similar shape in both models. The simple in-phase motion breaks up at higher frequencies, with each point showing different frequency-dependent magnitudes and phases. As done by Maftoon et al. (2013), we define the break-up frequency as the frequency at which the phase divergence of the points on the PT is more than 15°. The break-up frequency for the PT points in our model is 2.3 kHz. This is slightly higher than the 2.2 kHz seen in the model of Maftoon et al. (consistent with the higher stiffness of our PT) but is well within the range of 1.8 to 2.8 kHz observed experimentally (Maftoon et al., 2014).

Fig. 5-5 (and, to a lesser extent, Figs. 5-3 and 5-10) indicate that the shunting of low frequencies by the PF in our model and its effect on umbo and PT is less than in the model of Maftoon et al. As shown in experimental studies, this effect of the PF is strongly affected by the size of the middle-ear cavity (e.g., Rosowski et al., 1999; Maftoon et al., 2014). Smaller cavity sizes result in a stronger effect of the PF on the response of the umbo and PT. Thus, with an open middle-ear cavity, the PF has a very small effect on the motion of the PT and umbo, as seen in our model and in the model of Maftoon et al. In the open-cavity configuration, the effect may be modulated by the coupling of the PF with the manubrium and PT. The PT thickness in Maftoon's model was variable, but in our model it had a constant thickness of 15.8 μm, and this thickness along with the material properties used resulted in a stiffer PT in our model. This could affect the coupling between PT and PF, making the effect of the PF on the PT smaller. Furthermore, the coupling between manubrium and PT is affected by the position of the axis of rotation, which is different than in the model of Maftoon et al. This also might alter the effect of the PF on the umbo. This reduced shunting by the PF is also seen in Choukir's model, which has PT material properties which are very similar to those of our model. Such speculations about the coupling between

different structures of the middle ear could be verified by modelling different configurations: changing the axis of rotation, varying the PT thickness and material properties, etc.

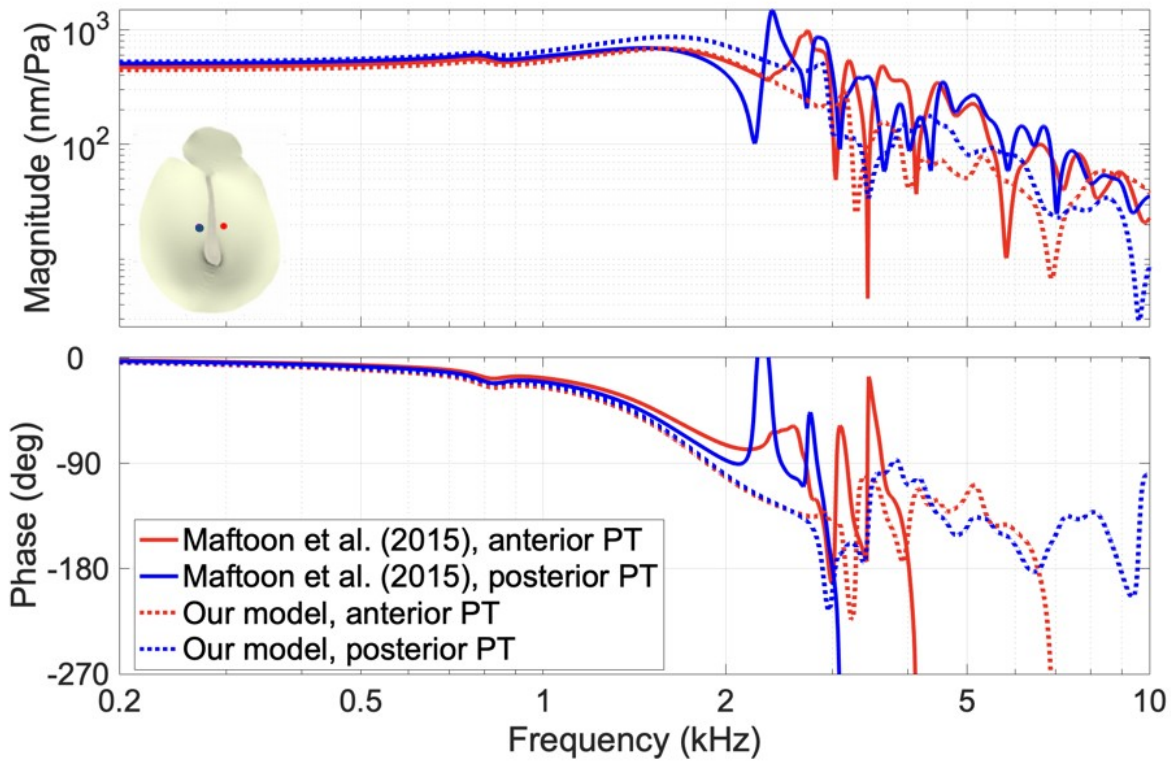

Figure 5-10: Comparison of responses of our model and that of Maftoon et al., at anterior and posterior PT points.

5.3 Pressurized vibrations

5.3.1 Triangular-wave quasi-static pressures

5.3.1.1 Displacement versus quasi-static pressure

In this section, we report the response of our model to slowly varying triangular pressure sweeps with amplitude ranging from –2500 Pa to +2500 Pa and linear pressure-change rates between 200 Pa/s and 1500 Pa/s, as was done by Choukir (2017). In addition, we also simulate the model response to triangular pressure sweeps ranging from –2500 Pa to +2500 Pa with a pressure-change rate of 1500 Pa/s and compare the resulting displacements with experimental measurements made by Dirckx and

Decraemer (2001) for pressure steps from –2000 Pa to +2000 Pa. Since small changes during preconditioning were observed in experimental studies (e.g., Dirckx and Decraemer, 2001; Dirckx et al., 2006), we only simulated 2 to 3 pressurization cycles at each pressure-change rate. Fig. 5-11A shows umbo displacement at 1500 Pa/s as a function of time for three cycles. As also found by Choukir, we can see that amplitudes at negative ear-canal pressures are always significantly larger than amplitudes at corresponding positive pressures; no significant change in the umbo displacement is seen after the first cycle, and repeated displacement-vs-pressure curves nearly coincide (Fig. 5-11B). This was also the case for low pressure-change rates. For subsequent simulations in this section, we report the displacement results of the second cycle.

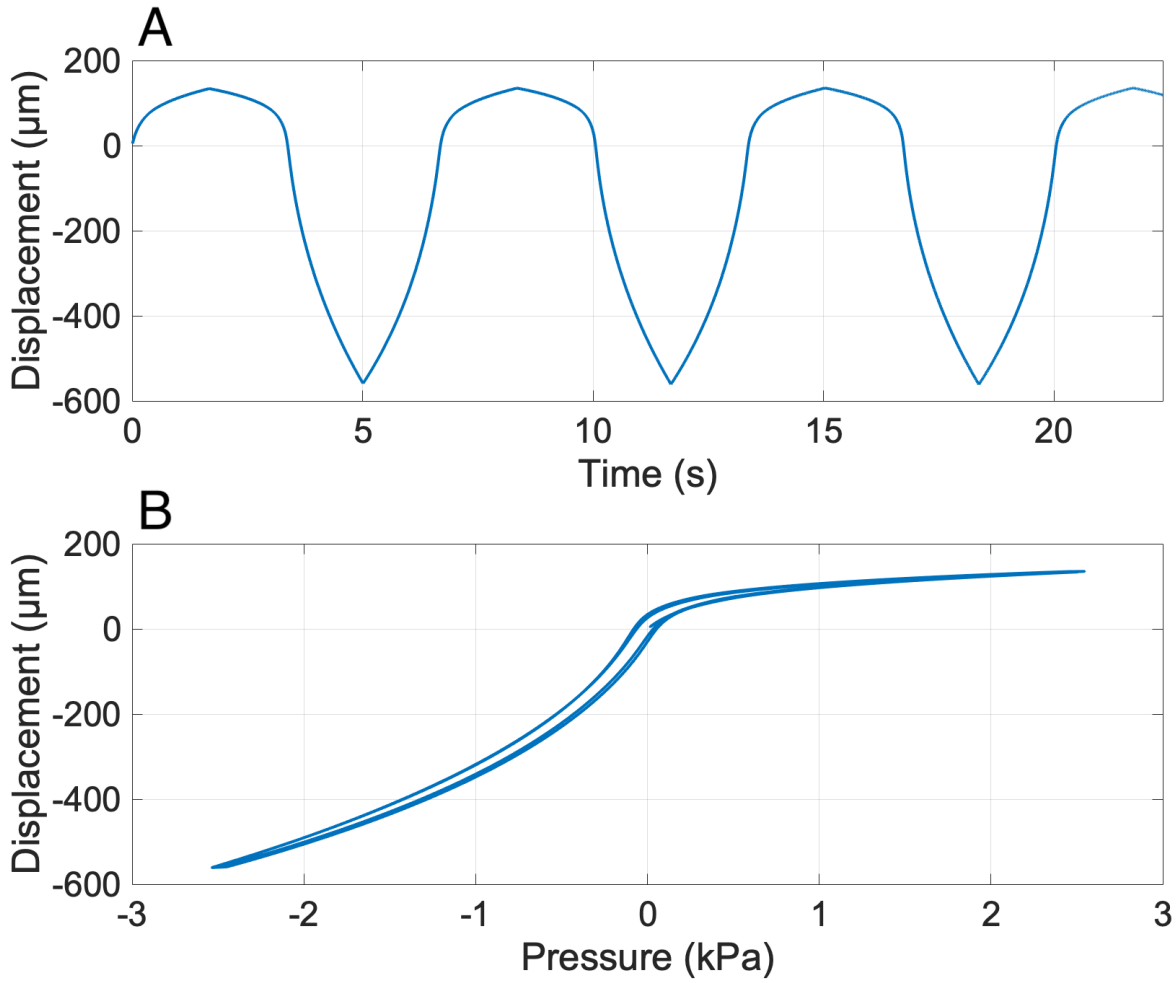

Figure 5-11: Simulated umbo response to about 4 cycles of triangular waves of pressure for a pressure-change rate of 1500 Pa/s. A: Umbo displacement as a function of time. B: Umbo displacement as a function of quasi-static pressure.

Fig. 5-12 compares the response of our model at points in the anterior and posterior PT and at the umbo to the mean deformation of the PT reported by Dirckx and Decraemer (2001). They performed a sequence of modifications of the middle ear, and stage 0 of the experimental results in Fig. 5-12B corresponds to the condition in our model. We can again observe a strong asymmetry in the vibration amplitude between positive and negative static pressures. This asymmetry is less pronounced but still present in the experimental data. We calculated the ratio of the amplitudes at +2000 and −2000 Pa. For our model, the ratio of displacement amplitudes is 2.4, while in Dirckx and Decraemer (2001) the ratio

is 1.3. Hysteresis, reflected by the difference between the loading and unloading curves, is smaller in our model response than in the experimental data.

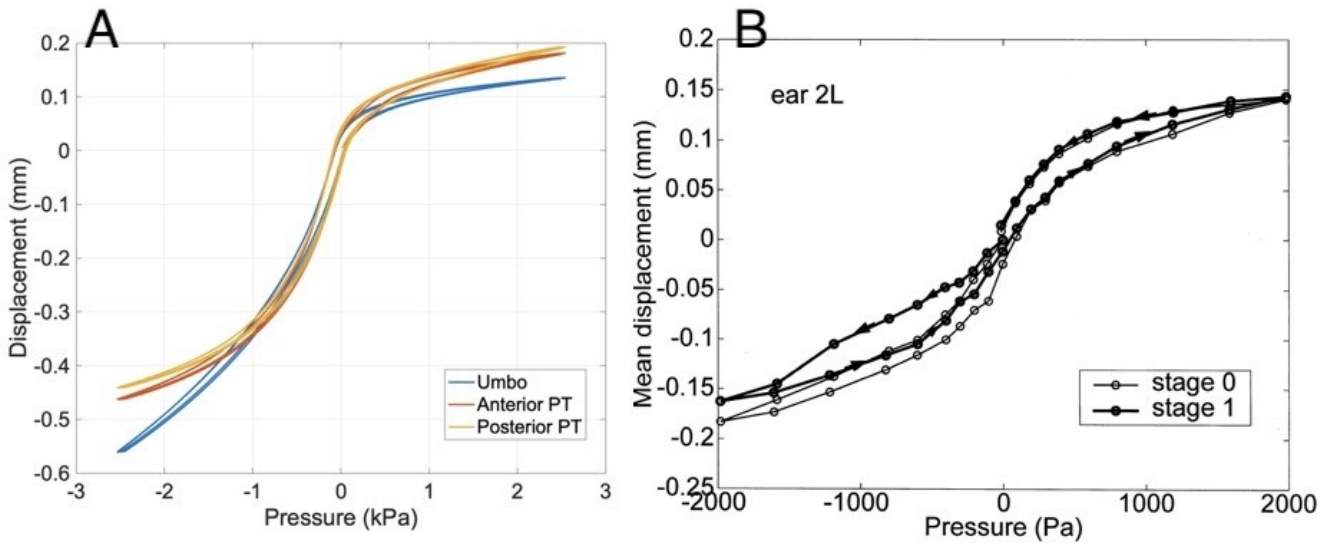

Figure 5-12: Comparison of model and experimental PT responses to quasi-static pressure. A: Response of our model for one cycle at the umbo and two points on the PT. B: Experimentally measured mean deformation as a function of pressure (Dirckx and Decraemer, 2001).

Fig. 5-13 shows our simulated umbo motion for different linear pressure-change rates ranging from 200 Pa/s to 1500 Pa/s in comparison with the response from Choukir's model and with experimental umbo motions measured by Dirck et al. (2006) for the rabbit middle ear. Our simulated umbo motion in Fig. 5-13A shows approximately the same small amount of hysteresis at all pressure-change rates. Fig. 5-13B shows less hysteresis in Choukir's results than in ours, presumably because of the absence of cochlear damping in Choukir's model for these particular simulations. The experimental data in Fig. 5-13C show more hysteresis, especially for lower pressure-change rates, than in the model responses. Compared with Choukir's simulation results, our simulation displacements are approximately 5% larger at positive ear-canal pressures and are slightly smaller at negative ear-canal pressures.

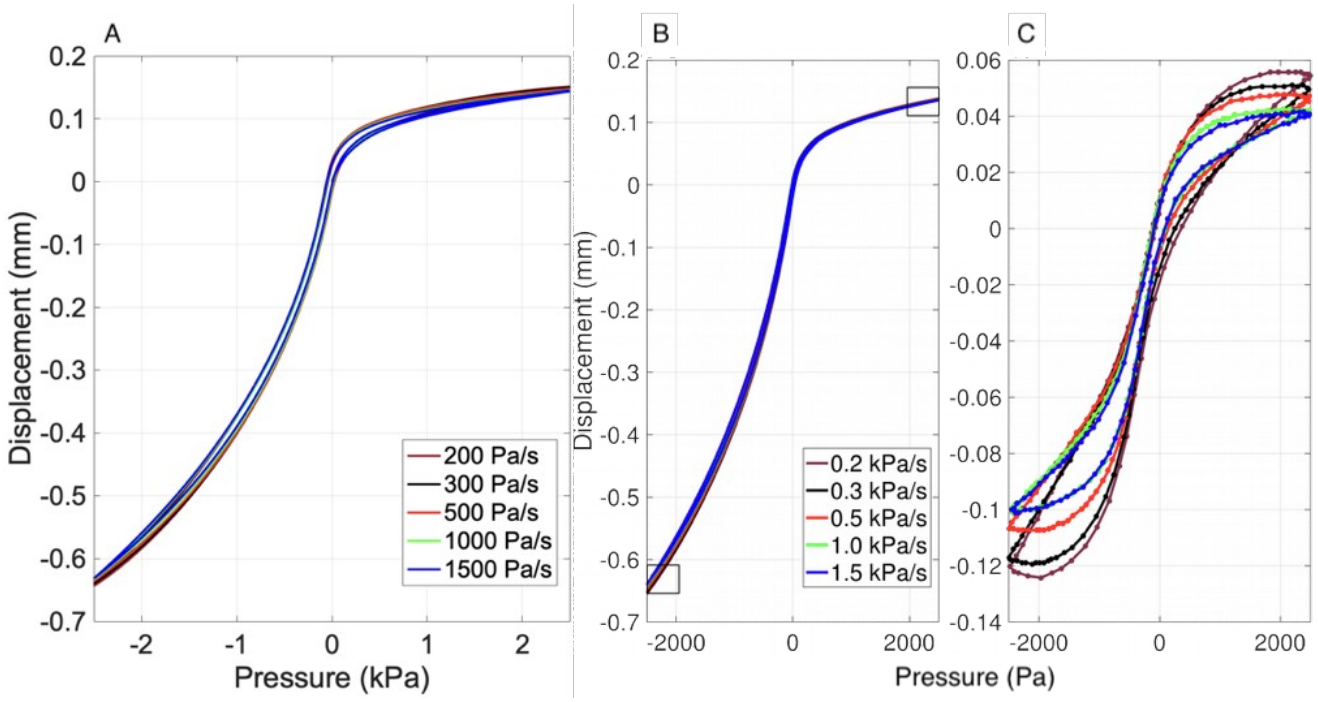

Figure 5-13: Umbo displacement vs. pressure for various pressure-change rates. A: Umbo displacement obtained with our model. B: Umbo displacement obtained with Choukir's model. C: Experimental umbo displacement obtained by Dirckx et al. (2006).

5.3.1.2 Vibration amplitude versus quasi-static pressure

To simulate tympanometry, we applied a 226-Hz pure tone with a magnitude of 1 Pa (equivalent to 94 dB SPL) for 300 ms around zero pressure on both the ascending and descending branches of the pressure sweep. We chose to apply the acoustic stimuli only for two short intervals and only on the 1500 Pa/s pressure sweep to reduce the computation time. The acoustic stimulus was applied to the ascending branch from 6.53 s to 6.83 s, to cover a range of static pressure from –225 Pa to +225 Pa. It was then applied to the descending branch from 9.91 s to 10.21 s, to cover a range of static pressure from +165 Pa to –285 Pa. Both periods include zero static pressure. Fig. 5-14 shows the umbo displacement as a function of time in response to the quasi-static pressure and sound stimulus. Fig. 5-14B and Fig. 5-14C are magnified views of the rectangles in Fig. 5-14A, showing the very small displacements resulting from the application of the pure tone.

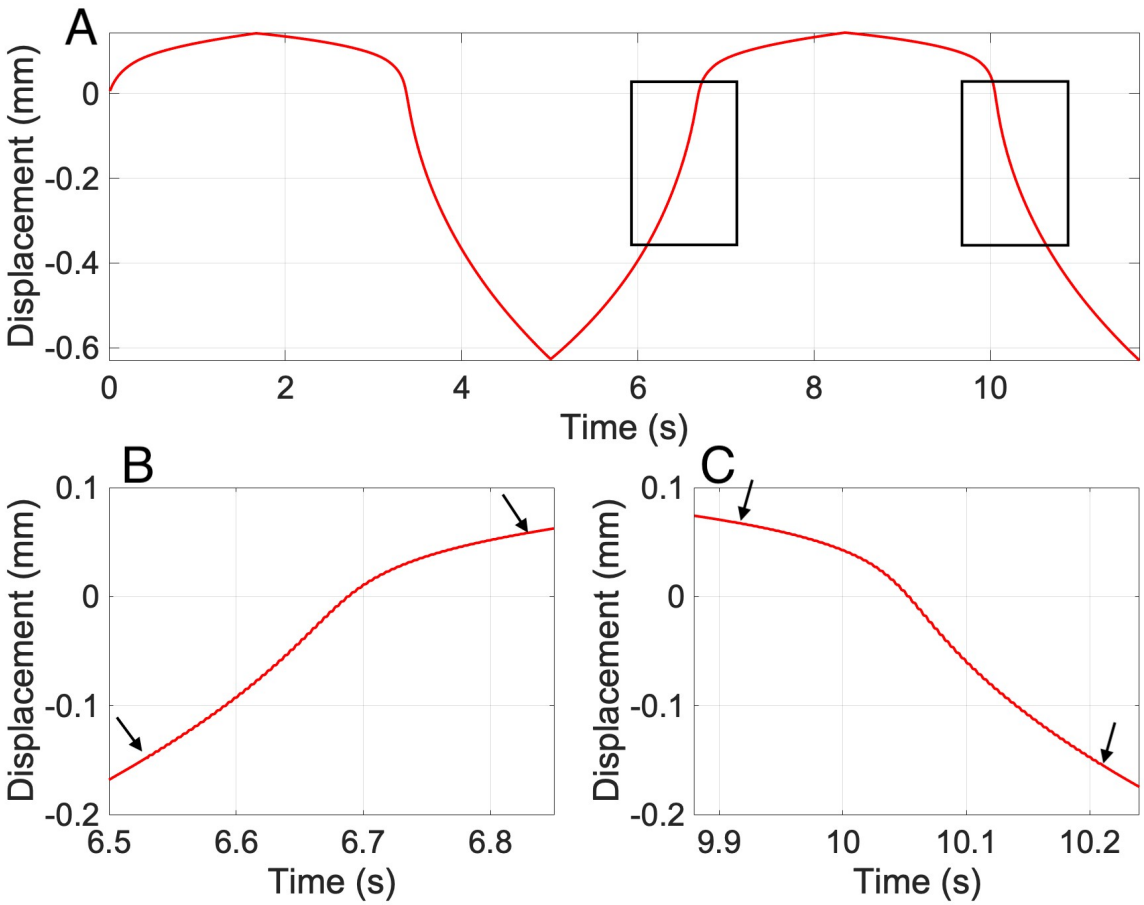

Figure 5-14: Response of our model to 226-Hz acoustic stimuli during large sweeps of quasi-static pressure. A: Umbo displacement as a function of time. Rectangles indicate areas where the acoustic stimuli were applied. B: Magnified view of the two rectangles in A to show the acoustic induced displacements during the quasi-static sweeps. Arrows indicate the start and end of the vibrations.

Fig. 5-15 shows the umbo response to the acoustic stimuli with the quasi-static response subtracted away. As seen in Fig. 5-15A for the ascending branch, as the static pressure increases, the umbo vibration increases slightly, then starting at time 6.68 s, which corresponds to a quasi-static pressure of –28.8 Pa, the vibration decreases. For the descending branch (Fig. 5-15B), as the static pressure decreases, the umbo vibration increases, and then starting at time 10.89 s, which corresponds to a quasi-static pressure of –70.5 Pa, the vibration decreases slightly. Compared with the umbo vibration obtained with the model of Choukir (Fig. 5-16), our model's umbo vibration has higher magnitudes and is more damped. The highest displacement of the umbo vibration in the ascending branch is around 0.7

μm for our model and 0.55 μm for Choukir's model. The difference in the vibration magnitude can presumably be attributed to the difference in the boundary conditions of the two models (see section 5.4 for discussion). In both model responses, pronounced transient effects are observed for the first three cycles as the acoustic stimulus starts. This phenomenon is only observed for the ascending branch.

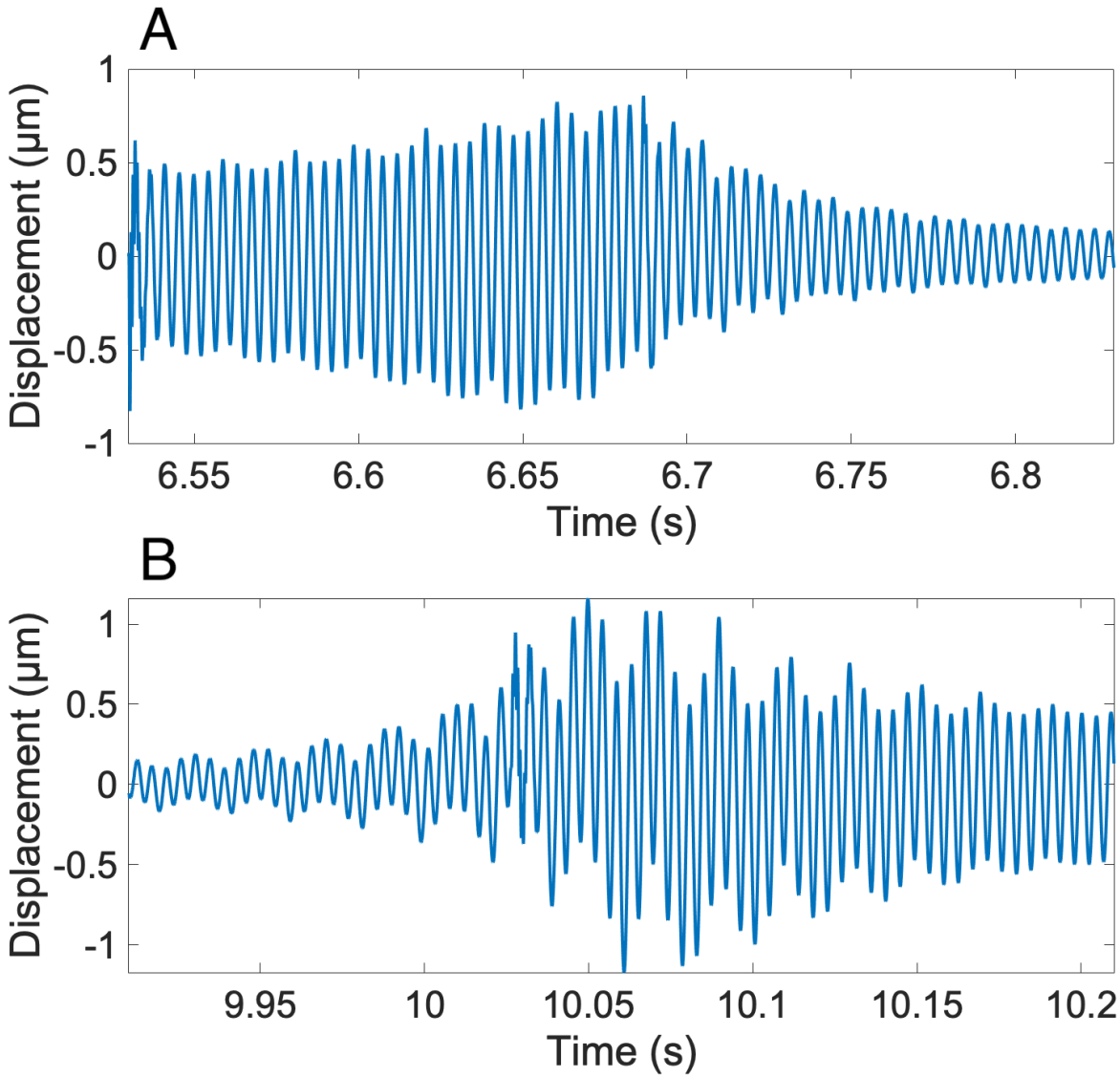

Figure 5-15: Model umbo vibration after removing the displacement induced by the quasi-static pressure sweep. A: Umbo vibration in the ascending branch. B: Umbo vibration in the descending branch.

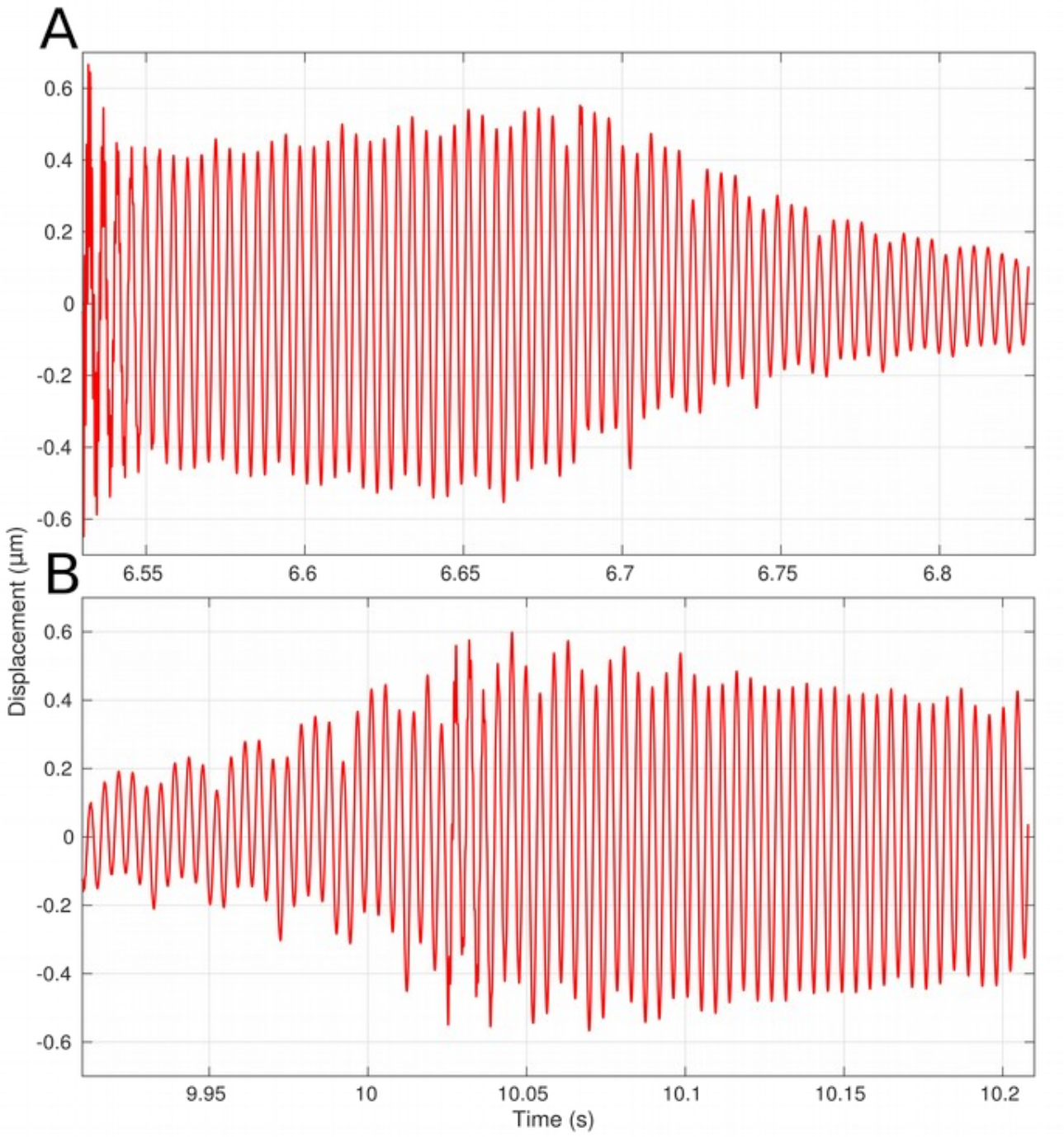

Figure 5-16: Model umbo vibration of Choukir's model after removing the displacement induced by the quasi-static pressure sweep. A: Umbo vibration in the ascending branch. B: Umbo vibration in the descending branch (Choukir, 2017).

We also observe modulation of the vibration amplitude with a period of 4 to 6 cycles. This modulation is also observable in Choukir's model. Choukir suggested two possible reasons for this

phenomenon: (1) using six Prony series time constants to express the viscoelastic effects for some components of our model leads to complex interactions between the viscoelastic effects and the frequencies of the pressure signals; or (2) the numerical integration in the FE solver.

To better understand how the amplitude of the vibration changes as a function of pressure, we extracted the amplitude envelope by performing a series of FFTs on the derivative of displacement with a moving window. We used a total of 50 windows on each 300-ms period of vibration with an 80% overlap between windows. Each window covered approximately five cycles of the 226-Hz tone. Fig. 5-17 shows the magnitude plotted as a function of static pressure for both the ascending (i.e., the positive direction) and descending (i.e., the negative direction) branches. The curve is very similar to the tympanogram that we get from clinical tympanometry except that the vertical axis represents the displacement magnitude at one point on the surface of the TM (in this case the umbo) instead of representing acoustic admittance (i.e., a normalized volume velocity corresponding to the entire TM).

The vibration magnitude is larger for negative pressure, which corresponds to our observations in section 5.3.1.1 (i.e., Fig. 5-13A). Fig. 5-17 also demonstrates the dependence of the displacement magnitude on the direction of the pressure sweep. The peak shifts negatively with the descending sweep, resulting in a peak pressure difference here equal to 36.3 Pa. The directional dependence is caused by the viscoelasticity of the components of the middle-ear model and reflects hysteresis. This feature was also demonstrated in Choukir's model with a similar PPD value of 42.8 Pa. The peak admittance in the negative direction is higher than that in the positive direction, indicating that the umbo vibrates with larger magnitude in response to the acoustic stimulus on the descending branch. Due to the many differences in the model components and material properties, the vibration displacement of our model is generally larger than that of Choukir's model.

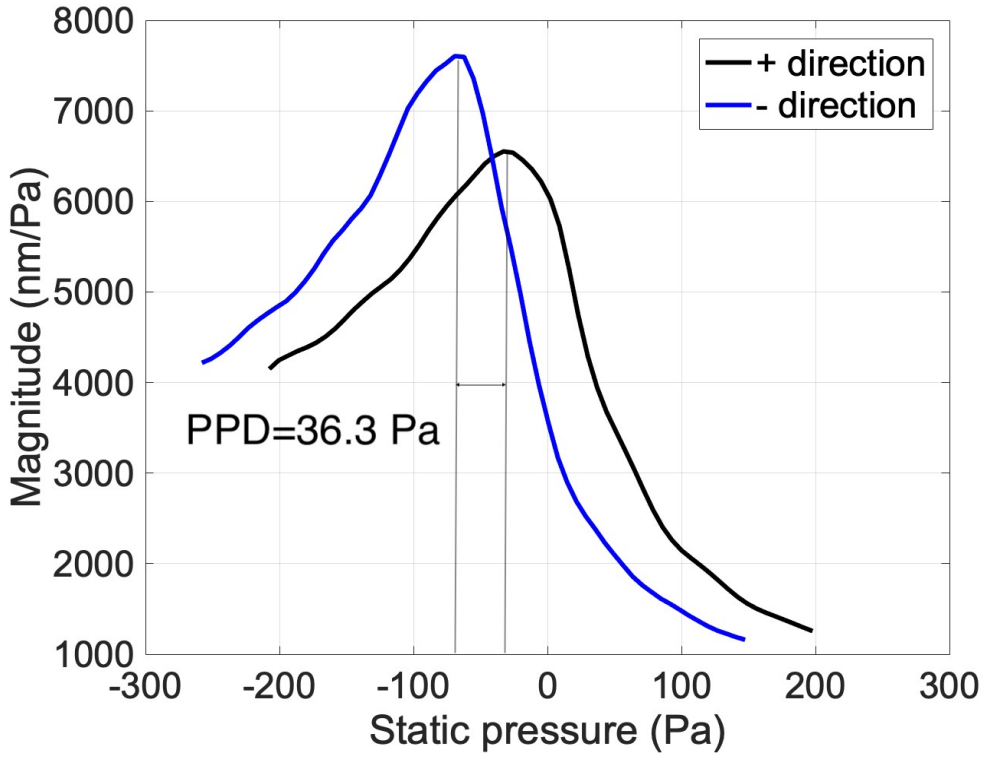

Figure 5-17: Umbo displacement normalized by sound pressure as a function of quasi-static pressure swept in both directions. PPD refers to the peak pressure difference defined in section 3.3.4.1, that is, the separation between the two pressure peaks obtained during the loading and unloading of the static pressure. "+ direction" stands for positive direction (from –2.5 kPa to +2.5 kPa) and "– direction" stands for negative direction (from +2.5 kPa to –2.5 kPa).

5.3.2 Step quasi-static pressures combined with low-amplitude sound pressures

In this section, we present the response of our model to a quasi-static pressure step, approximated by a linear increase from zero to 250 Pa in 10 ms and then maintained at a constant value. After 15 ms a 50-ms acoustic stimulus is superimposed on it, in the form of a pure tone (Fig. 5-18 A & B) or a chirp (Fig. 5-19 A & B), as described in section 4.5. The umbo displacements as a function of time are shown in panels C and D of Figs. 5-18 and 5-19. We also investigated the effect of changing the nature of the ISJ on the model response (Fig. 5-18D).

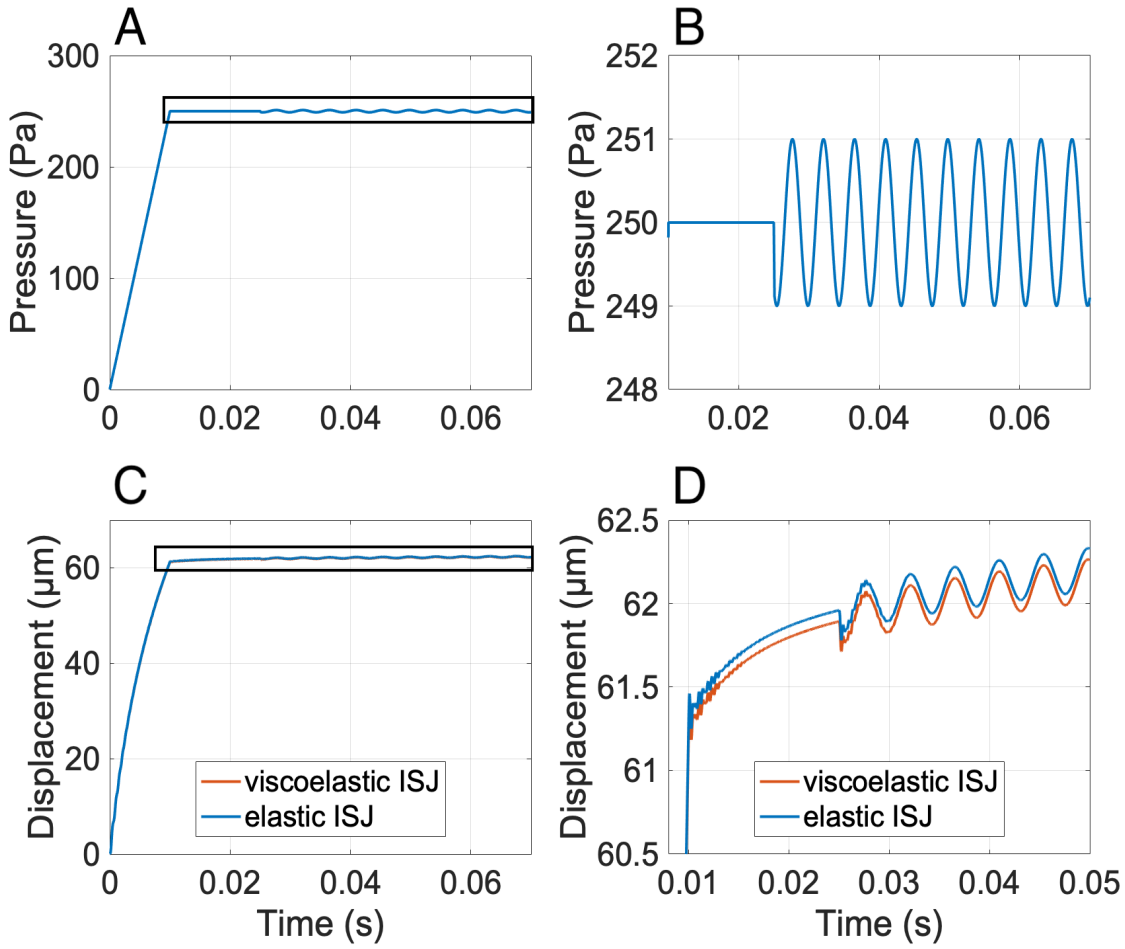

Figure 5-18: Model response to a quasi-static pressure step combined with a 226-Hz acoustic stimulus, and comparison between a viscoelastic ISJ and an elastic ISJ. A: Input pressure signal. B: Magnified view corresponding to the rectangle in A to highlight the acoustic stimulus. C: Umbo displacement as a function of time for both types of ISJ. D: Magnified view corresponding to the rectangle in C.

In Figs. 5-18C and 5-18D, we observe the umbo displacement to increase non-linearly as the static pressure increases linearly for the first 10 ms. The nature of the non-linearity is very similar to that of the model response of Choukir, but the resulting displacement of our model is about 10 μm larger than that from the model of Choukir. Then, when the pressure stays constant at 250 Pa, the displacement has a slight curvature with displacement increasing from 61.26 μm at 10 ms to 61.87 μm at 25 ms for the viscoelastic ISJ. The increase in the displacement is 0.6 μm, which is slightly smaller than the 0.7 μm reported by Choukir. Since we have time constants as high as 52 s, this slight increase in displacement

due to the quasi-static pressure could last several tens of seconds before it reaches a plateau. For the elastic ISJ response, the displacement increased from 61.37 μm to 61.97 μm, also giving us an increase of 0.6 μm. The slight curvature in the displacement response is typical of stress relaxation due to the viscoelasticity of the system. Therefore, having an elastic ISJ only increased the overall model displacement by 0.1 μm and did not affect the magnitude of the gradual increase. This indicates that the viscoelasticity of the model is predominantly provided by the TM. The displacement resulting from the sinusoidal acoustic stimulus is very close to being a pure sine wave of the same frequency riding on top of the slowly increasing response to the large pressure step. Aside from the transient effects seen at the onset, the magnitude of the vibration for the 50 ms duration is about 0.3 μm.

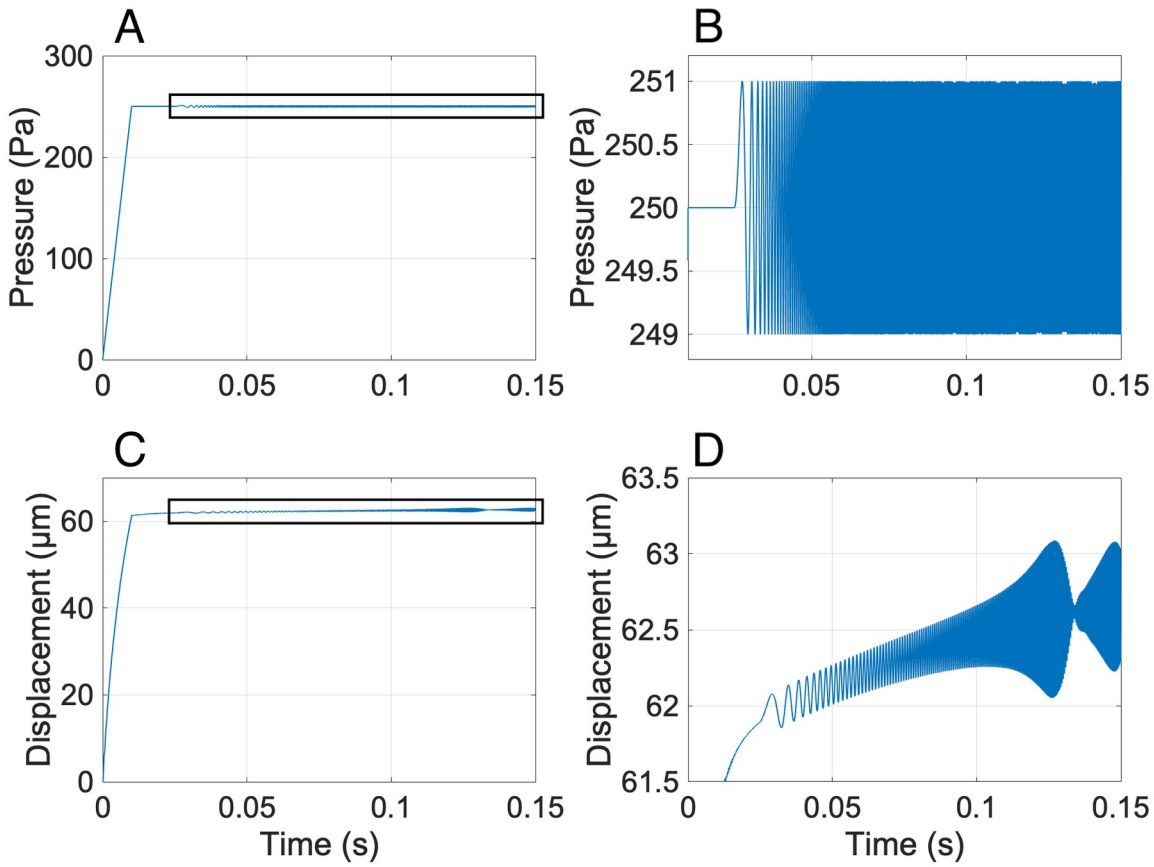

Figure 5-19: Model response to a quasi-static pressure combined with a chirp (0.12 to 3 kHz). A: Input pressure signal. B: Magnified view corresponding to the rectangle in A to highlight the acoustic stimulus. C: Umbo displacement as a function of time for an elastic ISJ. D: Magnified view corresponding to the rectangle in C.

Fig. 5-19 panels C and D show the umbo displacement when the acoustic stimulus is a chirp rather than a pure tone. For the first 25 ms, the response is the same as what is shown in Fig. 5-18. Then, the amplitude of the vibration increases from 25 ms (120 Hz chirp frequency) to 127.19 ms, decreases from there to 134.18 ms, increases again to 148.01 ms, and decreases until the end of the chirp signal. Due to the viscoelasticity of the model, the displacement at the umbo is continuing to rise even at the end of the chirp (153 ms).

When the acoustic stimulus is a chirp, simulating 150 ms of the model response lasted 32 hours in FEBio. A full pressurization cycle in the experimental study of Kose et al. (2020) is several minutes long and would be equivalent to millions of simulation steps. As a first step towards modelling a complete stepwise pressurization cycle, we simulated the response of our model to constant quasi-static pressures of different magnitudes in combination with one chirp of 128 ms. The chirp contains frequencies that increase linearly from 0.1 kHz to 10 kHz, the same as what was used as the experimental input. The simulated displacement data were differentiated using MATLAB's *diff* function, effectively converting it to velocity, and then in the frequency domain was converted back to displacement by dividing by $2\pi f$. This is equivalent to computing the difference between the model displacement data with chirp and that displacement obtained from a quasi-static step input without a chirp, but is faster because the response without a chirp does not need to be simulated. We applied only cochlear damping in the model without increasing the Prony-series coefficient at 10 μs. The normalized frequency response of our model due to chirps in the presence of a range of quasi-static pressures is presented in Fig. 5-20A, and equivalent experimental data obtained by Kose et al. (2020) in one gerbil is presented in Fig. 5-20B. Our model responses show trends similar to what is seen in the experimental measurements. As the magnitude of the quasi-static pressure increases from 0 Pa to +2500 Pa, the magnitude of the simulated low-frequency response decreases by a factor of 7.6, compared with a

factor of 4.1 for the experimental data; the decreasing magnitudes started to plateau earlier for the model results. The frequency of the resonance peak shifted towards higher frequencies. We did not observe a strong indication of the experimental R1 peaks (marked by circles, filled and unfilled, in panel B) in our simulated frequency response, but the frequencies of the R2 peaks in the simulated responses are similar to the experimental ones. The highest peaks of the 500-Pa (red), 1000-Pa (green), 1500-Pa (blue), 2000-Pa (yellow) and 2500-Pa (cyan) pressurized vibrations are approximately 3.9 kHz, 5 kHz, 5.5 kHz, 6 kHz and 6.5 kHz in our model and the R2 peaks are at 4.8 kHz, 5.5 kHz, 6.5 kHz, 7 kHz and 8 kHz in the experimental data, respectively. Our model's pressurized frequency responses showed multiple peaks at frequencies around and higher than that of the highest peak. These multiple peaks are not seen in the experimental data, presumably because of damping that was heavier than in our model.

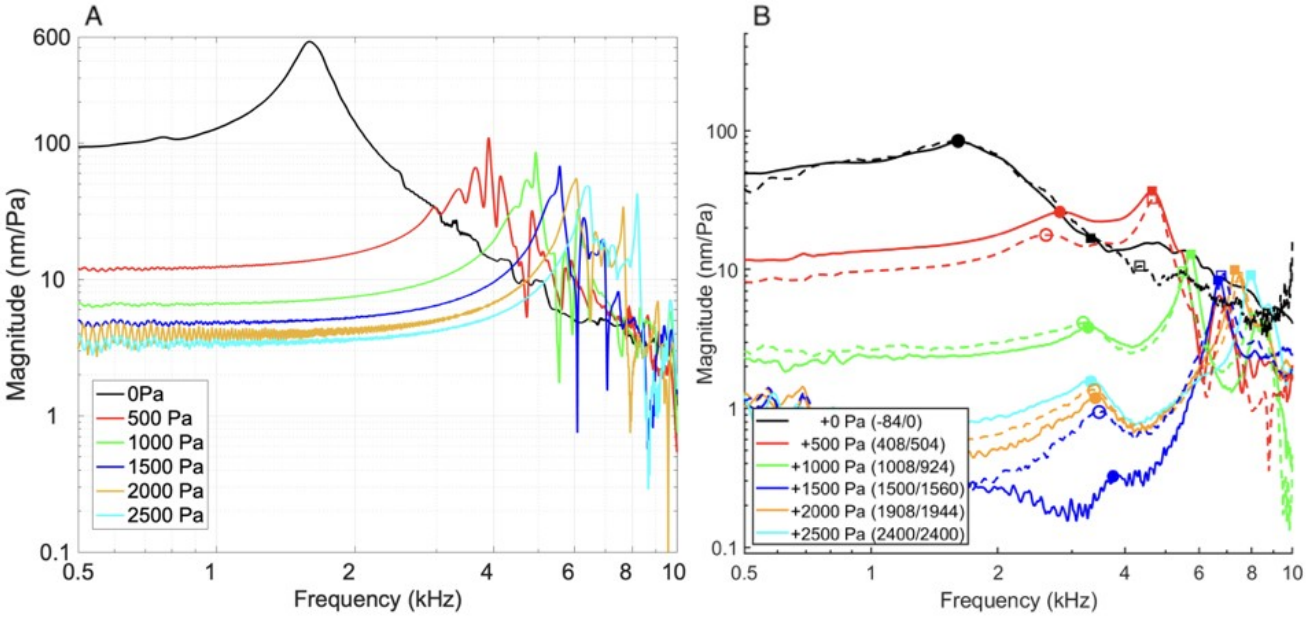

Figure 5-20: Comparison of our model responses with normalized vibration data at the gerbil umbo in Kose et al. (2020), in response to quasi-static pressures with different magnitude in combination with a chirp (0.12 kHz to 10 kHz). Here, a frequency range of 0.5 kHz to 10 kHz was selected to match the experimental data.

5.4 Discussion

For our Code_Aster model, we noticed that the model response at the umbo was not sensitive to changes in the spring constants of the lateral two sets of springs on the two ends of wedge 1. Although we intended to use these springs to provide the ossicular stiffness, the stiffness currently is mostly provided by the annular ligament springs on the stapes footplate. Therefore, the axis spring constants, and thus also the stapes spring constants, need to be reconsidered.

For the model response to the pressurized sweeps, we observed an asymmetry in our pressure versus displacement curves (Fig. 5-12 and Fig. 5-13A). Dirckx and Decraemer (2001) suggested that the TM motion in response to negative pressures is strongly affected by ossicular mechanics, while its motion at positive pressures is mainly influenced by the elastic properties of the TM itself. The discrepancies between the magnitudes of TM vibration at negative pressures obtained by our model and those obtained experimentally might be explained by the fact that our model does not accurately represent the ossicular mechanics. This can also be related to our observation with the model response to a pure-tone acoustic stimulus on top of a quasi-static pressure ramp. When changing the ISJ from viscoelastic to elastic, we observed a decrease in the magnitude of the umbo motion. Due to the simplicity of our ISJ structure, without curvature and individual ISJ components being modelled, it is hard to conclude what the decrease in magnitude indicates about the functionality of the ISJ.

For the model response to the 226-Hz pure tone in the presence of quasi-static sweeps, we obtained a difference between the pressure peaks 36.3 Pa (Fig. 5-17). The value of the PPD is directly dependent on the amount of hysteresis in the model response. Our model showed a smaller amount of hysteresis than Choukir's model did (Fig. 5-13), and consequently we obtained a lower PPD value than hers (42.8 Pa). Therkildsen and Gaihede (2005) reported a constant PPD of 120 Pa measured with live humans for pump speeds from 500 Pa/s to 4000 Pa/s. On the contrary, as discussed in section 5.3.1.1, Dirckx et al.

(2006) reported higher umbo hysteresis at lower pressure-change rates measured with *post mortem* rabbits. It is not clear to us whether the difference in species and/or the difference in experimental procedure could lead to the discrepancy.

Our simulated frequency responses at the umbo for a chirp on top of static-pressure steps were a first step towards replicating the experimental LDV measurements of Kose et al. (2020). We observed trends similar to those observed experimentally in terms of low-frequency magnitudes and resonance peak frequencies, but we observed multiple closely spaced peaks as low as 3 kHz, which was not seen experimentally. For the experimental measurements, because of laser tracking problems, the first chirps after a step were not reliable and later chirps were used, while we only simulated the model response to one chirp after a step to reduce computation cost. In our model response, because of the short period of simulation, the magnitude of the acoustic signal is much smaller than the magnitude of the on-going viscoelastic effect. We should simulate later chirps to see if it makes a difference. Due to the complexity of the many middle-ear components and our lack of knowledge about the masses and corresponding moments of inertia of those components of the gerbil middle ear, we cannot relate these peaks to particular middle-ear components.

Chapter 6: Conclusion

6.1 Summary

In this study, we developed a FE model of the gerbil middle ear and studied its response under conditions similar to those involved in clinical tympanometry, namely, a combination of large quasi-static pressures and low-amplitude acoustic pressures. We updated the previous model of Choukir (2017) by inserting distinct components for the ISJ, the pedicle, the lenticular plate and the stapes. We also added spring representations of the ligaments. We defined a fixed axis of rotation for the malleus and incus. We used two different FE solvers: Code_Aster, for model verification and analysis within the linear regime, and FEBio, for both linear and non-linear analysis.

For the Code_Aster model, we used isotropic elastic material properties and stiffness-proportional Rayleigh damping for all components. The model's small-amplitude frequency responses were compared with the model of Maftoon et al. (2015), and material properties were adjusted accordingly. The cochlear damping was modelled using four dashpots perpendicular to the stapes footplate. The magnitude of the Rayleigh parameter was increased compared to that used in the model of Maftoon et al. to match the resonance peak.

For the FEBio model, we employed a quasi-linear visco-hyperelastic model to describe the viscoelastic behaviour of the middle ear. The TM and the ISJ were described by the Mooney-Rivlin hyperelastic model. The other components were modelled as isotropic elastic. The elastic properties of the model components were determined by comparing the small-amplitude frequency responses of our model with the model of Maftoon et al. (2015). The viscoelastic response was defined with six Prony-series time constants, equally spaced logarithmically, covering a frequency range of 3 mHz to 16 kHz, effectively covering the range from ultra-low quasi-static pressure change rates to the frequencies of

the acoustic stimuli in tympanometry. As done by Choukir (2017), the Prony-series coefficients of the PF were adjusted to match the feature in the umbo response that reflected coupling between the PT and the PF. As done for the Code_Aster model, the cochlear damping was modelled using dashpots. To provide enough damping for the model, the Prony-series coefficients of other structures were adjusted to match the magnitude of the low-frequency response produced by the model of Maftoon et al. Overall, both the Code_Aster and FEBio models showed a small-amplitude response similar to that of the model of Maftoon et al. for frequencies up to 3 kHz.

As done by Choukir (2017), we explored the responses of our model to large quasi-static pressures in the form of triangular sweeps, with and without superimposed low-frequency acoustic stimuli, with pressure-change rates of 200 Pa/s to 1500 Pa/s. As previously observed, the umbo displacement was larger for the positive pressures than for the negative pressures. As Choukir did, we observed constant hysteresis for different pressure-change rates, although Dirckx et al. (2006) reported increasing hysteresis with decreasing pressure-change rates. We also compared the PT displacements at positive and negative pressures to those measured by Dirckx and Decraemer (2001); the PT displacements at negative pressures were substantially larger in our model.

We repeated Choukir's investigation of the model umbo response to low-frequency pure tones applied on top of pressure sweeps at a pressure-change rate of 1500 Pa/s. The simulated static-pressure-induced variations in the umbo vibration magnitude for ascending and descending pressure sweeps resemble some features of clinical tympanograms: (1) the asymmetrical effects of positive and negative pressures; and (2) the peak pressure difference that is a result of hysteresis. In addition to Choukir's investigations of pressure sweeps, we studied our model's response to low-frequency acoustic stimuli applied on top of quasi-static pressure steps, and also compared the effect of elastic and viscoelastic versions of our new ISJ component. The model results suggest that the viscoelasticity of the TM affects

umbo vibrations more than does that of the ISJ. Finally, in response to acoustic chirps (from 0.1 kHz to 10 kHz) superimposed on quasi-static pressure steps of between +500 Pa and +2500 Pa (as done by Kose et al., 2020), our model produced frequency responses that exhibited trends similar to those seen in the experimental results in terms of the low-frequency magnitude decrease and resonance peak shift to higher frequencies when the magnitude of pressurization increased.

6.2 Future work

Although our model was able to produce results similar to some aspects of experimental data, there are some discrepancies and further work is required. Developing a model with realistic geometry and *a priori* knowledge of the material properties is challenging. One reason is the wide range of possible choices that can be made during the calibration of a model, especially when using an oversimplified and somewhat arbitrary geometry for parts of the model. Sensitivity analyses on separate model components are essential to understand the relative influences of some of these choices. For example, for both the Code_Aster and FEBio models, we should explore the TM thickness, geometry and curvature; the spring constants of the annular ligament springs and the springs on the axis of rotation; the damping coefficient of the dashpots on the stapes footplate; and the thickness and Young's modulus of the wedges. Specifically for the springs on the axis of rotation, future work should define the annular ligament spring constants *a priori* by numerical simulation on just the stapes footplate, or by direct experimental measurement, and then investigate the spring constants required on the wedge (possibly increasing the thickness of the wedge) to an appropriate stiffness at the rotational axis.

For the FEBio model, we should explore the effects of the parameters of the Mooney-Rivlin model and try different hyperelastic material models, and also explore the effects of the relaxation coefficients for each Prony-series time constant. Future work should determine the low-amplitude effective Young's modulus of the hyperelastic part of the viscoelastic material properties *a priori*. We did not observe PT

buckling at low pressure-change rates as Choukir (2017, figs. 5–12) did. The discrepancy could indicate that the hyperelastic part of the TM material properties requires adjustment.

The present model still includes a considerable degree of simplification of the manubrium, ossicles, joints and ligaments. Further improvements of the model can be made by introducing more realistic component geometries (i.e., taken from the model of Maftoon et al.) and perhaps by taking into account the anisotropy and multiple layers of the TM. The geometry of the model components can strongly affect how they contribute to the model response. For example, Soleimani et al. (2020) found that the curvature of the ISJ joint capsule affected the joint response during tensile tests. More realistic compartments and geometry of the ISJ are required to really evaluate the effects of the ISJ on the model response. However, more complex geometries will require significantly greater computational power, in addition to introducing more parameters to be determined. Utilization of the supercomputer was helpful but only reduced run time by approximately 20%. Using multiple solution phases, with smaller step sizes when there are acoustic stimuli or large pressure transients, is not useful when those conditions continue for a long period. Therefore, it is essential to determine which model features are important, and where there are opportunities for decreased mesh resolution.

Future work should also investigate the pressurized vibrations of other components of the middle ear, for example, at the ISJ and at the stapes, to study the functionality of different middle-ear components. Since we do have a pedicle structure in the model, future work could also investigate the possible effects of pedicle bending (Funnell et al., 2005) in pressurized vibration responses. We did not investigate further for this thesis for lack of time and because there are few good data for comparison, but the recent pressurized ISJ measurements in our group by Feizollah (2019) using X-ray nanoCT and light-sheet imaging, as well as microscopic video and optical-flow processing, will be very useful for this purpose.

For the experimental pressurized LDV data of Kose et al. (2020), we only compared our model response to the positive static-pressure steps and encountered numerical problems when attempting to apply negative steps. Future work should simulate the model response to negative static-pressure steps. We noticed that the effect of viscoelasticity lasted through the period of the chirp acoustic input. Therefore, future work should extend the time of simulation until the viscoelastic effect is very small so that results from a full experimental pressurization cycle can be compared.

As discussed earlier, without more realistic component geometries, it is unclear to us which components of the middle ear contributed to the multiple peaks that we observed around the main resonance frequency under quasi-static pressurization. As more components are added to the model, we should be able to identify individual frequency-response peak features with distinct components of the middle ear, and thus gain a better understanding of the middle-ear response to quasi-static pressures.

6.3 Significance

Our model is an enhancement of the previous model of Choukir (2017), with more anatomical details. We confirmed Choukir's modelling of certain aspects of the response of the middle ear to both quasi-static pressures and acoustic pressures, presented a very preliminary look at the possible effects of the ISJ, and also presented a promising comparison to the new experimental data of Kose et al. (2020). Our model provides a tool to explore the complex interactions between the quasi-static and acoustic measurements, which can be used to improve our understanding of clinical tympanometry. Although our model was developed for gerbils, and the high-quality data that are available for gerbil ears, the ultimate goal is to study tympanometry performed in humans and particularly in newborns.

References

Aernouts, J., Aerts, J.R.M., Dirckx, J.J.J., 2012. Mechanical properties of human tympanic membrane in the quasi-static regime from in situ point indentation measurements. Hear Res 290, 45–54. https://doi.org/10.1016/j.heares.2012.05.001

Aernouts, J., Dirckx, J.J.J., 2012a. Static versus dynamic gerbil tympanic membrane elasticity: Derivation of the complex modulus. Biomech Model Mechanobiol 11, 829–840. https://doi.org/10.1007/s10237-011-0355-6

Aernouts, J., Dirckx, J.J.J., 2012b. Viscoelastic properties of gerbil tympanic membrane at very low frequencies. J Biomech 45, 919–924. https://doi.org/10.1016/j.jbiomech.2012.01.023

Aernouts, J., Soons, J.A.M., Dirckx, J.J.J., 2010. Quantification of tympanic membrane elasticity parameters from in situ point indentation measurements: Validation and preliminary study. Hear Res, MEMRO 2009: Middle-Ear Science and Technology 263, 177–182. https://doi.org/10.1016/j.heares.2009.09.007

Agache, P.G., Monneur, C., Leveque, J.L., De Rigal, J., 1980. Mechanical properties and Young's modulus of human skin in vivo. Arch Dermatol Res 269, 221–232. https://doi.org/10.1007/BF00406415

Alaerts, J., Luts, H., Wouters, J., 2007. Evaluation of middle ear function in young children: Clinical guidelines for the use of 226- and 1,000-Hz tympanometry. Otol Neurotol 28, 727–732. https://doi.org/10.1097/MAO.0b013e3180dca1e5

Békésy, G.V., 1960. Experiments In Hearing. McGraw-Hill, New York, NY.

Bennett, B.M., 1972. On comparisons of sensitivity, specificity and predictive value of a number of diagnostic procedures. Biometrics 28, 793–800. https://doi.org/10.2307/2528763

Bogičević, L., Verhoeven, M., van Baar, A., 2018. Chapter 30 - Evaluation of the Human Newborn Infant, in: Slikker, W., Paule, M.G., Wang, C. (Eds.), Handbook of Developmental Neurotoxicology (Second Edition). Academic Press, pp. 351–362. https://doi.org/10.1016/B978-0-12-809405-1.00030-4

Borg, E., Counter, S.A., 1989. The middle-ear muscles. Sci Am 261, 74–81.

Calandruccio, L., Fitzgerald, T., Prieve, B., 2006. Normative multifrequency tympanometry in infants and toddlers. J Am Acad Audiol 17, 470–80. https://doi.org/10.3766/jaaa.17.7.2

Carmo, M.P., Costa, N.T. de O., Momensohn-Santos, T.M., 2013. Tympanometry in infants: A study of the sensitivity and specificity of 226-Hz and 1,000-Hz probe tones. Int Arch Otorhinolaryngol 17, 395–402. https://doi.org/10.1055/s-0033-1351678

Chae, S.-H., Zhao, J.-H., Edwards, D., Ho, P., 2010. Characterization of the viscoelasticity of molding compounds in the time domain. J Electron Mater 39, 419–425. https://doi.org/10.1007/s11664-010-1078-7

Charlebois, M., Motallebzadeh, H., Funnell, W.R.J., 2013. Visco-hyperelastic law for finite deformations: A frequency analysis. Biomech Model Mechanobiol 12, 705–715. https://doi.org/10.1007/s10237-012-0435-2

Cheng, J.T., Aarnisalo, A.A., Harrington, E., Hernandez-Montes, M. del S., Furlong, C., Merchant, S.N., Rosowski, J.J., 2010. Motion of the surface of the human tympanic membrane measured with stroboscopic holography. Hear Res 263, 66–77. https://doi.org/10.1016/j.heares.2009.12.024

Cheng, T., Dai, C., Gan, R.Z., 2007a. Viscoelastic properties of human tympanic membrane. Ann Biomed Eng 35, 305–314. https://doi.org/10.1007/s10439-006-9227-0

Cheng, T., Dai, C., Gan, R.Z., 2007b. Viscoelastic properties of human tympanic membrane. Ann Biomed Eng 35, 305–314. https://doi.org/10.1007/s10439-006-9227-0

Cheng, T., Gan, R.Z., 2008a. Experimental measurement and modeling analysis on mechanical properties of tensor tympani tendon. Med Eng Phys 30, 358–366. https://doi.org/10.1016/j.medengphy.2007.04.005

Cheng, T., Gan, R.Z., 2008b. Mechanical properties of anterior malleolar ligament from experimental measurement and material modeling analysis. Biomech Model Mechanobiol 7, 387–394. https://doi.org/10.1007/s10237-007-0094-x

Cheng, T., Gan, R.Z., 2007. Mechanical properties of stapedial tendon in human middle ear. J Biomech Eng 129, 913–918. https://doi.org/10.1115/1.2800837

Chole, R.A., Kodama, K., 1989. Comparative histology of the tympanic membrane and its relationship to cholesteatoma. Ann Otol Rhinol Laryngol 98, 761–766. https://doi.org/10.1177/000348948909801002

Choukir, S., 2017. Finite-element modelling of tympanic-membrane vibrations under quasi-static pressurization (M.Eng. Thesis). McGill University, Canada.

Colletti, V., 1977. Multifrequency tympanometry. Audiology 16, 278–287. https://doi.org/10.3109/00206097709071839

Colletti, V., 1975. Methodologic observations on tympanometry with regard to the probe tone frequency. Acta Otolaryngol. 80, 54–60. https://doi.org/10.3109/00016487509121300

Colletti, V., Fiorino, F.G., Sittoni, V., Policante, Z., 1993. Mechanics of the middle ear in otosclerosis and stapedoplasty. Acta Otolaryngol 113, 637–641. https://doi.org/10.3109/00016489309135877

Daniel, S.J., Funnell, R.W.J., Zeitouni, A.G., Schloss, M.D., Rappaport, J., 2001. Clinical applications of a finite-element model of the human middle ear. J Otolaryngol 30, 340–346. https://doi.org/10.2310/7070.2001.19393

Daphalapurkar, N.P., Dai, C., Gan, R.Z., Lu, H., 2009. Characterization of the linearly viscoelastic behavior of human tympanic membrane by nanoindentation. J Mech Behav Biomed Mater 2, 82–92. https://doi.org/10.1016/j.jmbbm.2008.05.008

De Greef, D., Pires, F., Dirckx, J.J.J., 2017. Effects of model definitions and parameter values in finite element modeling of human middle ear mechanics. Hear Res 344, 195–206. https://doi.org/10.1016/j.heares.2016.11.011

de La Rochefoucauld, O., Decraemer, W.F., Khanna, S.M., Olson, E.S., 2008. Simultaneous measurements of ossicular velocity and intracochlear pressure leading to the cochlear input impedance in gerbil. J Assoc Res Otolaryngol 9, 161–177. https://doi.org/10.1007/s10162-008-0115-1

de La Rochefoucauld, O., Olson, E.S., 2010. A sum of simple and complex motions on the eardrum and manubrium in gerbil. Hear Res 263, 9–15. https://doi.org/10.1016/j.heares.2009.10.014

de Moraes, T.F.D., Macedo, C. de C., Feniman, M.R., 2012. Multifrequency tympanometry in infants. Int Arch Otorhinolaryngol 16, 186–194. https://doi.org/10.7162/S1809-97772012000200006

Decraemer, W.F., Creten, W.L., Van Camp, K.J., 1984. Tympanometric middle-ear pressure determination with two-component admittance meters. Scand Audiol 13, 165–172. https://doi.org/10.3109/01050398409043056

Decraemer, W.F., Dirckx, J.J.J., Funnell, W.R.J., 2003. Three-dimensional modelling of the middle-ear ossicular chain using a commercial high-resolution x-ray ct scanner. J Assoc Res Otolaryngol 4, 250–263. https://doi.org/10.1007/s10162-002-3030-x

Decraemer, W.F., Funnell, W.R.J., 2008. Anatomical and mechanical properties of the tympanic membrane, in: Chronic Otitis Media: Pathogenesis-Oriented Therapeutic Management. Kugler, The Hague, pp. 51–84.

Decraemer, W.F., Khanna, S.M., Funnell, R.W.J., 1989. Interferometric measurement of the amplitude and phase of tympanic membrane vibrations in cat. Hear Res 38, 1–17. https://doi.org/10.1016/0378-5955(89)90123-8

Decraemer, W.F., Maes, M.A., Vanhuyse, V.J., 1980. An elastic stress-strain relation for soft biological tissues based on a structural model. J Biomech 13, 463–468. https://doi.org/10.1016/0021-9290(80)90338-3

Dirckx, J.J.J., Buytaert, J.A.N., Decraemer, W.F., 2006. Quasi-static transfer function of the rabbit middle ear, measured with a heterodyne Interferometer with high-resolution position decoder. J Assoc Res Otolaryngol 7, 339–351. https://doi.org/10.1007/s10162-006-0048-5

Dirckx, J.J.J., Decraemer, W.F., 2001. Effect of middle ear components on eardrum quasi-static deformation. Hear Res 157, 124–137. https://doi.org/10.1016/S0378-5955(01)00290-8

Dirckx, J.J.J., Decraemer, W.F., von Unge, M., Larsson, C., 1998. Volume displacement of the gerbil eardrum pars flaccida as a function of middle ear pressure. Hear Res 118, 35–46. https://doi.org/10.1016/S0378-5955(98)00025-2

Elkhouri, N., Liu, H., Funnell, W.R.J., 2006. Low-frequency finite-element modeling of the gerbil middle ear. J Assoc Res Otolaryngol 7, 399–411. https://doi.org/10.1007/s10162-006-0055-6

Ellaham, N.N., Akarche, F., Funnell, W.R.J., Daniel, S.J., 2007. Experimental study of the effects of drying on middle-ear vibrations in the gerbil. CMBES Proceedings 30.

Elner, Å., Ingelstedt, S., Ivarsson, A., 1971. The elastic properties of the tympanic membrane system. Acta Oto-Laryngologica 72, 397–403. https://doi.org/10.3109/00016487109122499

Fay, J., Puria, S., Decraemer, W.F., Steele, C., 2005. Three approaches for estimating the elastic modulus of the tympanic membrane. J Biomech 38, 1807–1815.

Feizollah, S., 2019. Microstructure and displacements of the gerbil incudostapedial joint under static pressures (M.Eng. Thesis). McGill University, Canada.

Feldman, A.S., 1976. Tympanometry: Application and interpretation. Ann Otol Rhinol Laryngol 85, 202–208. https://doi.org/10.1177/00034894760850S238

Feldman, R., Fria, T., Palfrey, C., Dellecker, C., 1984. Effects of rate of air pressure change on tympanometry. Ear and Hearing 5, 91–95.

Ferekidis, E., Vlachou, S., Douniadakis, D., Apostolopoulos, N., Adamopoulos, G., 1999. Multiple-frequency tympanometry in children with acute otitis media. Otolaryngol Head Neck Surg 121, 797–801. https://doi.org/10.1053/hn.1999.v121.a91893

Funasaka, S., Funai, H., Kumakawa, K., 1984. Sweep-frequency tympanometry: Its development and diagnostic value. Audiology 23, 366–379. https://doi.org/10.3109/00206098409081530

Fung, Y.-C., 1993. Bioviscoelastic Solids, in: Fung, Y.-C. (Ed.), Biomechanics: Mechanical Properties of Living Tissues. Springer, New York, NY, pp. 242–320. https://doi.org/10.1007/978-1-4757-2257-4_7

Funnell, W.R.J., 1983. On the undamped natural frequencies and mode shapes of a finite-element model of the cat eardrum. J Acoust Soc Am 73, 1657–1661. https://doi.org/10.1121/1.389386

Funnell, W.R.J., Decraemer, W.F., 1996. On the incorporation of moiré shape measurements in finite-element models of the cat eardrum. J Acoust Soc Am 100, 925–932. https://doi.org/10.1121/1.416252

Funnell, W.R.J., Decraemer, W.F., Khanna, S.M., 1987. On the damped frequency response of a finite-element model of the cat eardrum. J Acoust Soc Am 81, 1851–1859. https://doi.org/10.1121/1.394749

Funnell, W.R.J., Heng Siah, T., McKee, M.D., Daniel, S.J., Decraemer, W.F., 2005. On the coupling between the incus and the stapes in the cat. J Assoc Res Otolaryngol 6, 9–18. https://doi.org/10.1007/s10162-004-5016-3

Funnell, W.R.J., Laszlo, C.A., 1982. A critical review of experimental observations on ear-drum structure and function. ORL 44, 181–205. https://doi.org/10.1159/000275593

Funnell, W.R.J., Laszlo, C.A., 1978. Modeling of the cat eardrum as a thin shell using the finite-element method. J Acoust Soc Am 63, 1461–1467. https://doi.org/10.1121/1.381892

Funnell, W.R.J., Maftoon, N., Decraemer, W.F., 2017. Mechanics and modelling for the middle ear [WWW Document]. URL http://audilab.bme.mcgill.ca/mammie/

Gaihede, M., 1996. Tympanometric preconditioning of the tympanic membrane. Hear Res 102, 28–34. https://doi.org/10.1016/S0378-5955(96)00146-3

Gan, R.Z., Yang, F., Zhang, X., Nakmali, D., 2011. Mechanical properties of stapedial annular ligament. Med Eng Phys 33, 330–339. https://doi.org/10.1016/j.medengphy.2010.10.022

Geuzaine, C., Remacle, J.-F., 2009. Gmsh: A 3-D finite element mesh generator with built-in pre- and post-processing facilities. Int J Numer Methods Eng 79, 1309–1331. https://doi.org/10.1002/nme.2579

Ghosh, S.S., Funnell, W.R.J., 1995. On the effects of incudostapedial joint flexibility in a finite-element model of the cat middle ear, in: Proceedings of 17th International Conference of the Engineering in Medicine and Biology Society. pp. 1437–1438 vol.2. https://doi.org/10.1109/IEMBS.1995.579765

Giannini, P., Marciano, E., Saulino, C., Strano, C.G., Alessio, M., Marcelli, V., Auletta, G., 1997. Middle ear involvement in children with chronic rheumatoid juvenile arthritis. Eur Arch Otorhinolaryngol 254 Suppl 1, S30-33. https://doi.org/10.1007/bf02439717

Gottlieb, P.K., Vaisbuch, Y., Puria, S., 2018. Human ossicular-joint flexibility transforms the peak amplitude and width of impulsive acoustic stimuli. J Acoust Soc Am 143, 3418–3433. https://doi.org/10.1121/1.5039845

Govindjee, S., Reese, S., 1997. A presentation and comparison of two large deformation viscoelasticity models. J Eng Mater Technol 119, 251–255. https://doi.org/10.1115/1.2812252

Hackett, R., 2015. Hyperelasticity Primer. Springer, Cham, Switzerland. https://doi.org/10.1007/978-3-319-23273-7

He, Z., 2012. Vibration measurements on the widely exposed gerbil eardrum (M.Eng. Thesis). McGill University, Canada.

Holzapfel, G.A., 2000. Nonlinear Solid Mechanics: A Continuum Approach for Engineering. Wiley, Chichester.

Huang, G., Daphalapurkar, N.P., Gan, R.Z., Lu, H., 2008. A method for measuring linearly viscoelastic properties of human tympanic membrane using nanoindentation. J Biomech Eng 130, 014501–1 to 014501–7. https://doi.org/10.1115/1.2838034

Humphrey, J. d., 2003. Review paper: Continuum biomechanics of soft biological tissues. P Roy Soc A-Math Phy 459, 3–46. https://doi.org/10.1098/rspa.2002.1060

Iacovou, E., Vlastarakos, P.V., Ferekidis, E., Nikolopoulos, T.P., 2013. Multi-frequency tympanometry: Clinical applications for the assessment of the middle ear status. Indian J Otolaryngol Head Neck Surg 65, 283–287. https://doi.org/10.1007/s12070-011-0470-9

Irgens, F., 2008. Deformation Analysis, in: Irgens, F. (Ed.), Continuum Mechanics. Springer, Berlin, Heidelberg, pp. 133–181. https://doi.org/10.1007/978-3-540-74298-2_5

Jerger, J., 1970. Clinical experience with impedance audiometry. Arch Otolaryngol 92, 311–324. https://doi.org/10.1001/archotol.1970.04310040005002

Karmody, C.S., Northrop, C.C., Levine, S.R., 2009. The incudostapedial articulation: New concepts. Otol Neurotol 30, 990–997. https://doi.org/10.1097/MAO.0b013e3181b0fff7

Kassem, F., Ophir, D., Bernheim, J., Berger, G., 2010. Morphology of the human tympanic membrane annulus. Otolaryngol Head Neck Surg 142, 682–687. https://doi.org/10.1016/j.otohns.2010.01.020

Keefe, D.H., Simmons, J.L., 2003. Energy transmittance predicts conductive hearing loss in older children and adults. J Acoust Soc Am 114, 3217–3238. https://doi.org/10.1121/1.1625931

Keith, R.W., 1973. Impedance audiometry with neonates. Arch Otolaryngol 97, 465–467. https://doi.org/10.1001/archotol.1973.00780010479007

Kemp, D.T., 2002. Otoacoustic emissions, their origin in cochlear function, and use. Br Med Bull 63, 223–241. https://doi.org/10.1093/bmb/63.1.223

Khanna, S.M., Tonndorf, J., 1972. Tympanic Membrane Vibrations in Cats Studied by Time-Averaged Holography. J Acoust Soc Am 51, 1904–1920. https://doi.org/10.1121/1.1913050

Kilic, A., Baysal, E., Karatas, E., Baglam, T., Durucu, C., Deniz, M., Kanlikama, M., Mumbuc, S., 2012. The role of high frequency tympanometry in newborn hearing screening programme. Eur Rev Med Pharmacol Sci 16, 220–223.

Kirikae, I., 1960. The structure and function of the middle ear. Tokyo: University of Tokyo Press.

Knauss, W.G., Zhao, J., 2007. Improved relaxation time coverage in ramp-strain histories. Mech Time-Depend Mater 11, 199–216. https://doi.org/10.1007/s11043-007-9035-4

Kobayashi, T., Okitsu, T., Endo, S., Kawamoto, K., 1985. Forward-backward tracing tympanometry in the diagnosis of middle ear pressure. Auris Nasus Larynx 12, S219–S221. https://doi.org/10.1016/S0385-8146(85)80155-3

Kochkin, R.V., 2006. Multifrequency and multicomponent tympanometry, in: Impedance Audiometry. Medicine, Moscow.

Konrádsson, K.S., Ivarsson, A., Bank, G., 1987. Computerized laser doppler interferometric scanning of the vibrating tympanic membrane. Scand Audiol 16, 159–166. https://doi.org/10.3109/01050398709042171

Kose, O., Funnell, W.R.J., Daniel, S.J., 2020. Vibration measurements of the gerbil eardrum under quasi-static pressure steps. J Assoc Res Otolaryngol Manuscript under revision.

Kuypers, L.C., Decraemer, W.F., Dirckx, J.J.J., 2006. Thickness distribution of fresh and preserved human eardrums measured with confocal microscopy. Otol. Neurotol. 27, 256–264. https://doi.org/10.1097/01.mao.0000187044.73791.92

Kuypers, L.C., Dirckx, J.J.J., Decraemer, W.F., Timmermans, J.-P., 2005. Thickness of the gerbil tympanic membrane measured with confocal microscopy. Hear Res 209, 42–52. https://doi.org/10.1016/j.heares.2005.06.003

Ladak, H.M., Decraemer, W.F., Dirckx, J.J.J., Funnell, W.R.J., 2004. Response of the cat eardrum to static pressures: Mobile versus immobile malleus. J Acoust Soc Am 116, 3008–3021. https://doi.org/10.1121/1.1802673

Ladak, H.M., Funnell, W.R.J., Decraemer, W.F., Dirckx, J.J.J., 2006. A geometrically nonlinear finite-element model of the cat eardrum. J Acoust Soc Am 119, 2859–2868. https://doi.org/10.1121/1.2188370

Lee, C.-Y., Rosowski, J.J., 2001. Effects of middle-ear static pressure on pars tensa and pars flaccida of gerbil ears. Hear Res 153, 146–163. https://doi.org/10.1016/S0378-5955(00)00269-0

Lemmerling, M.M., Stambuk, H.E., Mancuso, A.A., Antonelli, P.J., Kubilis, P.S., 1997. CT of the normal suspensory ligaments of the ossicles in the middle ear. Am J Neuroradiol 18, 471–477.

Lidén, G., 1969. Tests for Stapes Fixation. Arch Otolaryngol 89, 399–403. https://doi.org/10.1001/archotol.1969.00770020401030

Lilly, D., 1984. Multiple frequency, multiple component tympanometry: New approaches to an old diagnostic problem. Ear and Hearing 5, 300–308.

Lim, D.J., 1995. Structure and function of the tympanic membrane: A review. Acta Otorhinolaryngol Belg 49, 101–115.

Lim, D.J., 1970. Human tympanic membrane. Acta Oto-Laryngologica 70, 176–186. https://doi.org/10.3109/00016487009181875

Lim, D.J., 1968. Tympanic membrane part II.: Pars flaccida. Acta Oto-Laryngologica 66, 515–532. https://doi.org/10.3109/00016486809126316

Luo, H., Dai, C., Gan, R.Z., Lu, H., 2009a. Measurement of young's modulus of human tympanic membrane at high strain rates. J Biomech Eng 131, 064501. https://doi.org/10.1115/1.3118770

Luo, H., Jiang, S., Nakmali, D.U., Gan, R.Z., Lu, H., 2015. Mechanical properties of a human eardrum at high strain rates after exposure to blast waves. J Dyn Behav Mater 2, 59–73. https://doi.org/10.1007/s40870-015-0041-3

Luo, H., Lu, H., Dai, C., Gan, R.Z., 2009b. A comparison of Young's modulus for normal and diseased human eardrums at high strain rates. J Int Exp Comp Biomech 1, 1–22.

Maftoon, N., Funnell, W.R.J., Daniel, S.J., Decraemer, W.F., 2015. Finite-element modelling of the response of the gerbil middle ear to sound. J Assoc Res Otolaryngol 16, 547–567. https://doi.org/10.1007/s10162-015-0531-y

Maftoon, N., Funnell, W.R.J., Daniel, S.J., Decraemer, W.F., 2014. Effect of opening middle-ear cavity on vibrations of gerbil tympanic membrane. J Assoc Res Otolaryngol 15, 319–334. https://doi.org/10.1007/s10162-014-0442-3

Maftoon, N., Funnell, W.R.J., Daniel, S.J., Decraemer, W.F., 2013. Experimental study of vibrations of gerbil tympanic membrane with closed middle ear cavity. J Assoc Res Otolaryngol 14, 467–481. https://doi.org/10.1007/s10162-013-0389-9

Margolis, R.H., Bass-Ringdahl, S., Hanks, W.D., Holte, L., Zapala, D.A., 2003. Tympanometry in newborn infants--1 kHz norms. J Am Acad Audiol 14, 383–392.

Margolis, R.H., Goycoolea, H.G., 1993. Multifrequency tympanometry in normal adults. Ear Hear 14, 408–413. https://doi.org/10.1097/00003446-199312000-00006

McKinley, A.M., Grose, J.H., Roush, J., 1997. Multifrequency tympanometry and evoked otoacoustic emissions in neonates during the first 24 hours of life. J Am Acad Audiol 8, 218–223.

Motallebzadeh, H., Charlebois, M., Funnell, W.R.J., 2013. A non-linear viscoelastic model for the tympanic membrane. J Acoust Soc Am 134, 4427–4434. https://doi.org/10.1121/1.4828831

Motallebzadeh, H., Maftoon, N., Pitaro, J., Funnell, W.R.J., Daniel, S.J., 2017a. Finite-element modelling of the acoustic input admittance of the newborn ear canal and middle ear. J Assoc Res Otolaryngol 18, 25–48. https://doi.org/10.1007/s10162-016-0587-3

Motallebzadeh, H., Maftoon, N., Pitaro, J., Funnell, W.R.J., Daniel, S.J., 2017b. Fluid-structure finite-element modelling and clinical measurement of the wideband acoustic input admittance of the newborn ear canal and middle ear. J Assoc Res Otolaryngol 18, 671–686. https://doi.org/10.1007/s10162-017-0630-z

Nambiar, S., 2010. An experimental study of middle-ear vibrations in gerbils (M.Eng. Thesis). McGill University, Canada.

O'Connor, K.N., Cai, H., Puria, S., 2017. The effects of varying tympanic-membrane material properties on human middle-ear sound transmission in a three-dimensional finite-element model. J Acoust Soc Am 142, 2836–2853. https://doi.org/10.1121/1.5008741

Paradise, J.L., Smith, C.G., Bluestone, C.D., 1976. Tympanometric detection of middle ear effusion in infants and young children. Pediatrics 58, 198–210.

Purkait, R., 2013. Progression of growth in the external ear from birth to maturity: A 2-year follow-up study in India. Aesth Plast Surg 37, 605–616. https://doi.org/10.1007/s00266-013-0097-1

Qi, L., Funnell, W.R.J., Daniel, S.J., 2008. A nonlinear finite-element model of the newborn middle ear. J Acoust Soc Am 124, 337–347. https://doi.org/10.1121/1.2920956

Qi, L., Liu, H., Lutfy, J., Funnell, W.R.J., Daniel, S.J., 2006. A nonlinear finite-element model of the newborn ear canal. J Acoust Soc Am 120, 3789–3798. https://doi.org/10.1121/1.2363944

Rabbitt, R.D., Holmes, M.H., 1986. A fibrous dynamic continuum model of the tympanic membrane. J Acoust Soc Am 80, 1716–1728. https://doi.org/10.1121/1.394284

Ravicz, M.E., Cooper, N.P., Rosowski, J.J., 2008. Gerbil middle-ear sound transmission from 100Hz to 60kHz. J Acoust Soc Am 124, 363–380. https://doi.org/10.1121/1.2932061

Ravicz, M.E., Rosowski, J.J., 2013. Middle-ear velocity transfer function, cochlear input immittance, and middle-ear efficiency in chinchilla. J Acoust Soc Am 134, 2852–2865. https://doi.org/10.1121/1.4818745

Ravicz, M.E., Rosowski, J.J., 1997. Sound-power collection by the auditory periphery of the Mongolian gerbil Meriones unguiculatus: III. Effect of variations in middle-ear volume. J Acoust Soc Am 101, 2135–2147. https://doi.org/10.1121/1.418275

Ravicz, M.E., Rosowski, J.J., Voigt, H.F., 1992. Sound-power collection by the auditory periphery of the Mongolian gerbil Meriones unguiculatus. I: Middle-ear input impedance. J Acoust Soc Am 92, 157–177. https://doi.org/10.1121/1.404280

Rosowski, J.J., Cheng, J.T., Ravicz, M.E., Hulli, N., Hernandez-Montes, M., Harrington, E., Furlong, C., 2009. Computer-assisted time-averaged holograms of the motion of the surface of the mammalian tympanic membrane with sound stimuli of 0.4 to 25 kHz. Hear Res 253, 83–96. https://doi.org/10.1016/j.heares.2009.03.010

Rosowski, J.J., Lee, C.-Y., 2002. The effect of immobilizing the gerbil's pars flaccida on the middle-ear's response to static pressure. Hear Res 174, 183–195. https://doi.org/10.1016/S0378-5955(02)00655-X

Rosowski, J.J., Ravicz, M.E., Teoh, S.W., Flandermeyer, D., 1999. Measurements of middle-ear function in the mongolian gerbil, a specialized mammalian ear. Audiol Neurootol 4, 129–36.

Ruah, C.B., Schachern, P.A., Zelterman, D., Paparella, M.M., Yoon, T.H., 1991. Age-related morphologic changes in the human tympanic membrane: A light and electron microscopic study. Arch Otolaryngol Head Neck Surg 117, 627–634. https://doi.org/10.1001/archotol.1991.01870180063013

Saha, R., Srimani, P., Mazumdar, A., Mazumdar, S., 2017. Morphological Variations of Middle Ear Ossicles and its Clinical Implications. J Clin Diagn Res 11, AC01–AC04. https://doi.org/10.7860/JCDR/2017/23906.9147

Salih, W.H.M., Soons, J.A.M., Dirckx, J.J.J., 2016. 3D displacement of the middle ear ossicles in the quasi-static pressure regime using new X-ray stereoscopy technique. Hear Res 340, 60–68. https://doi.org/10.1016/j.heares.2015.12.003

Saunders, J.C., Kaltenbach, J.A., Relkin, E.M., 1983. The structural and functional development of the outer and middle ear, in: Romand, R. (Ed.), Development of Auditory and Vestibular Systems. Academic Press, pp. 3–25. https://doi.org/10.1016/B978-0-12-594450-2.50006-X

Shanks, J.E., Shohet, J.A., 2008. Tympanometry in Clinical Practice, in: Handbook of Clinical Audiology. Williams & Wilkins, Baltimore, pp. 157–188.

Shanks, J.E., Wilson, R.H., 1986. Effects of direction and rate of ear-canal pressure changes on tympanometric measures. J Speech Hear Res 29, 11–19. https://doi.org/10.1044/jshr.2901.11

Shapiro, R., 2014. An experimental study of vibrations in the gerbil middle ear under static pressure (M.Eng. Thesis). McGill University, Canada.

Simo, J.C., Hughes, T.J.R. (Eds.), 1998. Viscoelasticity, in: Computational Inelasticity, Interdisciplinary Applied Mathematics. Springer, New York, NY, pp. 336–373. https://doi.org/10.1007/0-387-22763-6_10

Soleimani, M., Funnell, W.R.J., Decraemer, W.F., 2020. A non-linear viscoelastic model of the incudostapedial joint. J Assoc Res Otolaryngol 21, 21–32. https://doi.org/10.1007/s10162-019-00736-0

Soleimani, M., Funnell, W.R.J., Decraemer, W.F., 2018. A new finite-element model of the incudostapedial joint. AIP Conference Proceedings 1965, 110003. https://doi.org/10.1063/1.5038503

Standring, S., 2016. Gray's Anatomy: The Anatomical Basis of Clinical Practice, 41st ed. Elsevier Limited, New York.

Stenfeldt, K., Johansson, C., Hellström, S., 2006. The collagen structure of the tympanic membrane: Collagen types I, II, and III in the healthy tympanic membrane, during healing of a perforation, and during infection. Arch Otolaryngol Head Neck Surg 132, 293–298. https://doi.org/10.1001/archotol.132.3.293

Sun, Q., Gan, R.Z., Chang, K.-H., Dormer, K.J., 2002. Computer-integrated finite element modeling of human middle ear. Biomechanics and Modeling in Mechanobiology 1, 109–122.

Teoh, S.W., Flandermeyer, D.T., Rosowski, J.J., 1997. Effects of pars flaccida on sound conduction in ears of Mongolian gerbil: Acoustic and anatomical measurements. Hear Res 106, 39–65. https://doi.org/10.1016/S0378-5955(97)00002-6

Terkildsen, K., Thomsen, K.A., 1959. The influence of pressure variations on the impedance of the human ear drum: A method for objective determination of the middle-ear pressure. J Laryngol Otol 73, 409–418. https://doi.org/10.1017/S002221510005550X

Therkildsen, A., Gaihede, M., 2005. Accuracy of tympanometric middle ear pressure determination: The role of direction and rate of pressure change with a fast, modern tympanometer. Otol Neurotol 26, 252–256.

Tonndorf, J., Khanna, S.M., 1972. Tympanic-membrane vibrations in human cadaver ears studied by time-averaged holography. J Acoust Soc Am 52, 1221–1233. https://doi.org/10.1121/1.1913236

Tonndorf, J., Khanna, S.M., 1968. Submicroscopic displacement amplitudes of the tympanic membrane (cat) measured by a laser interferometer. J Acoust Soc Am 44, 1546–1554. https://doi.org/10.1121/1.1911295

Van Camp, K.J., Margolis, R.H., Wilson, R.H., Creten, W.L., Shanks, J.E., 1986. Principles of tympanometry. ASHA Monogr 1–88.

van de Heyning, P.H., van Camp, K.J., Creten, W.L., Vanpeperstraete, P.M., 1982. Incudo-stapedial joint pathology: A tympanometric approach. J Speech Hear Res 25, 611–618. https://doi.org/10.1044/jshr.2504.611

Van der Jeught, S., Dirckx, J.J.J., Aerts, J.R.M., Bradu, A., Podoleanu, A.G., Buytaert, J.A.N., 2013. Full-field thickness distribution of human tympanic membrane obtained with optical coherence tomography. J Assoc Res Otolaryngol 14, 483–494. https://doi.org/10.1007/s10162-013-0394-z

Vanhuyse, V.J., Creten, W.L., Camp, K.J.V., 1975. On the W-notching of tympanograms. Scandinavian Audiology 4, 45–50. https://doi.org/10.3109/01050397509075014

von Unge, M., Decraemer, W.F., Bagger-Sjöbäck, D., Dirckx, J.J., 1993. Displacement of the gerbil tympanic membrane under static pressure variations measured with a real-time differential moire interferometer. Hear Res 70, 229–242. https://doi.org/10.1016/0378-5955(93)90161-S

Wada, H., Ando, M., Takeuchi, M., Sugawara, H., Koike, T., Kobayashi, T., Hozawa, K., Gemma, T., Nara, M., 2002. Vibration measurement of the tympanic membrane of guinea pig temporal bones using time-averaged speckle pattern interferometry. J Acoust Soc Am 111, 2189–2199. https://doi.org/10.1121/1.1467671

Wada, H., Kobayashi, T., 1990. Dynamical behavior of middle ear: Theoretical study corresponding to measurement results obtained by a newly developed measuring apparatus. J Acoust Soc Am 87, 237–245. https://doi.org/10.1121/1.399290

Wada, H., Koike, T., Kobayashi, T., 1998. Clinical applicability of the sweep frequency measuring apparatus for diagnosis of middle ear diseases. Ear Hear 19, 240–249.

Wada, H., Metoki, T., Kobayashi, T., 1992. Analysis of dynamic behavior of human middle ear using a finite-element method. J Acoust Soc Am 92, 3157–3168. https://doi.org/10.1121/1.404211

Wang, X., Cheng, T., Gan, R.Z., 2007. Finite-element analysis of middle-ear pressure effects on static and dynamic behavior of human ear. J Acoust Soc Am 122, 906–917. https://doi.org/10.1121/1.2749417

Wang, X., Gan, R.Z., 2016. 3D finite element model of the chinchilla ear for characterizing middle ear functions. Biomech Model Mechanobiol 15, 1263–1277. https://doi.org/10.1007/s10237-016-0758-5

Wu, J.Z., Dong, R.G., Smutz, W.P., Schopper, A.W., 2003. Nonlinear and viscoelastic characteristics of skin under compression: Experiment and analysis. Bio-med Mater Eng 13, 373–385.

Zhang, X., Gan, R.Z., 2011. Experimental measurement and modeling analysis on mechanical properties of incudostapedial joint. Biomech Model Mechanobiol 10, 713–726. https://doi.org/10.1007/s10237-010-0268-9

Zienkiewicz, O.C., Taylor, R.L., Zhu, J.Z., 2013. The Finite Element Method: Its Basis and Fundamentals, 7th ed. Butterworth-Heinemann, Oxford. https://doi.org/10.1016/B978-1-85617-633-0.00004-6

Zwislocki, J., 1957. Some impedance measurements on normal and pathological ears. J Acoust Soc Am 29, 1312–1317. https://doi.org/10.1121/1.1908776